

Yale University

## EliScholar – A Digital Platform for Scholarly Publishing at Yale

---

Yale Graduate School of Arts and Sciences Dissertations

---

Spring 2022

### Resonant Integrated Nonlinear Photonics for the Development of Compact and Stable Soliton Microcombs

Joshua Brian Surya

*Yale University Graduate School of Arts and Sciences*, [surya.jb@gmail.com](mailto:surya.jb@gmail.com)

Follow this and additional works at: [https://elischolar.library.yale.edu/gsas\\_dissertations](https://elischolar.library.yale.edu/gsas_dissertations)

---

#### Recommended Citation

Surya, Joshua Brian, "Resonant Integrated Nonlinear Photonics for the Development of Compact and Stable Soliton Microcombs" (2022). *Yale Graduate School of Arts and Sciences Dissertations*. 665.  
[https://elischolar.library.yale.edu/gsas\\_dissertations/665](https://elischolar.library.yale.edu/gsas_dissertations/665)

This Dissertation is brought to you for free and open access by EliScholar – A Digital Platform for Scholarly Publishing at Yale. It has been accepted for inclusion in Yale Graduate School of Arts and Sciences Dissertations by an authorized administrator of EliScholar – A Digital Platform for Scholarly Publishing at Yale. For more information, please contact [elischolar@yale.edu](mailto:elischolar@yale.edu).

## Abstract

# Resonant Integrated Nonlinear Photonics for the Development of Compact and Stable Soliton Microcombs

Joshua B. Surya

2022

Nonlinear nanophotonic devices are crucial building blocks of a fully integrated photonic system. They enable high-speed, high-throughput and customizable transfer of information, with applications ranging from biology to cutting edge quantum information technologies. A particularly important nanophotonics component is the micro-resonator. Not only do micro-resonators confine light and allow an effective increased length of interaction with a desired material platform, they are also highly compact. Through the amplification of light-matter interaction, nonlinear phenomena such as soliton comb generation, record breaking second and third harmonic generation as well as electro-optic frequency conversion have been observed on an integrated on-chip platform. The work presented here investigates the methods of integration and optimization of many such nonlinear micro-resonators with the ultimate goal of developing the first fully integrated and stabilized soliton microcomb.

Resonant Integrated Nonlinear Photonics for the Development of Compact  
and Stable Soliton Microcombs

A Dissertation  
Presented to the Faculty of the Graduate School  
of  
Yale University  
in Candidacy for the Degree of  
Doctor of Philosophy

by  
Joshua B. Surya

Dissertation Director: Hong X. Tang

May 2022

Copyright © 2022 by Joshua B. Surya

All rights reserved.

## Acknowledgments

I was fortunate enough throughout my Ph.D. to have received support from an amazing group of individuals.

My advisor Professor Hong Tang, who offered me the opportunity to pursue my doctoral studies in his group and provided valuable insights for my research. His encouragement and constant support made my life as a graduate student a thoroughly enjoyable experience.

My dissertation committee that included Professor Mark Reed, Professor Fengnian Xia, Professor Hui Cao. Their patience and commitment to giving me feedback were, without a doubt, top contributing reasons to any success I may have come across during my studies. I consider myself extremely lucky to have crossed paths with Mark, who always went out of his way to be kind and friendly to others. I would also like to acknowledge helpful guidance from Professor Yuji Zhao, who served as the external reader of this thesis.

My beloved lab-mates, past and present, including Xufeng Zhang, Changling Zou, Linran Fan, Hojoong Jung, Xiang Guo, Xu Han, Alexander Bruch, Na Zhu, Xianwen Liu, Risheng Cheng, Wei Fu, Zheng Gong, Jorge Holguin-Lerma, Yiyu Zhou, Juanjuan Lu, Sihao Wang, Mingrui Xu, Yuntao Xu, Mohan Shen, Ayed Al Sayem, Yubo Wang, Likai Yang, Jiacheng Xie, Fengyan Yang, Danqing Wang, Yufeng Wu, Mattia Vezzoli, Chunzhen Li and Sunny Yang. There is no other group of people I would have rather spent my years as a graduate student with. I am grateful for your support and amazing company.

I am grateful for the invaluable help I received during device fabrication from staff members, including Michael Power, Christopher Tillinghast, James Agresta, Kelly Woods, Sean Rinehart, Dr. Yong Sun, Dr. Michael Rooks and Nicholas Bernardo. I would also like to thank members of the administrative offices, Cara Gibilisco, Pamela Defilippo, Vanessa Epps, Nehemiah Hodges, Andrew Morcus, Michael Carbone and Senen Antunez

who have helped me immensely in all parts of my research.

I would like to thank a few individuals who I have learned a lot from and who have been important friends to me during my doctoral studies. Eugene, Ming, Wei, Zheng, Josh, Yubin, Yuri, Kevin, Dan, Neil, Mohan, Na, Juanjuan, Ragu, Eric, thanks for being there when I needed you, whether it was for discussing research, games, or a clogged toilet. Eugene, thank you for teaching me important life skills (like cooking, or being less awkward) that I have had to use throughout my studies to survive.

Lastly, I would like to acknowledge the individuals who have impacted and supported me unconditionally throughout my studies.

Si Si, my wife, who has an uncanny ability to make me laugh and happy under any circumstances, is equally skilled at yawning to everything I say that has to do with this thesis. Thank you for being the most understanding and loving wife.

Natalie, my sister, who has always had my back since I was a kid. Thank you for looking out for me as intensely as you did 20 years ago. I know you will still treat me as your baby brother in another 20 years.

Charles, my dad, his influence on me is reflected by my writing of this thesis. Thank you for your advice throughout these years and for showing me what it means to be hard-working. I am who I am because of you.

Lastly my mom Katherine, her kindness, patience and unending support for me throughout my life has been a source of comfort and inspiration. I wish to have your level of dedication and thoughtfulness one day.

*For my family...*

# Contents

<b>1</b>	<b>Introduction</b>	<b>1</b>
1.1	Integrated nonlinear optics . . . . .	1
1.1.1	Progress in Nonlinear Optics . . . . .	1
1.1.2	Progress in Integrated Nonlinear Photonics . . . . .	3
1.2	Thesis goal and outline . . . . .	4
<b>2</b>	<b>Efficient Second Harmonic Generation at a Targeted Wavelength with Pi-cometer Precision</b>	<b>9</b>
2.1	Motivation . . . . .	9
2.2	Second Harmonic Generation on Aluminum Nitride Microrings . . . . .	10
2.2.1	Theoretical Description of SHG . . . . .	10
2.2.2	Phase, Resonance and Energy Matching Conditions . . . . .	13
2.3	Second Harmonic Generation at a Target Wavelength . . . . .	15
2.4	Future Work and Conclusions . . . . .	22
<b>3</b>	<b>Third Harmonic Generation on a Hybrid Aluminum Nitride on Silicon Nitride Platform</b>	<b>23</b>
3.1	Motivation . . . . .	23
3.2	Doubly Resonant Third Harmonic Generation in Aluminum Nitride/Silicon Nitride Microrings . . . . .	24
3.2.1	Theoretical Description . . . . .	24
3.3	Optimization of Third Harmonic Generation . . . . .	27
3.4	Fabrication . . . . .	29
3.5	Results and Discussion . . . . .	30



3.6	Future Work and Conclusions . . . . .	37
<b>4</b>	<b>Stable Tuning of Resonant Modes in Lithium Niobate Microrings</b>	<b>39</b>
4.1	Motivation . . . . .	39
4.2	Photorefractive and Thermal Nonlinear Effects in Lithium Niobate Microrings . . . . .	41
4.3	Theoretical Description of $\chi^{(2)}$ Nonlinear Frequency Conversion in a Lithium Niobate Microring . . . . .	42
4.3.1	Saturation of the Photorefractive Effect . . . . .	42
4.3.2	Modeling of Second Harmonic Generation With an Auxiliary Laser	44
4.4	Results and Discussion . . . . .	47
4.4.1	Auxiliary Laser Stabilization of LN Microring Resonant Modes .	47
4.4.2	Modal Phase-Matched SHG on LN . . . . .	53
4.5	Future Work and Conclusions . . . . .	54
<b>5</b>	<b>Integration of Soliton Microcombs and SHG on Aluminum Nitride Microrings</b>	<b>56</b>
5.1	Motivation . . . . .	56
5.2	Soliton Generation on Aluminum Nitride Microrings . . . . .	58
5.3	Theoretical Description of Soliton Generation . . . . .	59
5.4	Device Modeling . . . . .	62
5.5	Device Design . . . . .	65
5.5.1	Octave Spanning Soliton Combs . . . . .	65
5.5.2	Device Fabrication . . . . .	70
5.6	Coupled Rings for the Integration of Frequency Doubling and Comb Generation . . . . .	71
5.6.1	Theoretical Description . . . . .	72
5.7	Results and Discussion . . . . .	77
<b>6</b>	<b>Summary and outlook</b>	<b>85</b>
<b>A</b>	<b>Microring Resonator Design and Fabrication</b>	<b>87</b>
A.1	Microring Resonators . . . . .	87
A.1.1	Waveguide Coupling . . . . .	87
A.1.2	Dispersion and the Free Spectral Range . . . . .	90
A.1.3	Quality Factor and Finesse . . . . .	91

## **B Frequency Comb Simulation**

<b>Source Code</b>	<b>95</b>
B.1 Main Code . . . . .	95
B.2 Comb Solver . . . . .	97
B.3 Cython . . . . .	106

# List of Figures

2.1	Schematic illustration of SHG in a microring . . . . .	11
2.2	(a) Analysis of the phase-matching condition across different widths. Simulation included details of the cross sectional geometry of the ring, with a sidewall angle of 8 degrees. The refractive index curve of our material was measured by an ellipsometer. The experimental data agrees with the simulated data reasonably well. (b) Analysis of the resonance wavelength at varying radii. . . . .	15
2.3	(a) Dependence of the phase-matched wavelength as the ring width increases. Phase-matching wavelengths tend to occur at larger pump wavelengths as ring widths increase. (b) Comparison of the simulated and measured phase-matched wavelengths with the designed ring width. Measured data is color coded by SHG output power as described by the color scale. . . . .	18
2.4	A schematic of the device, where the ring radius is varied across a single device and the ring width is varied across devices. Over 300 of microrings can be fit onto a single chip, which can guarantee an optimized phase-matching in a desired wavelength, assuming fixed height and bulk refractive index profile. . . . .	19

2.5	(a) Shows the temperature dependent SH response on both a wavelength scale and the correspondingly transformed temperature scale using the thermo-shift coefficient of polycrystalline AlN at the IR wavelengths, assuming the coefficient is constant. A maximum internal efficiency of 1800%/W was observed at a wavelength of 1556.2 nm (110°C) with a 3 dB bandwidth (FWHM) of $0.303 \pm 0.068$ nm (17.5°C). Each data point is color coded by its corresponding temperature as shown by the color scale-bar. (b) A zoomed-in spectrum of the transmission at 110°C. (c) SHG at a fixed temperature of 110°C, with the peak SH power observed at the visible wavelength corresponding to $\lambda_{Rb}$ . . . . .	21
3.1	Effective index of the fundamental TE mode of the fundamental (solid red curve) and higher order modes of the third harmonic light (dotted curve) with varying ring widths. The intersecting points of the red curve with the other lines denote the ring widths that satisfy the phase matching. The phase-matched TE modes are marked with the corresponding labels from Table 3.1. . . . .	28
3.2	SEM micrograph of a ring resonator device on the hybrid material platform	29
3.3	Schematic of the experimental setup, where the dotted box indicates the cross section of the device under test. A wavelength demultiplexer on the input and output side of the device captures the TH visible signal (green) as well as the transmitted IR signal (red) which is then received by the photodetectors. The scattered light from the microring is collected by the Andor Spectrograph, a spectrometer located directly atop the device. . . .	30
3.4	Photographed top view of the TH light scattered from the ring. . . . .	30
3.5	Third harmonic generation spectrum with respect to input pump wavelength. Data was taken using the Andor spectrograph 193i. At each pump wavelength input, TH light scattered from the ring was collected by the spectrograph with a slit opening of $50 \mu\text{m}$ and an integration time of one second. The linewidth of the THG wavelength is due to the limit in resolution of the Andor Spectrograph. No signal was captured at other visible wavelengths, suggesting a pure third harmonic process and not a cascaded second order process at play. . . . .	31

3.6	<p><b>(a)</b> Transmission at low input pump power. The resonance within the shaded region was used for generating TH light. <b>(b)</b> Transmission at high power of the IR pump resonance. Red curve and blue curve denote the experimentally observed and the simulated resonance respectively. The triangular shape resonance is a result of the thermal shifting of the 1541.2 nm resonance at high temperatures. The large shift is due to high confinement of thermal energy within the waveguide. <b>(c)</b> The TH response with respect to the pump wavelength. The response (green) is modeled by a lorentzian shaped curve (blue).</p>	32
3.7	<p>Schematic of the pulsed laser setup. Two separate IR inputs were used, one is connected to a commercial electro-optic modulator (EOM) with a low duty-cycle input control signal from an arbitrary waveform generator, used to probe the TH resonance. The EOM generates a pulsed signal which is then amplified by an EDFA and filtered by an oz-optics tunable filter. Fiber polarization controllers were placed on both sides of the EDFA in order to ensure TE mode operation. The auxiliary CW laser for temperature control was tuned into a resonance multiple FSRs away from the probe resonance to ensure phase-mismatch with the probe mode. Finally, IR detectors were used to monitor the pulsed laser average power as well as the visible TH signal from the microring.</p>	34
3.8	<p><b>(a)</b> Study of the THG power dependence using a continuous-wave (CW) laser input. The horizontal axis shows the amount of pump power that is coupled into the resonance at the phase-matched wavelength. The solid curve indicates the model prediction of the output power at high input powers, where a difference in resonance shift speeds causes resonance wavelength mismatch and subsequently a deviation from a cubic power dependence. <b>(b)</b> Temperature dependence of the THG. The temperature was tuned by coupling a (CW) input into a resonance away from the wavelength at which THG occurs. The absolute temperature was then calibrated for by measuring the thermal shift in the IR resonances. Simultaneously, a low-duty cycle modulated laser with a average power of 4 mW was used for THG. This scheme was implemented to avoid the thermal shift at high CW input powers. A lorentzian shaped temperature dependence curve with a full-width-at-half-maximum (FWHM) of 10.6°C is fitted.</p>	36

4.1	(a) Schematic of the experimental setup. Two laser inputs, a pump probe and an auxiliary drive were used for interrogating two separate cavity modes (the pump mode <i>a</i> and auxiliary mode <i>c</i> ). A higher power for the auxiliary laser input is used. (b) Conceptual diagram of the operation principle. The photorefractive effect causes unstable and difficult resonance locking. The proposed solution first utilizes an auxiliary laser, by slowly tune it into resonance at high power, where stable tuning is possible due to the stable dynamics of thermal expansion and photorefraction. With the auxiliary laser in resonance, the target mode can be stably accessed at low powers. . . . .	48
4.2	Experimental and simulated SH output plots with the auxiliary laser off and on resonance. (a) SH output traces measured at intervals of 10 seconds, with the auxiliary laser set to be far-detuned from the resonance. The on-chip auxiliary and probe laser powers were set to 5.4 mW and 98.6 $\mu$ W respectively. The inset depicts the shifting peak of the SHG with number of laser scans, where the measured and simulated data are denoted by circles and triangles. (b) The simulated SH output of the measurement without an auxiliary laser. The cold cavity resonance wavelengths for IR and SH modes are fitted to be approximately 1571.05 nm and 785.535 nm respectively, this slight energy mismatch causes the double peaks observed in the SHG spectrum. (c) SH output traces when the auxiliary laser is locked into one resonance, at intervals of 10 seconds. The auxiliary laser suppresses the PR-induced resonance shifts, allowing stable cavity access. The inset depicts the stabilized peak of the SHG with number of laser scans. (d) Simulated output traces of SHG with the auxiliary laser in resonance. . . . .	50
4.3	Tuning of SHG peak wavelength using an auxiliary laser and the photorefractive effect. (a) Illustration of the transmission curve of the auxiliary mode resonance with red-to-blue scan. Each arrow independently signifies a different auxiliary laser wavelength used when measuring the SHG output. The color of the arrow corresponds to the trace in (b). (b) Normalized SHG output at various Auxiliary laser wavelengths (5 mW auxiliary laser power on-chip). The simulated SHG peak wavelength is plotted against the traces (98.6 $\mu$ W on-chip probe power). . . . .	51

4.4	Simulated mode profiles relevant to phase-matching utilizing the $d_{33}$ component of the $\chi^{(2)}$ nonlinear coefficient, along with the mode overlap profile in the cross-section of the LN waveguide. For a film thickness of 600 nm, phase-matching occurs at 600 nm. (b) Mode profiles of the IR and visible mode at a phase-matching width of $1.2 \mu\text{m}$ , utilizing the $d_{31}$ coefficient. (c)-(d) Measured transmission and SHG output of a $1.2 \mu\text{m}$ wide ring with a TE <sub>00</sub> IR input pump. The SHG spectrum corresponds to a 600%/W efficiency. . . . .	53
5.1	The top plot displays the integrated dispersion ( $D_{int}$ ) profile of the corresponding intracavity comb power (log-scale) profile of the simulated single soliton comb profile on the bottom. The red line indicates zero $D_{int}$ . Peaks in the comb power can be associated with zero crossings in $D_{int}$ as indicated by the shaded regions. . . . .	60
5.2	Wavelength dependence of the coupling Q ( $Q_c$ ), plotted on logarithm scale. The inset shows the cross sectional simulation of the ring (left) and the bus waveguide (right) mode in commercial software FIMMWAVE, which is then used to calculate the evanescent field overlap. . . . .	61
5.3	Simulated comb dynamics. (a) A plot of the integrated dispersion profile used in the simulation. (b) Comb power throughout the simulation at each snapshot as the pump frequency started from the blue-detuned region to the red-detuned region. Total simulated time was $1 \mu\text{s}$ , and was divided into 2000 equally spaced in time "snapshots" and plotted. Pump frequency in simulation was tuned from 193.4156 THz to 193.4124 THz. (c) Plotted comb power for each simulated mode frequency at the starred snapshot of (b), where the blue stem-plot is the intracavity power and the orange curve is the waveguide power. (d) The temporal profile of (c), where $\theta$ represents the radial location within the microring. . . . .	63
5.4	(a) Dependence of the long wavelength dispersive wave (LWDW) frequency on both AlN height and the ring width, note that the same change in height produces a much larger difference in the frequency of the LWDW compared to the same change in ring width. (b) Experimental observation of the change in LWDW frequency and the overall comb spectrum due to a $\approx 10\text{nm}$ difference in height indicated by the red and green starred location of the devices on the chip in (c) which is a map of the height variation within the measured chip. . . . .	66

5.5	(a) A comb spectrum showing the presence of both the stimulated Raman scattering process and Ker four-wave-mixing, the first stokes line is at 1706 nm and the second stokes line is located at 1905 nm. (b) A plot of total comb power with respect to pump wavelength, scanned across the resonance at a speed of 10 nm/s, this plot shows no presence of stimulated Raman scattering. (c) A plot of total comb power which shows Raman interactions. In general the observance of stimulated Raman scattering is correlated with the observance of a larger thermal triangle. . . . .	69
5.6	Before and after ion milling. (a) The variation of height in nanometers over a photonic chip before processing. (b) Variation of height in nanometers over the same photonic chip after ion-milling and before patterning and fabrication of the microring devices. . . . .	70
5.7	Numerical modeling of the coupled rings. (a) The simulated total comb power as the pump laser is swept over the resonance. In the inset is a measured comb power spectrum from a coupled microrings device. (b) Simulated intracavity and waveguide soliton comb spectrum corresponding to the detuning of the red star in (a). This corresponds to the intracavity power in the soliton ring highlighted in red. (c) Simulated coupled intracavity and waveguide power spectrum in the doubler ring. A corresponding theoretically achievable SHG efficiency of 50,000%/W would produce an in-waveguide SH power of -63 dBm at 288 THz. . . . .	76
5.8	Measurement of soliton comb microring devices with varying widths. The dispersive waves tend to deviate away from the pump line as the ring width decreases, indicating a broadening of the corresponding integrated dispersion profile. . . . .	78
5.9	Simultaneous observance of SHG and soliton microcomb. (a) Generated to-scale image of the device measured, where the red shaded device is the soliton microring and the green shaded device is the microring doubler. (b) Multi-soliton spectrum generated by the microring with an input power of 2.5 W. (c) Measurement of SHG at 450 $\mu$ W of input power. . . . .	79
5.10	Simulation of SHG from the auxiliary doubler microring. The x-axis is the detuning of the two coupled modes while the y-axis is the pump detuning. Both axes are normalized by the FSR. A coupling rate of 1.5 GHz was used.	80



5.11 Simultaneous observance of broadband comb and high efficiency SHG. (a) Display of the transmission and corresponding SHG spectrum of the doubler (auxiliary) ring coupled to the primary ring. The measurement was performed using a $2\ \mu\text{m}$ tunable laser set at $800\ \mu\text{W}$ corresponding to waveguide power of $300\ \mu\text{W}$ . (b) MI comb from the primary ring, spanning greater than one octave. . . . .	81
5.12 Observed soliton spectrum from a primary ring. . . . .	82
A.1 Conceptual illustration of a microring resonator, including coupling terms, loss and phase . . . . .	88

# List of Tables

3.1 Phase matched widths from simulations with the respective mode profiles and calculated overlap factor  $\zeta$ . . . . . 27

# Chapter 1

## Introduction

### 1.1 Integrated nonlinear optics

#### 1.1.1 Progress in Nonlinear Optics

The study of nonlinear systems began when it became apparent that simple models often lacked accuracy in the description of the observed world. An example of such was recorded in the early 1900s, when Lord Rayleigh derived and subsequently spawned the earliest works on nonlinear acoustics, while taking inspiration from Maxwell's theories of radiation pressure from electromagnetic waves<sup>1</sup>. Another early study of a nonlinear optical effect is the phenomenon of two-photon absorption, which was predicted and theorized by Maria Goeppert-Mayer in her 1931 doctoral thesis, thirty years before it was observed experimentally (owing to the invention of lasers)<sup>2</sup>.

One of the most discussed nonlinear effect in this thesis is the Kerr effect, which is the driver of four-wave mixing (FWM) processes such as frequency microcomb generation, third harmonic generation (THG) and Raman scattering. It was discovered in 1875 by John Kerr when an electrostatic field was observed to cause a difference in refractive index of the ordinary and extraordinary light (double refraction), this difference was observed to be

proportional to the square of the applied electric field. Soon after, the Pockels electro-optic effect was discovered in materials that lack inversion symmetry. In contrast to the Kerr effect, it was discovered that the Pockels effect causes the index of refraction experienced by light to be linearly dependent on the applied steady electric field.

Up until the 1960s, many nonlinear optical effects were hypothesized but the experimental realization was not possible until the construction of a laser by Theodore Maiman. The laser provided high intensity coherent light which was the catalyst needed for the first experimental observation of second harmonic generation (SHG) in 1961 by Peter Franken and colleagues<sup>3</sup>. Soon after the demonstration, theoretical formulations of many nonlinear optical effects were predicted. The invention of the laser was a much needed catalyst as it relates to the proof of principle optical experiments.

Since the first demonstration of SHG, many nonlinear optical effects utilizing the AC Kerr and Pockels effects have been demonstrated<sup>4,5</sup>. Nonlinear optics has since become a critical process for frequency conversion. The very basics of nonlinear frequency conversion can be understood by using a Taylor series expansion of the induced electric dipole moments in a dielectric material, otherwise known as the polarization density.

$$P(x,t) = \epsilon_0 \left( \chi^{(1)} E(x,t) + \chi^{(2)} E^2(x,t) + \chi^{(3)} E^3(x,t) + \dots \right) \quad (1.1)$$

$$\begin{aligned} P^{(2)}(x,t) = \epsilon_0 \chi^{(2)} & \left( E_i^2(x) e^{-i2\omega_i t} + E_j^2(x) e^{-i2\omega_j t} \right. \\ & + 2E_i(x) E_j(x) e^{-i(\omega_i + \omega_j)t} + 2E_i(x) E_j(x) e^{-i(\omega_i - \omega_j)t} \\ & \left. + (|E_i|^2 + |E_j|^2) \right) \end{aligned} \quad (1.2)$$

Using the above expanded equation, it can be seen that the second order nonlinear wave mixing term describes many nonlinear optical processes including SHG, difference frequency generation (DFG), and sum frequency generation (SFG). Much of the theoretical work related to these processes were formulated soon after the demonstration of SHG

and led to the rapid increase of efficiency in nonlinear optical processes through the understanding of phase-matching. Furthermore, Kerr nonlinear mixing processes are resultant of the third order nonlinear term in Eq. 1.1 which is the source of major innovations in frequency combs and temporal solitons in microresonators<sup>6-8</sup>.

As the thesis will try to demonstrate, the importance of Kerr ( $\chi^{(3)}$ ) and Pockels ( $\chi^{(2)}$ ) nonlinearity in the field of integrated nonlinear optics cannot be overstated. They are highly utilized in microcavity systems where the internal field can be amplified to many times the input light, thus increasing the interaction between light and the nonlinear material.

### 1.1.2 Progress in Integrated Nonlinear Photonics

While early works in nonlinear optics were table-top experiments that typically required an elaborate setup, recent advances in laser and fabrication technologies has allowed significant progress in developing nano-scale platforms for nonlinear optics. Dating back to the 1970s were initial efforts in the design of optical waveguides using lithium niobate and III/V semiconductor materials due to their favorable opto-electronic properties<sup>9,10</sup>. Later on in the 1980s, silicon photonics became a highly popular platform due to low costs and integrability with conventional electronics as well as its favorable optical properties<sup>11</sup>. Since then high quality integrated photonics devices have been achieved on a variety of material platforms, each with its own sets of advantages and disadvantages<sup>4,12-15</sup>. Besides the integration of waveguides, passive and active optical components, breakthroughs in the demonstration of optical microcavities<sup>16</sup> allowed nonlinear optics to be observed at chip-scale using reasonable input powers.

Microcavities or microresonators have been realized using various platforms and configurations<sup>16</sup>. A particularly important configuration is the optical microring resonator, which in its most simplistic form, is a closed circular optical waveguide evanescently cou-

pled to a probing bus waveguide<sup>17</sup>. This type of microresonator is popular due to its simplicity in nano-fabrication and its easily configurable parameters such as ring radius and ring width which allows the engineering of effective index and geometric dispersion. Recently, high quality (Q) factor ring resonators have been realized on silicon nitride<sup>18,19</sup>, aluminum nitride<sup>20–22</sup>, lithium niobate<sup>12</sup>, and more<sup>16,23</sup>.

The ability to trap light within a confined space using a microresonator has had important applications in the field of frequency microcomb generation. Since the initial demonstration of frequency comb generation on a microresonator<sup>7</sup>, microcombs have been observed on many platforms.

In order for a frequency comb to be commercially viable, the spectral location of every comb line must be identified and stabilized. The two main sources of uncertainty in determining the absolute frequency of all comb lines are the carrier envelope offset frequency ( $f_{ceo}$ ) and the free spectral range (FSR). They are respectively defined by the difference between the first comb line and the zero frequency, as well as the frequency spacing between each comb line. Achieving such stability will have significant impact on applications such as frequency metrology<sup>24</sup>, ultra-fast communications<sup>25</sup>, and scalable quantum communication technologies<sup>26</sup>. Current state-of-the-art systems demonstrated have still required large footprints and are not fully integrated<sup>27,28</sup>, where the systems performing  $f_{ceo}$  and FSR detection are separate from the microcomb chip. Advances in integrated nonlinear photonics for the full integration of a stabilized comb are thus highly sought after and are the focus of this thesis.

## 1.2 Thesis goal and outline

The goal of this thesis is to resolve the challenge of integrating a fully stabilized comb onto a chip.

The remaining part of the thesis is organized as follows:

In [Chapter 2](#), we present a systematic method of fine-tuning microring parameters to simultaneously align the phase-matching and dual resonances on a target wavelength with picometer-level precision. This is particularly important for the stabilization of a frequency comb since taking advantage of cavity enhanced SHG will require aligning resonances and phase-matching windows to a very particular frequency of interest. As a proof of concept we achieved a microring resonator with optimized SHG efficiency at the wavelength of the rubidium two-photon transition at 1556.24 nm. This was repeating across many fabrication attempts.

In [Chapter 3](#), we demonstrate efficient THG on a hybrid aluminum nitride (AlN) and silicon nitride platform. This is useful for the integration of a stabilized comb since silicon nitride (SiN) is the most commonly used platform for soliton comb generation and AlN can compensate for SiN's lack of a second order nonlinear  $\chi^{(2)}$  tensor. Furthermore, THG can potentially lower the required bandwidth of a soliton comb for the detection of  $f_{\text{ceo}}$ , which is needed for comb stabilization.

In [Chapter 4](#), we introduce a method for the stable tuning of lithium niobate (LN) resonant modes. LN has become an important platform for both second order and Kerr nonlinear processes and thus cannot be neglected in the conversation of stabilizing microcombs. However, the photorefractive effect on LN presents a major challenge due to stability issues, which this chapter attempts to resolve using an auxiliary laser method.

In [Chapter 5](#), we demonstrate our design and preliminary results of using a pair of coupled rings for the purpose of integrating the measurement of  $f_{\text{ceo}}$  onto a single chip. First we present systematic numerical studies of frequency comb and second harmonic generation on the coupled system, then we discuss preliminary experimental results which demonstrate simultaneous high efficiency SHG and broadband comb generation. Furthermore we show that soliton comb generation can be achieved on these devices.

In the final [Chapter 6](#), we summarize this thesis and discuss the future work towards the full integration of a stable comb.

## References

- [1] R. T. Beyer, “Lord rayleigh and nonlinear acoustics,” *J. Acoust. Soc. Am.* **98**, 3032 (1995).
- [2] A. J. Miller, S. W. Nam, J. M. Martinis, and A. V. Sergienko, “Demonstration of a low-noise near-infrared photon counter with multiphoton discrimination,” *Applied Physics Letters* **83**, 791 (2003).
- [3] P. A. Franken, A. E. Hill, C. W. Peters, and G. Weinreich, “Generation of optical harmonics,” *Phys. Rev. Lett.* **7**, 118 (1961).
- [4] C. Xiong, W. H. P. Pernice, X. Sun, C. Schuck, K. Y. Fong, and H. X. Tang, “Aluminum nitride as a new material for chip-scale optomechanics and nonlinear optics,” *New Journal of Physics* **14**, 095014 (2012).
- [5] R. W. Boyd, *Nonlinear Optics*, 3rd ed. (Academic Press, San Diego, CA, 2008).
- [6] T. Udem, R. Holzwarth, and T. W. Hänsch, “Optical frequency metrology,” *Nature* **416**, 233 (2002).
- [7] P. Del’Haye, A. Schliesser, O. Arcizet, T. Wilken, R. Holzwarth, and T. J. Kippenberg, “Optical frequency comb generation from a monolithic microresonator,” *Nature* **450**, 1214 (2007).
- [8] T. Herr, V. Brasch, J. D. Jost, C. Y. Wang, N. M. Kondratiev, M. L. Gorodetsky, and T. J. Kippenberg, “Temporal solitons in optical microresonators,” *Nature Photonics* **8**, 145 (2013).
- [9] I. P. Kaminow, V. Ramaswamy, R. V. Schmidt, and E. H. Turner, “Lithium niobate ridge waveguide modulator,” *Applied Physics Letters* **24**, 622 (1974).
- [10] R. A. Logan and F. K. Reinhart, “Optical waveguides in GaAs–AlGaAs epitaxial layers,” *Journal of Applied Physics* **44**, 4172 (1973).
- [11] B. N. Kurdi and D. G. Hall, “Optical waveguides in oxygen-implanted buried-oxide silicon-on-insulator structures,” *Optics Letters* **13**, 175 (1988).
- [12] M. Zhang, C. Wang, R. Cheng, A. Shams-Ansari, and M. Lončar, “Monolithic ultra-high-q lithium niobate microring resonator,” *Optica* **4**, 1536 (2017).
- [13] D. J. Moss, R. Morandotti, A. L. Gaeta, and M. Lipson, “New CMOS-compatible platforms based on silicon nitride and hydrex for nonlinear optics,” *Nature Photonics* **7**, 597 (2013).
- [14] V. R. Almeida, C. A. Barrios, R. R. Panepucci, and M. Lipson, “All-optical control of light on a silicon chip,” *Nature* **431**, 1081 (2004).



- [15] T. Koch and U. Koren, “Semiconductor photonic integrated circuits,” *IEEE Journal of Quantum Electronics* **27**, 641 (1991).
- [16] K. J. Vahala, “Optical microcavities,” *Nature* **424**, 839 (2003).
- [17] S. F. Preble, Q. Xu, and M. Lipson, “Changing the colour of light in a silicon resonator,” *Nature Photonics* **1**, 293 (2007).
- [18] X. Ji, S. Roberts, M. Corato-Zanarella, and M. Lipson, “Methods to achieve ultra-high quality factor silicon nitride resonators,” *APL Photonics* **6**, 071101 (2021).
- [19] M. H. P. Pfeiffer, C. Herkommer, J. Liu, T. Morais, M. Zervas, M. Geiselmann, and T. J. Kippenberg, “Photonic damascene process for low-loss, high-confinement silicon nitride waveguides,” *IEEE Journal of Selected Topics in Quantum Electronics* **24**, 1 (2018).
- [20] A. W. Bruch, X. Liu, X. Guo, J. B. Surya, Z. Gong, L. Zhang, J. Wang, J. Yan, and H. X. Tang, “17 000%/w second-harmonic conversion efficiency in single-crystalline aluminum nitride microresonators,” *Applied Physics Letters* **113**, 131102 (2018).
- [21] A. W. Bruch, X. Liu, J. B. Surya, C.-L. Zou, and H. X. Tang, “On-chip  $\chi^{(2)}$  microring optical parametric oscillator,” *Optica* **6**, 1361 (2019).
- [22] Y. Sun, W. Shin, D. A. Laleyan, P. Wang, A. Pandey, X. Liu, Y. Wu, M. Soltani, and Z. Mi, “Ultrahigh q microring resonators using a single-crystal aluminum-nitride-on-sapphire platform,” *Optics Letters* **44**, 5679 (2019).
- [23] T. Baehr-Jones, M. Hochberg, C. Walker, and A. Scherer, “High-q ring resonators in thin silicon-on-insulator,” *Applied Physics Letters* **85**, 3346 (2004).
- [24] S. B. Papp, K. Beha, P. Del’Haye, F. Quinlan, H. Lee, K. J. Vahala, and S. A. Diddams, “Microresonator frequency comb optical clock,” *Optica* **1**, 10 (2014).
- [25] A. S. Raja, S. Lange, M. Karpov, K. Shi, X. Fu, R. Behrendt, D. Cletheroe, A. Lukashchuk, I. Haller, F. Karinou, B. Thomsen, K. Jozwik, J. Liu, P. Costa, T. J. Kippenberg, and H. Ballani, “Ultrafast optical circuit switching for data centers using integrated soliton microcombs,” *Nat. Commun.* **12**, 5867 (2021).
- [26] M. Kues, C. Reimer, J. M. Lukens, W. J. Munro, A. M. Weiner, D. J. Moss, and R. Morandotti, “Quantum optical microcombs,” *Nat. Photonics* **13**, 170 (2019).
- [27] Z. L. Newman, V. Maurice, T. Drake, J. R. Stone, T. C. Briles, D. T. Spencer, C. Fredrick, Q. Li, D. Westly, B. R. Ilic, B. Shen, M.-G. Suh, K. Y. Yang, C. Johnson, D. M. S. Johnson, L. Hollberg, K. J. Vahala, K. Srinivasan, S. A. Diddams, J. Kitching, S. B. Papp, and M. T. Hummon, “Architecture for the photonic integration of an optical atomic clock,” *Optica* **6**, 680 (2019).

- [28] V. Brasch, E. Lucas, J. D. Jost, M. Geiselmann, and T. J. Kippenberg, “Self-referenced photonic chip soliton kerr frequency comb,” *Light Sci. Appl.* **6**, e16202 (2017).

# Chapter 2

## Efficient Second Harmonic Generation at a Targeted Wavelength with Picometer Precision

### 2.1 Motivation

In this section, I motivate the importance of second harmonic generation (SHG) at a targeted frequency or wavelength by alluding to the topic of self-referenced frequency combs. In order for a frequency microcomb to be truly useful and integrated on-chip, there are a number of challenges to overcome: (1) Every comb line should be evenly spaced. (2) The spacing between comb lines should be detectable at electronic frequencies such that it can be locked in a servo. (3) The comb must be broad-band in order to support  $f - 2f$  self-referenced detection of the carrier-envelope offset frequency ( $f_{ceo}$ ). (4) Efficient SHG must be integrated with the comb generation process to enable  $f_{ceo}$  detection.

The challenge of integrating an efficient doubler on-chip ((4) on previous paragraph) is multi-fold. Generally, it is difficult to realize a simultaneously efficient and compact doubler using traditional methods like quasi-phase-matching in a bulk crystal or long waveguide. For this reason, it is advantageous to utilize a microring resonator for SHG, where

double resonance conditions at the fundamental and second harmonic wavelengths, as well as modal phase-matching can be engineered. The difficulty here is that due to the narrow bandwidth of high-Q resonances, it is crucial to align the resonance and phase-matching conditions to the exact wavelengths of interest. In this chapter, a systematic method of achieving this goal is outlined.

## **2.2 Second Harmonic Generation on Aluminum Nitride Microrings**

Aluminum nitride (AlN) is a strong candidate as a material for the integration of a self-referenced soliton microcomb due to its intrinsically strong  $\chi^{(2)}$  and  $\chi^{(3)}$  nonlinearity. In contrast, to date, most successful platforms for stable soliton generation lack a strong  $\chi^{(2)}$  nonlinearity, making it difficult to integrate second harmonic generation onto the same device. Additionally, advances in fabrication methods allow for high-Q and versatile photonic devices to be realized on an AlN platform.

### **2.2.1 Theoretical Description of SHG**

To understand the SHG process in an AlN microring resonator, the theoretical description of the nonlinear process is presented in this subsection. The goal is to derive the equations of motion and to understand the steady state behavior of the process. A schematic of the nonlinear frequency conversion process in the microring resonator along with the relevant coupling, loss and frequency conversion mechanisms is displayed in Fig. 2.1. The

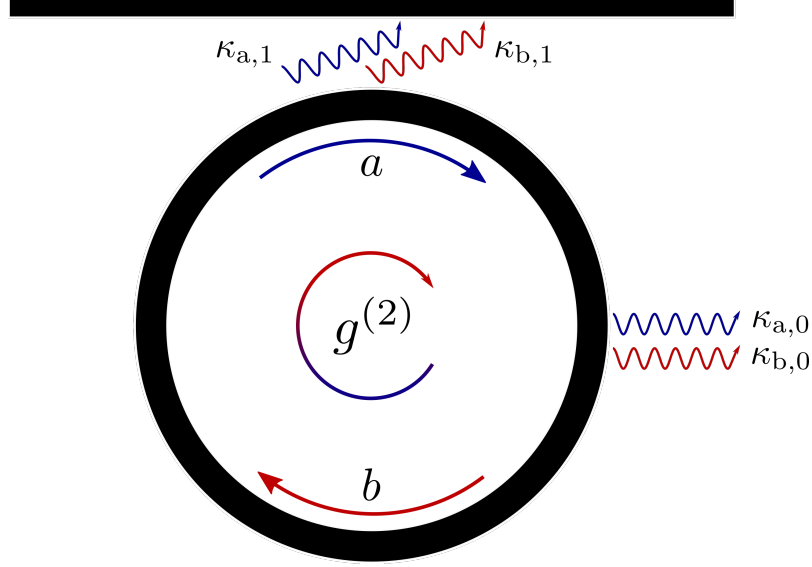


**Figure 2.1: Illustration of SHG in a microring resonator.** Coupling rates ( $\kappa_{c,a(b)}$ ), intrinsic loss rates ( $\kappa_{i,a(b)}$ ) and second order nonlinear coupling strength ( $g^{(2)}$ ). Mode  $a$  refers to the fundamental mode whereas  $b$  is the second harmonic mode.

Hamiltonian of this system can be written as,

$$\begin{aligned} \frac{H}{\hbar} = & \omega_a a^\dagger a + \omega_b b^\dagger b + g^{(2)} \left( a^2 b^\dagger + (a^\dagger)^2 b \right) \\ & + i \sqrt{2\kappa_{a,1}} \frac{P_f}{\hbar\omega_f} \left( -a e^{i\omega_f t} + a^\dagger e^{-i\omega_f t} \right) \end{aligned} \quad (2.1)$$

where  $\omega_f$  is the frequency of the pump laser input,  $P_f$  is its corresponding power in watts,  $a$  and  $b$  are the fundamental and second harmonic modes respectively, and  $\kappa_{a,1}$  is the coupling rate of the fundamental mode to the bus-waveguide. In the rotating frame of  $\omega_f a^\dagger a + 2\omega_f b^\dagger b$ , the Hamiltonian can be simplified as,

$$\check{H} = \delta_a a^\dagger a + \delta_b b^\dagger b + g^{(2)} \left( a^2 b^\dagger + (a^\dagger)^2 b \right) + i\varepsilon_f \left( -a + a^\dagger \right) \quad (2.2)$$

where  $\delta_a = \omega_a - \omega_f$ ,  $\delta_b = \omega_b - 2\omega_f$  and  $\varepsilon_f = \sqrt{2\kappa_{a,1}} \frac{P_f}{\hbar\omega_f}$ . The nonlinear coupling strength  $g^{(2)}$  is related to the  $\chi^{(2)}$  tensor component that couples the fundamental and second harmonic (SH) mode, the phase-matching (the fundamental and SH modes must have equal

phase velocities), as well as the modal overlap. The latter two conditions can be thought of as equivalent concepts where the integral of the electric field overlap across the radial geometry (phase-matching) as well as cross sectional geometry (modal overlap) of the ring resonator must constructively interfere. To put it quantitatively,

$$\begin{aligned}
\hbar g &= \varepsilon_0 \int r dr dz d\theta \chi^{(2)} (u_a^*(r,z))^2 u_b(r,z) e^{i(-2m_a+m_b)\theta} \\
&= \varepsilon_0 2\pi \delta(m_b - 2m_a) \int r dr dz \chi^{(2)} (u_a^*(r,z))^2 u_b(r,z) \\
&= \frac{\sqrt{2} (\hbar \omega_a)^{\frac{3}{2}} \chi^{(2)}}{\sqrt{\varepsilon_0 2\pi R}} \gamma
\end{aligned} \tag{2.3}$$

must be non-vanishing, where

$$\gamma = \frac{\int dr dz (u_a^*(r,z))^2 u_b(r,z)}{\int dr dz \varepsilon_a(r,z) u_a^*(r,z) u_a(r,z) \left( \int dr dz \varepsilon_b(r,z) u_b^*(r,z) u_b(r,z) \right)^{\frac{1}{2}}} \tag{2.4}$$

is the normalized overlap factor.

Finally, applying the Heisenberg equations of motion on the Hamiltonian from Eq. 2.2, the dynamical equations of the fundamental and SH modes are,

$$\frac{d}{dt} a = -i [a, \check{H}] - \kappa_a a = (-i\delta_a - \kappa_a) a - i2ga^*b + \varepsilon_f, \tag{2.5}$$

$$\frac{d}{dt} b = (-i\delta_b - \kappa_b) b - iga^2, \tag{2.6}$$

where the total loss rate of the fundamental and SH modes are respectively  $\kappa_a$  and  $\kappa_b$ . At steady state, assuming non depletion where  $-i2ga^*b \approx 0$ , we can solve for the collected SHG power at the waveguide,

$$P_{b,out} = |-\sqrt{2\kappa_{b,1}}b|^2 \hbar \omega_b = g^2 \left( \frac{2\kappa_{b,1}}{\delta_b^2 + \kappa_b^2} \right) \left( \frac{2\kappa_{a,1}}{\delta_a^2 + \kappa_a^2} \right)^2 \left( \frac{1}{\hbar \omega_f} \right)^2 \hbar \omega_b. \tag{2.7}$$

Importantly, we see that the second harmonic generation efficiency is proportional to the reciprocal of the SH mode loss rate, and to the square of the fundamental mode's.

## 2.2.2 Phase, Resonance and Energy Matching Conditions

Due to the small bandwidth of a microring SH doubler, it is critical to understand the many dependencies of the phase-matching wavelength in order to finely tune the SHG efficiency to be at a target wavelength. In general for a ring resonator with width  $w$  radius  $R$ , effective index  $n_{eff}^{(qf)}$  where  $q \in 1, 2$  denotes fundamental or SH mode, and orbital angular momentum (OAM)  $m$ , the resonance condition follows,

$$2\pi n_{eff}(\lambda)R = mq\lambda^{(qf)} \quad (2.8)$$

Allowing the wavelength to vary in the vicinity of a constant  $\lambda_0$ , Eq. 2.8 becomes

$$2\pi R \left( n_{eff}^{(qf)} + \frac{\partial n_{eff}^{(qf)}}{\partial \lambda} \delta \lambda^{(qf)} \right) = mq \left( \lambda_0^{(qf)} + \delta \lambda^{(qf)} \right) \quad (2.9)$$

where we can then express  $\delta \lambda^{(qf)}$  as

$$\delta \lambda^{(qf)} = \frac{n_{eff} - \frac{mq\lambda_0}{2\pi R}}{\frac{mq}{2\pi R} - \frac{\partial n_{eff}}{\partial \lambda}} \quad (2.10)$$

with a variation relation dependent on  $w$ ,  $T$ ,  $R$  and  $m$  according to

$$\begin{aligned} d\lambda^{(qf)} &= \left( \frac{\partial \delta \lambda^{(qf)}}{\partial w} \frac{\partial w}{\partial \lambda^{(qf)}} + \frac{\partial \delta \lambda^{(qf)}}{\partial T} \frac{\partial T}{\partial \lambda^{(qf)}} + \frac{\partial \delta \lambda^{(qf)}}{\partial R} \frac{\partial R}{\partial \lambda^{(qf)}} + \frac{\partial \delta \lambda^{(qf)}}{\partial m} \frac{\partial m}{\partial \lambda^{(qf)}} \right) \delta \lambda^{(qf)} \\ &\approx A^{(qf)} dw + B^{(qf)} dT + C^{(qf)} dR + D^{(qf)} dm \end{aligned} \quad (2.11)$$

here the coefficients are expressed as,

$$\begin{aligned}
A^{(qf)} &= \frac{1}{n_g^{(qf)}} \frac{\partial n_{eff}^{(qf)}}{\partial w} \\
B^{(qf)} &= \frac{1}{n_g^{(qf)}} \frac{\partial n_{eff}^{(qf)}}{\partial T} \\
C^{(qf)} &= \frac{\pi q m \left( n_{eff}^{(qf)} - \frac{\partial n_{eff}^{(qf)}}{\partial \lambda} \right)}{\left( n_g^{(qf)} \right)^2 2\pi R^2} \\
D^{(qf)} &= \frac{q n_{eff}^{(qf)}}{\left( n_g^{(qf)} \right)^2 2\pi R} dm
\end{aligned} \tag{2.12}$$

From our empirical observations,  $n_g^{(qf)} \gg 1$ , such that  $A, B, C, D$  can be effectively treated as constants. Furthermore, the energy matching condition is

$$\begin{aligned}
\Delta\lambda(m, \delta R, \delta w, \delta T) &= d\lambda_{2f} - \frac{1}{2} d\lambda_f = 0 \\
&\approx \left( \frac{\frac{\partial n_{eff}^{(2f)}}{\partial w}}{\frac{2m}{2\pi R} - \frac{\partial n_{eff}^{(2f)}}{\partial \lambda}} - \frac{\frac{\partial n_{eff}^{(f)}}{\partial w}}{\frac{2m}{2\pi R} - \frac{2\partial n_{eff}^{(f)}}{\partial \lambda}} \right) dw \\
&+ \left( \frac{\frac{\partial n_{eff}^{(2f)}}{\partial T}}{\frac{2m}{2\pi R} - \frac{\partial n_{eff}^{(2f)}}{\partial \lambda}} - \frac{\frac{\partial n_{eff}^{(f)}}{\partial T}}{\frac{2m}{2\pi R} - \frac{2\partial n_{eff}^{(f)}}{\partial \lambda}} \right) dT \\
&+ \left( \frac{n_{eff}^{(2f)} \pi m}{\left( m - \frac{\partial n_{eff}^{(2f)}}{\partial \lambda} \pi R \right)^2} - \frac{n_{eff}^{(f)} \pi m}{\left( m - \frac{\partial n_{eff}^{(f)}}{\partial \lambda} 2\pi R \right)^2} \right) dR
\end{aligned} \tag{2.13}$$

where given  $T$  and  $w$ , since usually we must use a specific temperature and width for satisfying phase-matching conditions, the energy matching condition is satisfied when

$$\left( \frac{\frac{\partial n_{eff}^{(2f)}}{\partial w}}{\frac{2m}{2\pi R} - \frac{\partial n_{eff}^{(2f)}}{\partial \lambda}} - \frac{\frac{\partial n_{eff}^{(f)}}{\partial w}}{\frac{2m}{2\pi R} - \frac{2\partial n_{eff}^{(f)}}{\partial \lambda}} \right) \delta w = -\Delta\lambda(m, 0, 0, 0) \tag{2.14}$$



By obtaining the coefficients in Eq. 2.12 through empirical analysis or simulations, it is possible to engineer a microring resonator with phase-matching and energy matching conditions that coincide at a targeted wavelength.

## 2.3 Second Harmonic Generation at a Target Wavelength

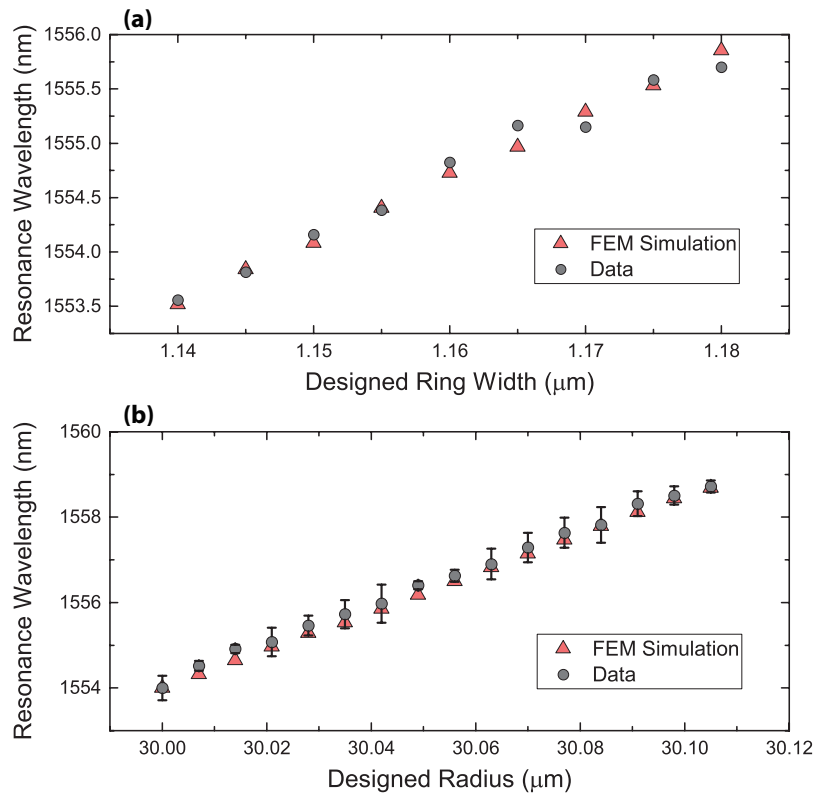


**Figure 2.2:** (a) Analysis of the phase-matching condition across different widths. Simulation included details of the cross sectional geometry of the ring, with a sidewall angle of 8 degrees. The refractive index curve of our material was measured by an ellipsometer. The experimental data agrees with the simulated data reasonably well. (b) Analysis of the resonance wavelength at varying radii.

To maximize yield of high efficiency SHG devices at the desired wavelength, several AlN chips containing arrays of devices (connected along the same bus-waveguide) as depicted in Fig. 2.4 were fabricated to simultaneously optimize for multiple param-

ters. These parameters are, ring width and ring radius. The effect of the ring width on the resonance wavelength shift as well as the relationship between the radius and resonance wavelength are depicted in Fig. 2.3(a) and Fig. 2.3(b) respectively. Moreover, the impact of the ring width on the effective index of both the fundamental and SH modes and the phase-matching window of the SHG is crucial to the design parameters and will be detailed throughout the following paragraphs. Finally, we note that the temperature of the environment is also an important degree of freedom that will ultimately be used to fine-tune the optimal SH wavelength to the specific wavelength of choice.

Here we address two main design challenges: (1) The simultaneous coupling to both the fundamental and SH wavelengths, which must be done in an efficient manner, (2) the coincidence of resonant wavelengths at the fundamental and SH wavelengths at the desired frequency of the two-photon transition of  $^{85}\text{Rb}$  at  $\lambda_{\text{Rb}} = 1556.24 \text{ nm}$ . This transition frequency was used due to its important applications in optical clockwork technologies. The first challenge has been addressed previously by a number of publications, where separately optimized waveguides with varying structural designs (wrap-around angles and waveguide widths) were used to interrogate the visible and telecom light efficiently<sup>1-3</sup>.

The second challenge mentioned in the preceding paragraph is a significant one due to the inability of the fundamental and SH resonant wavelength to be independently addressed by a single one of the many degrees of freedom (DoFs). In order to solve this, all DoFs were had to be varied based on theoretical predictions and empirically observed parameters. By utilizing all DoFs, independent control of resonance frequencies spectrally far apart is possible.

From the variation relation of 2.11, we note that the coefficients from 2.11 can be treated as constants since  $n_g^{(qf)} = \frac{qm}{2\pi R} - \frac{\partial n_{eff}^{(qf)}}{\partial \lambda} \gg 1$ . The coefficients were empirically observed to be  $A^{(1f)} \approx 0.055 \pm 0.0028$  and  $C^{(1f)} \approx 0.043 \pm 0.00053$ . This is illustrated more clearly in Fig. 2.3. The resonant mode was simulated using COMSOL, using different ring widths and ring radii, while considering the microring as a waveguide cross-section with

radial symmetry. The mode number was set to be 226, and the eigen-frequencies at different radii and ring widths were simulated and plotted as red triangles in Fig. 2.3, which agree reasonably well with experimental data. The thermal-shift coefficient of the telecom resonance was  $B^{(1f)} = 0.019 \pm 0.00031$  nm/K. FSR of the IR modes correspond to the coefficient value of  $D^{(1f)}$  which was estimated to be about 5.84.

For the phase-matching condition to be met, the condition  $d\lambda^{(1f)} = 2d\lambda^{(2f)}$  must be observed. We can see that for fixed values of  $R$  and  $T$ , and for  $\Delta m = 1$ , the phase-matching point experiences a wavelength shift of  $D^{(1f)} - A^{(f)} \frac{D^{(1f)} - 2D^{(2f)}}{A^{(1f)} - 2A^{(2f)}}$ , with  $dw = -\frac{D^{(1f)} - 2D^{(2f)}}{A^{(1f)} - 2A^{(2f)}}$ . The rate of shift in  $dw$  is  $\sim 2.8 \pm 0.026$  as illustrated in Fig. 2.3(a) and (b). The visible TM<sub>02</sub> mode existing within the resonator which is closest in frequency to  $2\lambda_{\text{Rb}}$  was selected with a maximum deviation of  $\frac{1}{2}D^{(1f)}$ . Meanwhile, the parameters  $w$ ,  $R$  and  $T$  were varied to align the fundamental and SH modes. In order to tune the resonance by  $\frac{1}{2}D^{(1f)}$ , experimentally, the change in width, temperature or radius needed was respectively  $9D^{(1f)}$  nm,  $26D^{(1f)}$  K, or  $11.5D^{(1f)}$  nm. The requirement for phase-matching is given by  $(A^{(f)} - 2A^{(2f)})dw + (B^{(f)} - 2B^{(2f)})dT + (C^{(f)} - 2C^{(2f)})dR = 0$ .

Guided by the analysis of phase-matching conditions, we are able to control  $w$ ,  $T$ , and  $R$  to optimize the SHG output such that  $\lambda^{(2f)} = \lambda_{\text{Rb}}(d\lambda^{(2f)} = 0)$ . For each device, the  $w$  and  $R$  are fixed by fabrication, while  $T$  is real-time adjustable using an external heater. Since the thermo-shift coefficients are relatively small for aluminum nitride, i.e.,  $(B^{(1f)}, B^{(2f)})$ , thermal adjustments were used as a fine-tuning approach whereas the geometrical DoFs  $w$  and  $R$  were varied for coarse tuning.

In order to conduct experimental observations of the resonance wavelength shift coefficients, a number of preliminary chips were fabricated. For these chips, the width of the microrings was varied from  $1.13 - 1.18 \mu\text{m}$  at intervals of 10 nm. This provided the exact ring widths that exhibit optimal phase-matching conditions in the range of a tunable telecom laser at  $1520 - 1570$  nm. By analyzing the data from three separate chips, the optimal widths were found to be between  $1.13 - 1.17 \mu\text{m}$ , depending on the exact height

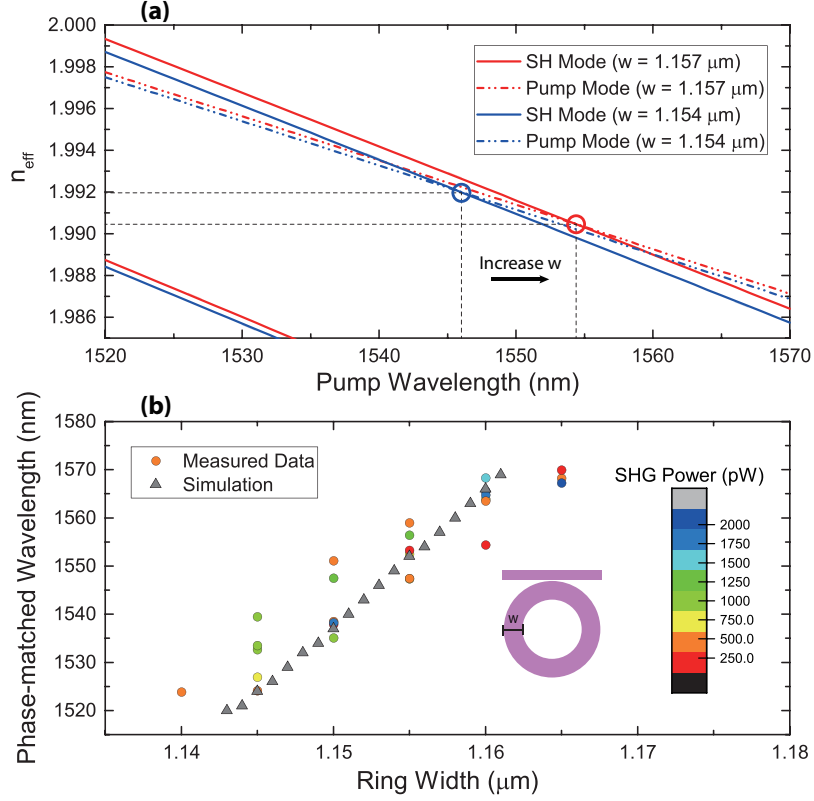


**Figure 2.3:** (a) Dependence of the phase-matched wavelength as the ring width increases. Phase-matching wavelengths tend to occur at larger pump wavelengths as ring widths increase. (b) Comparison of the simulated and measured phase-matched wavelengths with the designed ring width. Measured data is color coded by SHG output power as described by the color scale.

of the AlN, which can vary slightly between chips. With this result, the ring width for the final chip design was varied in a narrower range, at a finer gap of 5 nm. Finally, it was observed that the SHG output wavelength has a bandwidth of  $\sim 7$  nm for each array of microrings. Therefore, through our careful designing of the parameters of a single chip, phase-matching can be realized for any wavelength within the bandwidth of the laser in every fabricated chip.

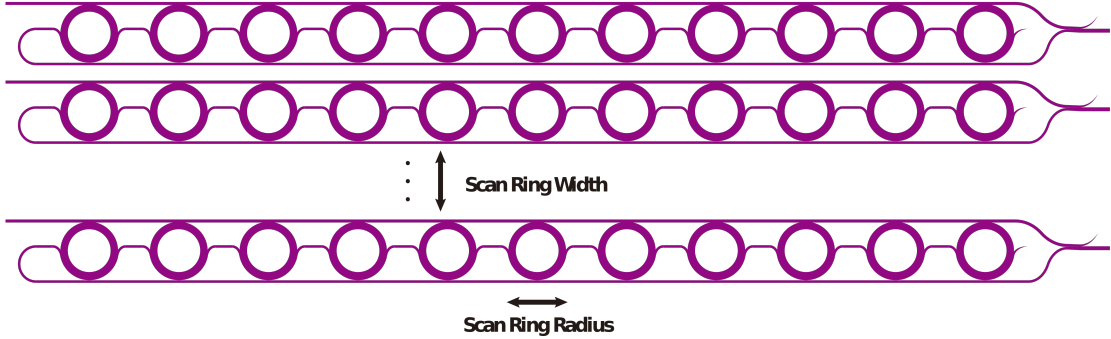
Maximizing the yield of devices was not a simple task and required a number of iterations. However, the process was greatly simplified due to guidance from simulations. We designed each device to consist of a cascade of 16 rings as shown in Fig. 2.4, where the radius of every ring is different, at a step size of 7 nm from ring to ring. Again shown in

Fig. 2.3(b), each radius step corresponded to a  $36 \pm 3.7$  pm shift of resonance mode wavelength, corresponding to one cascade of devices covering a span of 5.7 nm, along with a radius change of over 100 nm. For the final chip design, where the data was measured from, the sweeping range of ring width further narrowed to 1.15 – 1.17  $\mu$ m. The specific working device with the targeted wavelength of phase-matching had a designed ring width of 1.155  $\mu$ m and a radius of 30.035  $\mu$ m.

As shown from numerous previous studies<sup>??</sup>, the doubly-resonant SHG efficiency  $\eta$  in a non pump-depleted regime can be expressed as

$$\eta = \frac{P_{SH}}{P_p^2} = g^2 \frac{4\kappa_{SH,1}}{\delta_{SH}^2 + (\kappa_{SH})^2} \left( \frac{2\kappa_{p,1}}{\delta_p^2 + (\kappa_p)^2} \right)^2, \quad (2.15)$$

Here,  $g$  is the nonlinear coupling rate,  $\kappa_{SH(p),0}$  and  $\kappa_{SH(p),1}$  are respectively the SH (pump) mode intrinsic loss and external coupling rates. In order to optimize phase-matching



**Figure 2.4:** A schematic of the device, where the ring radius is varied across a single device and the ring width is varied across devices. Over 300 of microrings can be fit onto a single chip, which can guarantee an optimized phase-matching in a desired wavelength, assuming fixed height and bulk refractive index profile.

and SH output at the targeted wavelength of  $\lambda_{RB}$ , the following requirements were strictly followed. (1) Since for most applications such as carrier envelope offset frequency detection and optical clockworks, the input power is usually on the order of –20 dbm, the SHG

process is operating at the non-depletion regime. Therefore, the ring-coupler configurations should be critically coupled in both the IR and SH modes for optimal SH efficiency. For our designs, a straight bus waveguide of  $0.57\ \mu\text{m}$  width was used for the coupling of IR light, and is tapered to  $3\ \mu\text{m}$  to facilitate coupling to a lens or fiber input/output. (2) Since the extraction of SH light through the IR bus is inefficient, a wrap-around waveguide which was designed to taper from  $0.17 - 0.12\ \mu\text{m}$  was used to couple to the visible SH mode of the ring resonator. This waveguide was bent around to guide the extracted SH light towards the output end of the chip (shown in Fig. 2.4). Finally, an integrated wavelength division multiplexer was used to combine IR and Visible light onto the same output waveguide. (3) The detuning of SH light and IR pump input  $\delta_{SH(p)}$  must be as close to zero as possible by the fine tuning of temperature using an external (or an integrated on-chip) heater.

Due to the differences of thermo-shift coefficient at telecom wavelengths versus visible wavelengths for polycrystalline AlN material, we utilize this effect in aligning the dual resonances<sup>3-5</sup>. The effect of the differential thermal effects on the detuning between the visible and IR modes and thus the SHG power is shown in Fig. 2.5(a). This behavior is modeled by the following equation,

$$\eta \approx \frac{\hbar\omega_{SH}}{(\hbar\omega_p)^2} \frac{8g^2\kappa_{SH,1}\kappa_{p,1}^2}{\kappa_p^4 \left[ \frac{2\pi c}{\lambda_p\lambda_{SH}} (\lambda_\Delta - d_\Delta T)^2 + \kappa_{SH}^2 \right]}. \quad (2.16)$$

The wavelength mismatch in the visible and IR resonances is effectively compensated by the differing thermo-shift coefficients  $d_\Delta$  between the SH and pump modes at temperature  $T$ . At the external temperature where  $\lambda_\Delta - d_\Delta T = 0$ , maximum SHG power can be observed due to a perfect alignment of resonances and phase-matching. For our specific champion device, this temperature was observed to be at  $110^\circ\text{C}$  with a full-width at half maximum (FWHM) of  $\Delta T = 17.5^\circ\text{C}$ . The FWHM in the wavelength scale is observed to be  $0.303 \pm 0.068\text{nm}$ . At  $110^\circ\text{C}$ , the measured IR transmission spectrum and visible

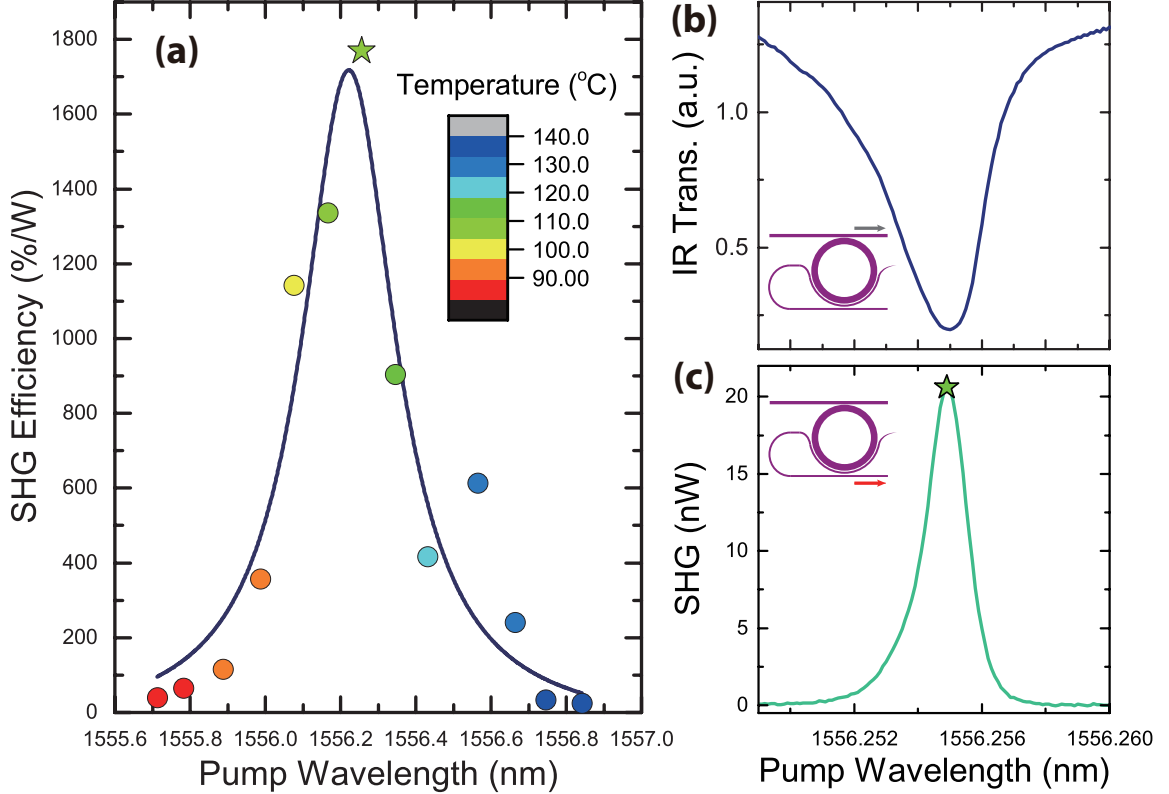


**Figure 2.5:** (a) Shows the temperature dependent SH response on both a wavelength scale and the correspondingly transformed temperature scale using the thermo-shift coefficient of polycrystalline AlN at the IR wavelengths, assuming the coefficient is constant. A maximum internal efficiency of 1800%/W was observed at a wavelength of 1556.2 nm (110°C) with a 3 dB bandwidth (FWHM) of  $0.303 \pm 0.068$  nm (17.5°C). Each data point is color coded by its corresponding temperature as shown by the color scale-bar. (b) A zoomed-in spectrum of the transmission at 110°C. (c) SHG at a fixed temperature of 110°C, with the peak SH power observed at the visible wavelength corresponding to  $\lambda_{Rb}$ .

response can be seen in Fig. 2.5(b). For the IR mode resonance, a loaded  $Q \approx 3 \times 10^5$  was measured with an extinction ratio of 0.8. The maximum SH response observed was 20 nW at a center wavelength of 1556.255 nm and a FWHM of 1.5 pm, corresponding to a maximum on-chip efficiency of 1800%/W. The input power of the pump laser was set to  $180 \mu\text{W}$ . We note that further optimization of the coupling conditions for critical coupling of the modes can be expected to further improve the SHG efficiency.

## 2.4 Future Work and Conclusions

In conclusion, there are many applications that could potentially benefit from a highly efficient, on-chip integrated SHG at a targeted wavelength. In this work, we performed systematic simulations and theoretical analysis on the effect of geometrical variations of a polycrystalline AlN microring resonator on modal phase-matching of SHG. In conjunction with data analysis from multiple chip designs, we realized a robust procedure of designing a phase-matched second-harmonic generator (microring) for any targeted wavelength in the telecom-band. As a proof of principle for applications in ultra-stable clock designs, we used the two photon transition of rubidium-85 ( $^{85}\text{Rb}$ ), at a wavelength of 778.12 nm. The systematic approach is useful for designs where doubly- or even triply-resonant conditions are required. This work generalises to other on-chip material platforms for frequency conversion at targeted wavelengths.

## References

- [1] X. Guo, C.-L. Zou, and H. X. Tang, “Second-harmonic generation in aluminum nitride microrings with 2500%/w conversion efficiency,” *Optica* **3**, 1126 (2016).
- [2] A. W. Bruch, X. Liu, X. Guo, J. B. Surya, Z. Gong, L. Zhang, J. Wang, J. Yan, and H. X. Tang, “17 000%/w second-harmonic conversion efficiency in single-crystalline aluminum nitride microresonators,” *Appl. Phys. Lett.* **113**, 131102 (2018).
- [3] X. Guo, C.-L. Zou, and H. X. Tang, “70 db long-pass filter on a nanophotonic chip,” *Opt. Express* **24**, 21167 (2016).
- [4] J. B. Surya, X. Guo, C.-L. Zou, and H. X. Tang, “Efficient third-harmonic generation in composite aluminum nitride/silicon nitride microrings,” *Optica* **5**, 103 (2018).
- [5] J. B. Surya, X. Guo, C.-L. Zou, and H. X. Tang, “Control of second-harmonic generation in doubly resonant aluminum nitride microrings to address a rubidium two-photon clock transition,” *Opt. Lett.* **43**, 2696 (2018).



# Chapter 3

## Third Harmonic Generation on a Hybrid Aluminum Nitride/Silicon Nitride Platform

### 3.1 Motivation

Aluminum Nitride (AlN) and stoichiometric Silicon Nitride ( $\text{Si}_3\text{N}_4$ , or SiN from hereon) have both emerged as important nonlinear materials in the past decade. AlN has been instrumental in the advancement of next generation on-chip frequency doublers, having broken records in efficiencies during the times the works were first published. In addition to having a relatively strong  $\chi^{(2)}$  nonlinearity, AlN also exhibits  $\chi^{(3)}$  Kerr nonlinearity. Although the material possesses both second order and third order nonlinearities, the maturity of AlN as a platform for comb generation has consistently lagged behind SiN. SiN on the otherhand, has a comparatively larger  $\chi^{(3)}$  coefficient, mature fabrication technologies, and has recently enjoyed a variety of technological advances<sup>1-4</sup>. This has led to its strong growth and is often the material of choice in the field of soliton microcomb generation. The one weakness of SiN is the crystal's centro-symmetric structure which prohibits intrinsic second order nonlinear effects on electric fields. This subsequently means that it

is difficult to integrate  $f - 2f$  self-referencing with broadband soliton microcomb generation on an all-SiN platform. To do so, one must employ special techniques to break the inversion symmetry, such as the use electric-field induced second order effects (a DC Kerr  $\chi^{(3)}$  effect), or stress-induced symmetry breaking<sup>5-8</sup>.

Another method of integrating both soliton microcomb generation and self-referencing is to utilize a hybrid material platform. In this chapter, a hybrid AlN on SiN platform is introduced. Here, it is demonstrate that both efficient SHG and third harmonic generation (THG) can be achieved. Such a platform can be extremely valuable to the simultaneously integrating self-referencing and comb generation. Not only can SiN provide the mature platform for soliton microcombs, the demonstration of high efficiency SHG and THG on this platform offers a unique advantage the ability to potentially realize  $2f - 3f$  self referencing, which can relax the bandwidth requirement of the microcomb in determining the  $f_{ceo}$ .

## 3.2 Doubly Resonant Third Harmonic Generation in Aluminum Nitride/Silicon Nitride Microrings

### 3.2.1 Theoretical Description

#### Self-referencing of a soliton microcomb

We can express all modes of a frequency comb as:

$$f_n = f_{ceo} + n\Delta f, \quad (3.1)$$

where the FSR or the resonator is expressed as  $\Delta f$ . In  $f-2f$  self-referencing, the beat-note of a doubled  $n^{\text{th}}$  comb line with the  $2n^{\text{th}}$  comb line yields the carrier envelope frequency

offset  $f_{ceo}$ , which is explicitly

$$2f_n - f_{2n} = 2(f_{ceo} + n\Delta f) - (f_{ceo} + 2n\Delta f) = f_{ceo}, \quad (3.2)$$

where we can see that in order for this scheme to be effective, the  $n^{\text{th}}$  and the  $2n^{\text{th}}$  comb line must be detectable with acceptable signal-to-noise ratio. Therefore for this  $f - 2f$  self-referencing, the frequency comb bandwidth must span an octave.

In a  $2f - 3f$  self-referencing scheme, the expression that relates SHG and THG to the  $f_{ceo}$  becomes

$$3f_n - 2f_m = 3(f_{ceo} + n\Delta f) - 2(f_{ceo} + m\Delta f) = f_{ceo}, \quad (3.3)$$

such that the condition  $3n = 2m$  or  $3n = 2m \pm 1$  must be met. This corresponds to a  $2/3$  octave spanning bandwidth requirement, considerably relaxing the one needed for the  $f - 2f$  scheme.

### THG Equations of Motion

The analysis for THG takes inspiration from that of SHG, starting from the system Hamiltonian

$$H = \omega_a a^\dagger a + \omega_b b^\dagger b + g \left( (a^\dagger)^3 b + a^3 b^\dagger \right) + \epsilon_p \left( a e^{i\omega_p t} + a^\dagger e^{-i\omega_p t} \right), \quad (3.4)$$

where  $g$  has an expression given by

$$g \approx \frac{\zeta \sqrt{3} \hbar \omega_a^2 \chi^{(3)}(r)}{\epsilon_0 2\pi R \sqrt{\epsilon_a^3 \epsilon_b}} \delta(m_b - 3m_a), \quad (3.5)$$

and is once again dependent on a modal overlap factor

$$\frac{\int \int dr dz [u_{a,z}^*(r,z)]^3 u_{b,z}(r,z)}{[\int \int dr dz |u_{a,z}(r,z)|^2]^{3/2} [\int \int dr dz |u_{b,z}(r,z)|^2]^{1/2}}. \quad (3.6)$$

We can perform the same analysis on the Hamiltonian 3.4 as in the previous chapter on Eq. 2.2, and arrive at the equations of motion,

$$\begin{aligned} \frac{d}{dt}a &= -(i\delta_a + \kappa_a)a - i3g(a^*)^2b + \varepsilon_f \\ \frac{d}{dt}b &= -(i\delta_b + \kappa_b)b - iga^3, \end{aligned} \quad (3.7)$$

where modes  $a$  and  $b$  are the fundamental and TH mode respectively,  $\varepsilon_f$  represents the coupling rate of the pump input power,  $\delta_{a(b)}$  is the detuning of the pump input frequency from the mode frequency, and  $\kappa_{a(b)}$  is the total loss rate.

### THG efficiency and thermal nonlinearity

From the input-output relations at steady state, the output TH mode can be expressed as

$$b_{out} = -\sqrt{2\kappa_{b,l}}b = \frac{-i\sqrt{2\kappa_{b,l}}g|a|^3}{-i\delta_b - \kappa_b} \quad (3.8)$$

The output power and efficiency of THG can be subsequently evaluated as

$$P_{b,out} = |b_{out}|^2 \hbar\omega_b = g^2 \hbar\omega_b \frac{2\kappa_{b,l}}{\delta_b^2 + \kappa_b^2} \left( \frac{2\kappa_{a,l}}{\delta_a^2 + \kappa_a^2} \right)^3 \left( \frac{P_f}{\hbar\omega_f} \right)^3 \quad (3.9)$$

$$\eta_{THG} = \frac{P_{b,out}}{P_f^3} = g^2 \hbar\omega_b \frac{2\kappa_{b,l}}{\delta_b^2 + \kappa_b^2} \left( \frac{2\kappa_{a,l}}{\delta_a^2 + \kappa_a^2} \right)^3 \left( \frac{1}{\hbar\omega_f} \right)^3 = g^2 \frac{16Q_a^3 Q_b}{\hbar^2 \omega_a^6}. \quad (3.10)$$

The nonlinear  $\chi^{(3)}$  tensor components governing the TH transition is small. Thus, higher input power is generally needed to observe THG, where the thermal nonlinearity

of the microring resonator modes must be considered. In the following analysis we make the assumption that the term corresponding to third order down-conversion to be weak and can be ignored, such that the coupled equations due to the thermal effect are









$$\frac{d}{dt}a = -i(\delta_a - i\kappa_a - g_T\Delta T)a - i\kappa_{a,l}\varepsilon_p \quad (3.11)$$

$$\frac{d}{dt}\Delta T = K|a|^2 - \gamma_{th}\Delta T. \quad (3.12)$$

Due to the fast response time of thermal relaxation for the purpose of our studies, we can assume steady state for both of the above equations and numerically solve for the bistability curve of mode  $a$ , which is the source of the experimentally observed triangularly shaped pump laser transmission curve.

### 3.3 Optimization of Third Harmonic Generation

**Table 3.1: Phase matched widths from simulations with the respective mode profiles and calculated overlap factor  $\zeta$ .**

Ring Width ( $\mu\text{m}$ )	1.34	1.45	1.49	1.68	1.86	1.99	2.20	2.30
	i.	ii.	iii.	iv.	v.	vi.	vii.	viii.
Simulated Mode Profile								
Calculated Overlap Factor	0.15	0.28	0.11	0.54	0.52	0.48	0.21	0.14

From the previous analysis, there are two conditions that need to be met in order to improve the THG efficiency: (1) The effective indices of the IR and visible mode must be matched through careful design of the geometry. (2) The efficiency scales with the squared overlap factor, and therefore choosing a higher order mode which has a large field overlap with the fundamental mode is crucial. Finally, the structural design of the microring is an important consideration in the optimization of the efficiency as well. The

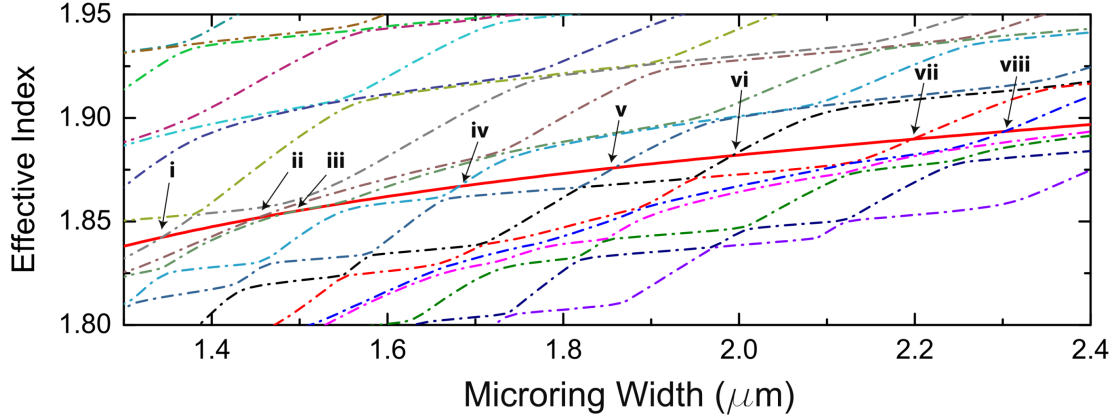


**Figure 3.1:** Effective index of the fundamental TE mode of the fundamental (solid red curve) and higher order modes of the third harmonic light (dotted curve) with varying ring widths. The intersecting points of the red curve with the other lines denote the ring widths that satisfy the phase matching. The phase-matched TE modes are marked with the corresponding labels from Table 3.1.

diameter of the ring resonator was  $40 \mu\text{m}$ , with a hybrid  $330 \text{ nm}$  sputtered polycrystalline AlN on  $330 \text{ nm}$  of low pressure chemical vapor deposited (LPCVD)  $\text{Si}_3\text{N}_4$ . The degrees of freedom used in the optimization process was the ring width, and modal dispersion engineering. However, we note there can be many more alternative methods one may employ to further optimize the structure for THG such as the design of a step-stool.

Due to the dispersion of nanophotonic waveguides, modal optimization of phase-matching is required. It is also important choose a high order TH mode with a large modal overlap with the fundamental mode. Table 3.1 lists various simulated cross sectional TE mode profiles in increasing order of the ring width from the commercial mode solver FIMMWAVE. The Roman numerals indicated below the ring widths are corresponding to the intercepts between the fundamenal TE (solid curve) and higher order TE (dotted curves) modes on Fig. 3.1. Based on calculations of the modal overlap, it was theoretically predicted that the higher order mode at  $1.86 \mu\text{m}$  would produce the highest efficiency THG. Fabrication of the device was guided by this realization.

### 3.4 Fabrication

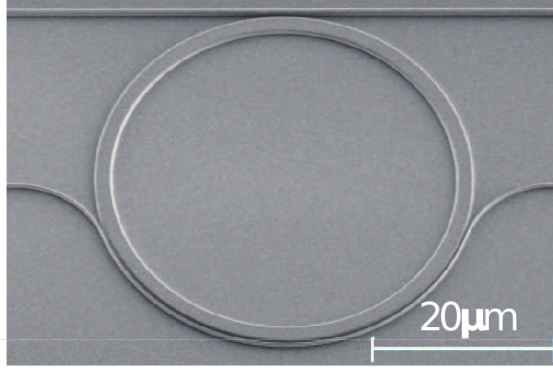


**Figure 3.2:** SEM micrograph of a ring resonator device on the hybrid material platform

The AlN/Si<sub>3</sub>N<sub>4</sub> layers were grown and sputtered on top of a 3.3 µm thick silicon dioxide substrate. First the pattern design was defined by electron beam lithography using a FOX16 resist and MF312 as a developing agent. Then the AlN layer was dry etched using a BCl<sub>3</sub>/Cl<sub>2</sub>/Ar recipe, followed by the Si<sub>3</sub>N<sub>4</sub> dry etching using a CHF<sub>3</sub>/O<sub>2</sub> chemistry. Finally, a layer of silicon dioxide was deposited on top using plasma-enhanced chemical vapor deposition (PECVD) as a top cladding layer. Under the BCl<sub>3</sub>/Cl<sub>2</sub>/Ar chemistry, AlN etches three times faster than Si<sub>3</sub>N<sub>4</sub>. Therefore, the two-step etching processes using an Oxford-100 tool was developed with finely adjusted etch times and chemical ratios to create the smoothest possible sidewall. We note that this ratio will be highly dependent on the condition of the tool used. Additionally, the devices were annealed at a temperature of 950 °C for 1 hour, after which the IR optical mode intrinsic Q were empirically observed to yield an improvement of a factor of around two, with an observed value of  $Q_{a,0} \approx 4 \times 10^5$ . An SEM micrograph of the device before the deposition of the top cladding layer is displayed in Fig. 3.2

### 3.5 Results and Discussion

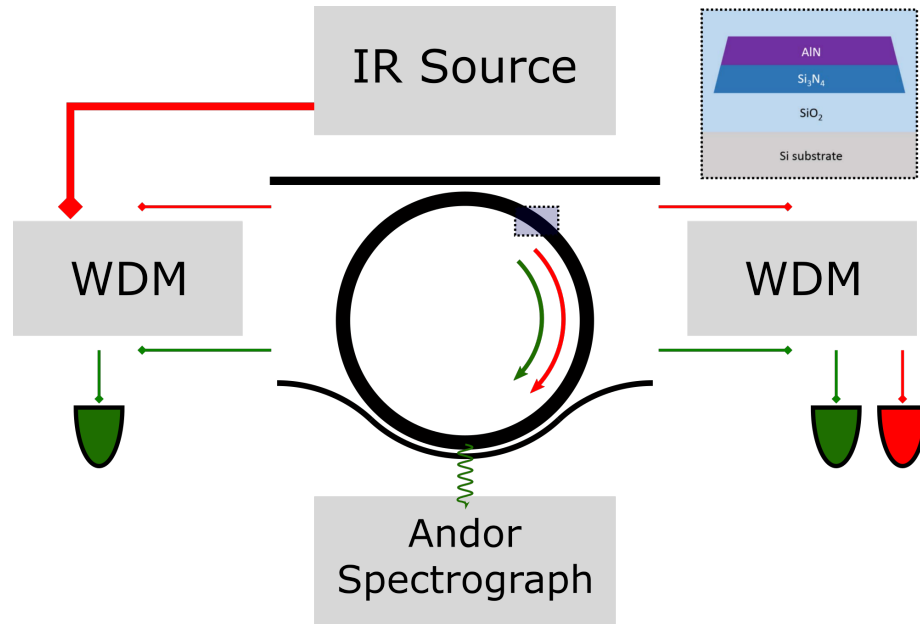


**Figure 3.3:** Schematic of the experimental setup, where the dotted box indicates the cross section of the device under test. A wavelength demultiplexer on the input and output side of the device captures the TH visible signal (green) as well as the transmitted IR signal (red) which is then received by the photodetectors. The scattered light from the microring is collected by the Andor Spectrograph, a spectrometer located directly atop the device.

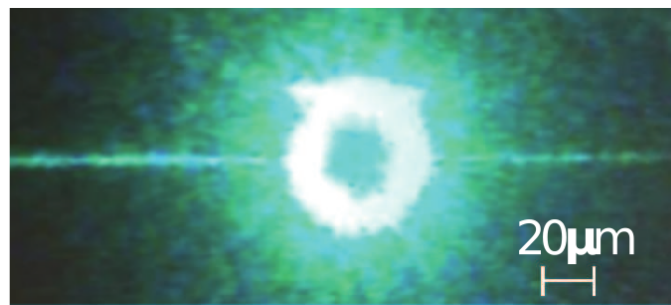


**Figure 3.4:** Photographed top view of the TH light scattered from the ring.



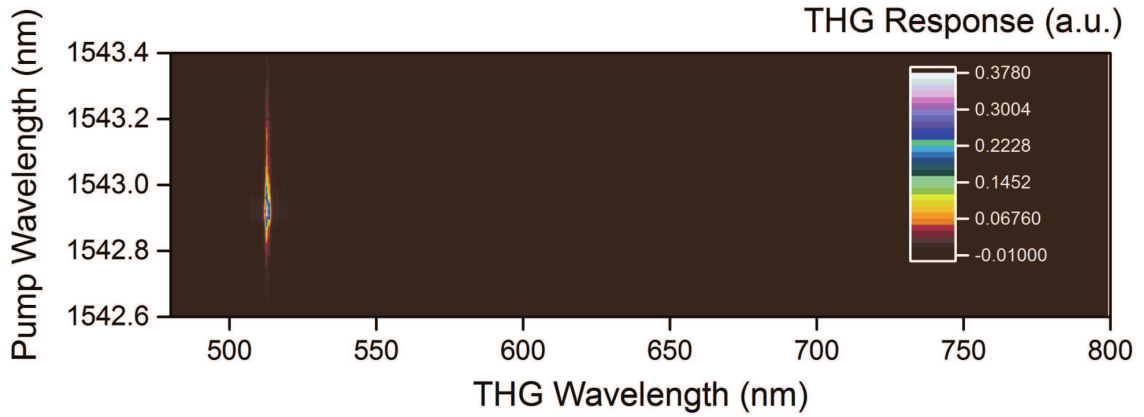


**Figure 3.5:** Third harmonic generation spectrum with respect to input pump wavelength. Data was taken using the Andor spectrograph 193i. At each pump wavelength input, TH light scattered from the ring was collected by the spectrograph with a slit opening of  $50\ \mu\text{m}$  and an integration time of one second. The linewidth of the THG wavelength is due to the limit in resolution of the Andor Spectrograph. No signal was captured at other visible wavelengths, suggesting a pure third harmonic process and not a cascaded second order process at play.

For the optimized device, separate waveguides including a bus designed for efficient coupling to the IR mode and a wrap-around coupler for the high order TH visible mode were used. The ring width was  $1.85\ \mu\text{m}$ , which is in good agreement with the simulated value of  $1.86\ \mu\text{m}$ . The extraction coupler for visible light had a wrap-around angle of 60 degrees and was tapered from a width of  $0.12$  to  $0.17\ \mu\text{m}$ . The gap between between the coupler and the ring was varied from  $0.3$  to  $0.5\ \mu\text{m}$ , with the highest THG efficiency observed at  $0.3\ \mu\text{m}$ .

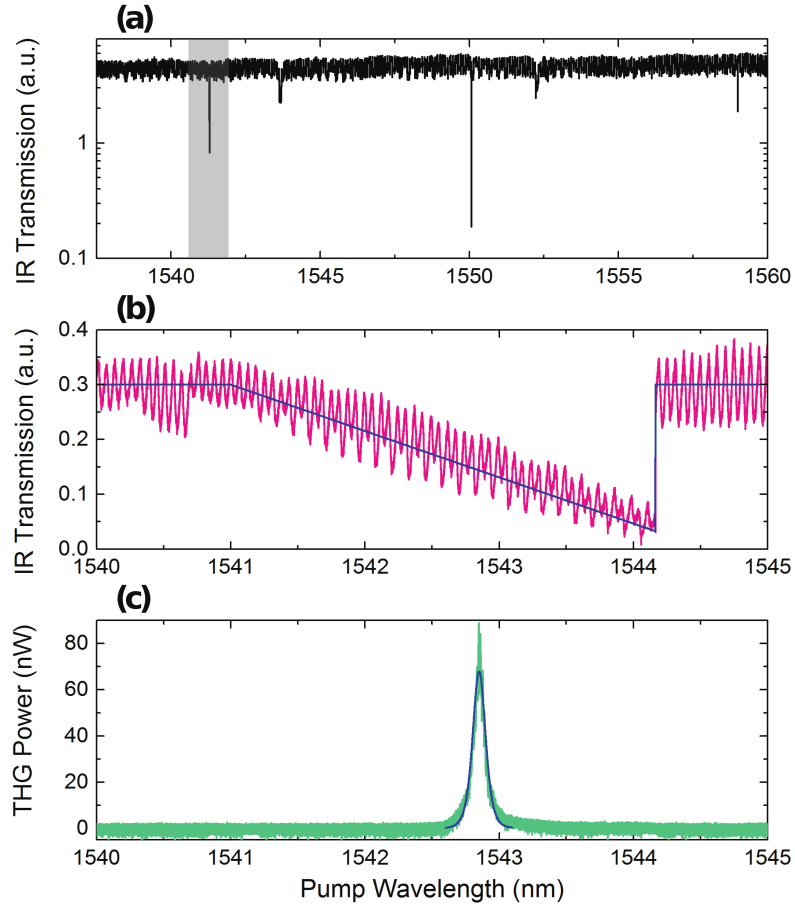


**Figure 3.6:** (a) Transmission at low input pump power. The resonance within the shaded region was used for generating TH light. (b) Transmission at high power of the IR pump resonance. Red curve and blue curve denote the experimentally observed and the simulated resonance respectively. The triangular shape resonance is a result of the thermal shifting of the 1541.2 nm resonance at high temperatures. The large shift is due to high confinement of thermal energy within the waveguide. (c) The TH response with respect to the pump wavelength. The response (green) is modeled by a lorentzian shaped curve (blue).

The experimental setup of the measurement is displayed in Fig. 3.3, consisting of two wavelength demultiplexers (WDM) at both the input and output ends of the optimized device. A pump laser source and an erbium-doped fiber amplifier was used as the input light to the device. Separate detectors were used for the IR transmission and the extracted TH signal. Two detectors at the input and output end were used for the TH signal detection,

where due to the geometry of the wrap-around waveguide coupler,  $\approx 5\%$  of the output TH light was scattered towards the output end while the remainder was collected through the input port on the left of the schematic. Finally, scattered light from the microring is collected by an Andor 193i spectrograph which has installed an iVac camera. The Andor spectrograph has a calibrated resolution of 0.15 nm. The calibration of efficiency does not include the measured signal from the spectrograph.

On Fig. 3.4 is a photograph of the microring in resonance with scattered TH light. A colormap indicating the relative intensity of the scattered TH from the top of the microring is displayed in Fig. 3.5. The collection was achieved by placing a lens directly atop the the working device. A slit size of  $50\ \mu\text{m}$  and an integrating time of one second was used as the setting of the spectrograph. The plotted colormap is plotted with the TH wavelength as the x-axis and the pump wavelength as the y-axis. The observed scattered light shows a strong peak at 514 nm, with no light observed at 771 nm, which is expected if the nonlinear process had been governed by a cascaded second order process (SHG followed by SFG) instead of the  $\chi^{(3)}$  process of THG.

The microring device characterization was performed by scanning the pump laser over the phase-matched resonance at an input power of 230 mW while observing the TH light at the photodetectors. The transmission spectrums at low power and at 230 mW (corresponding to an on-chip pump power of 60 mW), as well as the output spectrum of the THG at 230 mW input power is plotted in Fig. 3.6(a-c). Due to the thermal bistability, which can be seen in the steady state solution of Eq. 3.11, 3.12, a thermal triangle is observed in the transmission spectrum under high input power. Qualitatively, as the pump wavelength approaches resonance, the amplified intracavity power causes a thermal expansion of the ring resonator and consequently a change in the effective index of the microring. The solid blue curve of Fig. 3.6(b) corresponds to a theoretical fitting of the thermal thermal triangle, which agrees well with the measurement in red.

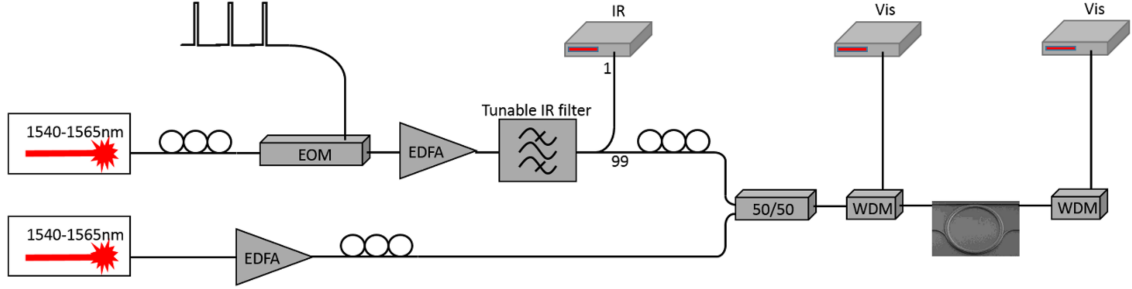


**Figure 3.7:** Schematic of the pulsed laser setup. Two separate IR inputs were used, one is connected to a commercial electro-optic modulator (EOM) with a low duty-cycle input control signal from an arbitrary waveform generator, used to probe the TH resonance. The EOM generates a pulsed signal which is then amplified by an EDFA and filtered by an opto-optics tunable filter. Fiber polarization controllers were placed on both sides of the EDFA in order to ensure TE mode operation. The auxiliary CW laser for temperature control was tuned into a resonance multiple FSRs away from the probe resonance to ensure phase-mismatch with the probe mode. Finally, IR detectors were used to monitor the pulsed laser average power as well as the visible TH signal from the microring.

Additionally, the temperature change induced by the high power pump will cause different shifts for different wavelengths due to the thermal-optical change of the refractive index (i.e.  $\Delta n \propto T$ ). Moreover, the change can be approximated by  $\Delta\omega/\omega \approx -\Delta n$ . Therefore, the frequency mismatch of the fundamental and TH modes will be changed depending on the temperature of the microring. Here, we wish to have the difference, i.e.  $3\omega_p - \omega_a(T)$  to be  $\approx 0$ . As shown in Fig. 3.6(c), the frequency mismatch is 0 at the wavelength corresponding to the maximum observed THG. At the optimized wavelength, the absorbed power is 30 mW. From our experimental observations, it was possible to fit the thermal shift coefficients by the equations:  $\lambda_a(T) = \lambda_{a0} + d_a T$ ,  $\lambda_b(T) = \lambda_{b0} + d_b T$ , with the corresponding coefficients of  $d_a = 0.016 \pm 0.001$  nm/K,  $d_b = 0.0046 \pm 0.0003$  nm/K. The efficiency is strongly dependent on the doubly resonant condition (no frequency mismatch of  $3\omega_p - \omega_a(T)$ ). Thus as the pump wavelength is further increased, the phase-matching is no longer fulfilled and the TH output is not observed.

After the inclusion of the thermal effects, the theoretical expression of the power output

due to THG becomes,

$$P_{THG} \approx \frac{2g^2 \kappa_{b,1} \left( \frac{2\kappa_{a,1}}{\kappa_a^2} \right)^3 \frac{\hbar\omega_b}{(\hbar\omega_p)^3} (P_p)^3}{\left[ \frac{2\pi c}{\lambda_a \lambda_b} ((\lambda_{a0} - 3\lambda_{b0}) + (d_a - 3d_b)T) \right]^2 + \kappa_b^2}, \quad (3.13)$$

where the efficiency is

$$\eta = \frac{P_{THG}}{P_p^3} \approx \frac{\hbar\omega_b}{(\hbar\omega_p)^3} \frac{16g^2 \kappa_{b,1} \kappa_{a,1}^3}{\kappa_a^6 \left[ \frac{2\pi c}{\lambda_a \lambda_b} (d_a - 3d_b)T \right]^2 + \kappa_b^2}. \quad (3.14)$$

Here we notice that although  $P_{THG}$  has a cubic dependence on pump power, Fig. 3.8(a) shows a non-cubic curve. The non-cubic dependence is due to the thermal effect which causes varying wavelength mismatch between the fundamental and TH mode frequencies as the pump power changes. By optimizing the temperature, a maximum of 49  $\mu\text{W}$  was observed at 30 mW absorbed power, corresponding to an on-chip THG efficiency of  $\eta = P_{THG}/(P_p)^3 = 180\% \text{W}^{-2}$  and an absolute conversion efficiency of 0.16%. Which, to the best of our knowledge, remains the highest THG efficiency achieved on an integrated platform.

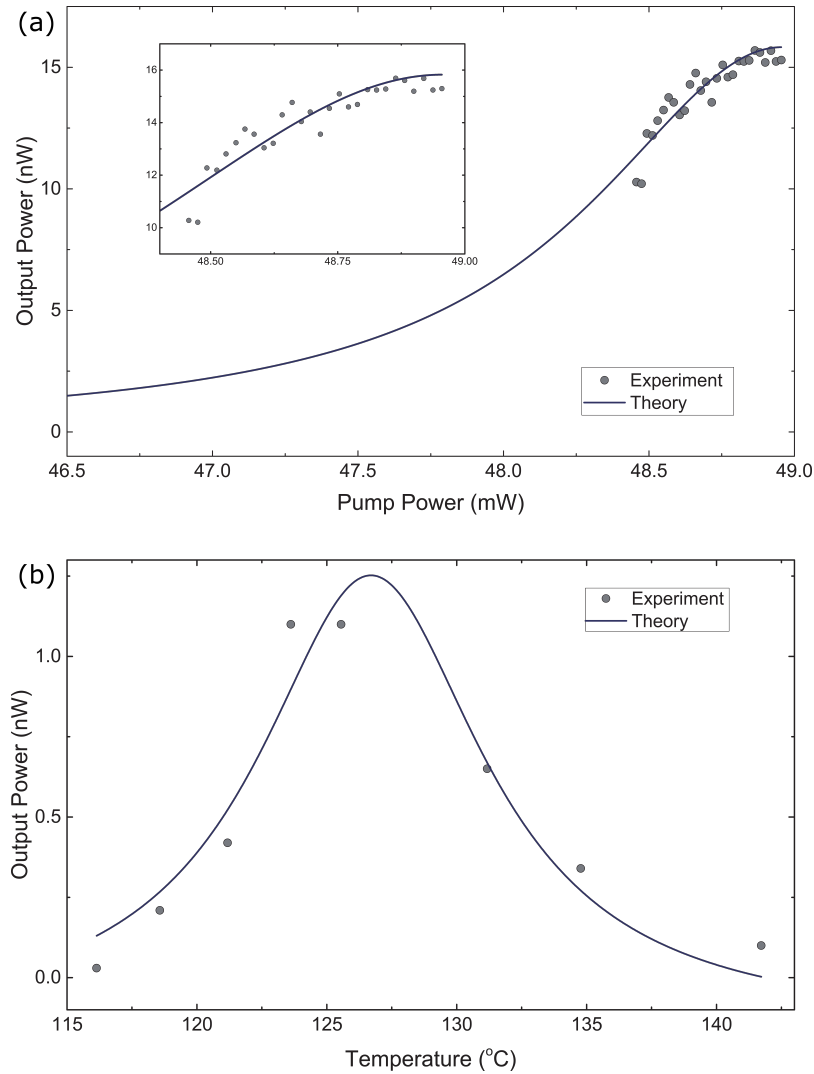


**Figure 3.8:** (a) Study of the THG power dependence using a continuous-wave (CW) laser input. The horizontal axis shows the amount of pump power that is coupled into the resonance at the phase-matched wavelength. The solid curve indicates the model prediction of the output power at high input powers, where a difference in resonance shift speeds causes resonance wavelength mismatch and subsequently a deviation from a cubic power dependence. (b) Temperature dependence of the THG. The temperature was tuned by coupling a (CW) input into a resonance away from the wavelength at which THG occurs. The absolute temperature was then calibrated for by measuring the thermal shift in the IR resonances. Simultaneously, a low-duty cycle modulated laser with a average power of 4 mW was used for THG. This scheme was implemented to avoid the thermal shift at high CW input powers. A lorentzian shaped temperature dependence curve with a full-width-at-half-maximum (FWHM) of  $10.6^{\circ}\text{C}$  is fitted.

The characterisation of the visible resonant mode at 514 nm is a challenging task. In

order to probe the mode without subject to thermal nonlinearities and to be able to interrogate fundamental aspects of the mode such as the Q factor, a pulsed input laser and an auxiliary continuous-wave (CW) laser are used simultaneously as shown in Fig. 3.7. The auxiliary laser serves as a temperature control by tuning a high power CW input into an IR resonance. The pulse laser is then tuned to a phase-matched wavelength to observe the output of the THG without thermal shift, since the pulse laser operates at a very low duty cycle and thus the average power is low. Finally we observe the maximum THG signal at varying auxiliary laser detunings as shown in Fig. 3.8(b), which is accurately fitted by the lorentzian lineshape solid curve as predicted by 3.14. The full-width at half maximum (FWHM) is determined by the equation:  $\Delta T = \frac{\kappa_b \lambda_a \lambda_b}{\pi c (d_a - 3d_b)} = \frac{\lambda_a}{Q_b d_\Delta}$ . Where  $d_\Delta = (d_a - 3d_b)$ . From the empirical results, a  $\Delta T = 10.6^\circ\text{C}$  was observed. Thus, according to the previously measured value of  $\lambda_a$  and  $d_\Delta$ , we estimate the loaded Q factor of the TH mode to be  $Q_b \approx 6.4 \times 10^4$ .

### 3.6 Future Work and Conclusions

In conclusion, THG was optimized on a composite AlN/Si<sub>3</sub>N<sub>4</sub> integrated platform through a systematic study of the field overlap between the input and TH modes, coupling of IR and visible modes, as well as detailed thermo-optic analysis. From our experimental results, we report a calibrated on-chip efficiency of  $\eta = P_{\text{THG}}/(P_p)^3 = 180\% \text{ W}^{-2}$ . To the best of our knowledge, this is the highest reported THG efficiency achieved on an integrated platform. Additionally, a power dependent and temperature dependent measurement was used to confirm our theoretical understanding of the THG. We note that future improvements can be made to our system to achieve higher efficiency THG, including further optimization of the IR and visible quality factor, the thickness of the bilayer as well as the gap between the microring and the visible coupling waveguide.

## References

- [1] D. J. Moss, R. Morandotti, A. L. Gaeta, and M. Lipson, “New CMOS-compatible platforms based on silicon nitride and hydrex for nonlinear optics,” *Nat. Photonics* **7**, 597 (2013).
- [2] B. Shen, L. Chang, J. Liu, H. Wang, Q.-F. Yang, C. Xiang, R. N. Wang, J. He, T. Liu, W. Xie, J. Guo, D. Kinghorn, L. Wu, Q.-X. Ji, T. J. Kippenberg, K. Vahala, and J. E. Bowers, “Integrated turnkey soliton microcombs,” *Nature* **582**, 365 (2020).
- [3] M. H. P. Pfeiffer, C. Herkommer, J. Liu, T. Morais, M. Zervas, M. Geiselmann, and T. J. Kippenberg, “Photonic damascene process for low-loss, high-confinement silicon nitride waveguides,” *IEEE Journal of Selected Topics in Quantum Electronics* **24**, 1 (2018).
- [4] M. H. P. Pfeiffer, J. Liu, A. S. Raja, T. Morais, B. Ghadiani, and T. J. Kippenberg, “Ultra-smooth silicon nitride waveguides based on the damascene reflow process: fabrication and loss origins,” *Optica* **5**, 884 (2018).
- [5] J. S. Levy, M. A. Foster, A. L. Gaeta, and M. Lipson, “Harmonic generation in silicon nitride ring resonators,” *Opt. Express* **19**, 11415 (2011).
- [6] M. Cazzanelli, F. Bianco, E. Borga, G. Pucker, M. Ghulinyan, E. Degoli, E. Luppi, V. Véniard, S. Ossicini, D. Modotto, S. Wabnitz, R. Pierobon, and L. Pavesi, “Second-harmonic generation in silicon waveguides strained by silicon nitride,” *Nat. Mater.* **11**, 148 (2011).
- [7] X. Lu, G. Moille, A. Rao, D. A. Westly, and K. Srinivasan, “Efficient photoinduced second-harmonic generation in silicon nitride photonics,” *Nat. Photonics* **15**, 131 (2021).
- [8] E. Timurdogan, C. V. Poulton, M. J. Byrd, and M. R. Watts, “Electric field-induced second-order nonlinear optical effects in silicon waveguides,” *Nat. Photonics* **11**, 200 (2017).



# Chapter 4

## Stable Tuning of Resonant Modes in Lithium Niobate Microrings

Lithium niobate (LN) has been an important material for nonlinear optics in the past few decades. It is heavily used for second order nonlinear processes due to its large  $\chi^{(2)}$  nonlinear tensor, as well as for fast switching based on its electro-optics properties. Domain engineering has also enabled quasi-phase-matching (QPM) on lithium niobate which has led to many more customizable photonics applications.

### 4.1 Motivation

The recent emergence of lithium niobate (LN) as a candidate for integrated nonlinear optics was led by the advancement of fabrication methods that allow for high quality, crystalline waveguides to be realized on the LN platform. In conjunction with low mode volume microresonators, it is now possible to realize a variety of nonlinear integrated photonics devices on LN. This is a significant achievement due to the substantially large second order nonlinearity of LN, and the simultaneous presence of third order nonlinearity in the material. This can allow nonlinear phenomena to be achieved at record low

powers<sup>1-6</sup>, and even for the unveiling of new physics<sup>7</sup>.

Particularly in the application of achieving stabilized solitons, lithium niobate can offer a similar advantage to AlN in that it contains both Kerr and Pockels nonlinearity. Furthermore, current fabrication methods allow for high-Q microring resonators to be consistently realized, with Q factors of over 10 million having been achieved recently<sup>4</sup>. There are two main drawbacks of the lithium niobate platform. First is the relative difficulty of etching of the material, and second is that the material is highly susceptible to photorefractive (PR) damage. Crystalline LN material is notoriously difficult to etch, however, current fabrication methods that utilize ion milling can still achieve high quality factor, albeit with lower selection ratio against typical lithography masks. The primary difficulty of using LN on an integrated resonator-based photonics platform is the photorefractive effect, which causes instability even under modest input powers. Bulk LN is known to possess many trap states. Furthermore, for every input photon, there is an increased likelihood in a corresponding ionization of a trap donor due to the substantially high optical confinement of photonic waveguides and optical cavities. Driven by LN's intrinsically large EO tensor coefficients, the amplified intracavity photons leads to a substantial resonance shift even at low input powers. The following sections will discuss the effect in more details and present a method of stabilizing cavity modes in LN-based microresonators using an auxiliary laser.

The work of Lu et. al.<sup>6</sup> presented a novel platform of a periodically-poled LN (PPLN) microring resonator, an achievement with great potential in terms of integrated nonlinear optics. PPLN has long been used as the material of choice in many commercial applications due to its high efficiency for  $\chi^{(2)}$  frequency conversion processes as well as easily manipulable phase-matching conditions that allows for operation at many different wavelengths of interest. Poling on a microring resonator allows further enhancement of these nonlinear processes and is of immense interest in the scientific community. However, the drawbacks of the material platform primarily in PR damage remains and it is important to be able to mitigate or have fine control over this effect.

## 4.2 Photorefractive and Thermal Nonlinear Effects in Lithium Niobate Microrings

The photorefractive effect is a change in the refractive index, caused by the redistribution of charges when electrons in the trapped states of the material are excited by incident light. The redistribution of charges causes a change in the refractive index due to the electro-optic effect. In a first order approximation, this effect within a microresonator can be thought of as a similar one to the thermal nonlinear effect, with a negative coefficient compared to that of the temperature coefficient. Therefore, in contrast to the thermal effect, where under steady-state in a purely thermal system, bistability exists in the red-detuned region, in a purely photorefractive microresonator under steady state there are bistable solutions in the blue-detuned region. This counteracting change in refractive index is represented by  $\Delta n = -\frac{n_{\text{eff}}^3}{2} r_{\text{eff}} E_{\text{sc}}$ . Where  $n_{\text{eff}}$  is the effective index of the resonator and  $r_{\text{eff}}$  is the effective EO coefficient.

Furthermore, whereas the thermal effect in a microresonator usually exhibits one relaxation times on the order of micro-seconds, the PR effect can have multiple relaxation times on the order of milliseconds or even seconds, and is dependent on the electronic band structure. The relaxation time is also temperature dependent, where a higher temperature causes quicker space charge redistribution back to an equilibrium state.

To broadly understand the underlying mechanisms, LN is a material with many trap states between the valence and conduction band. The Nb defects act as electron trap sites and form polaron and bipolaron states which are responsible for the photorefractive damage<sup>8</sup>. The trap states lie close to the valence band such that light below the band-gap can easily excite electrons into the trap. If the traps are located close to one another, there is a non-zero probability that the electrons will jump from one trap to the other, causing the redistribution of charges that results in a “space charge” in the vicinity of where the trap

electrons are generated by light interaction with the lithium niobate cavity. The potential well of a trap can be described by that of a harmonic oscillator. When an electron is excited to a trap state, this potential well is altered to become one with two dips. At non-zero temperatures, it is possible for a trapped electron to escape by an activation energy of  $E_A$ , where the equation dictating the time constant of electrons from trapped state to the valence band is of an Arrhenius-type dependence  $\tau_e = 1/\gamma_e \sim Ke^{-\frac{E_A}{k_B T}}$ <sup>9</sup>.

The mitigation of the PR effect can be approached in a variety of ways<sup>10</sup>, including reducing the number of trap states and operation at a higher temperature to lower the relaxation time. Another method to lower the relaxation time is by utilizing an auxiliary laser (effectively, this is a saturation of the charge carrier generation rate), which will be described in the following section.

## 4.3 Theoretical Description of $\chi^{(2)}$ Nonlinear Frequency Conversion in a Lithium Niobate Microring

### 4.3.1 Saturation of the Photorefractive Effect

In previous studies, the coupled equations of motions for a single mode cavity have generally been written as

$$\begin{aligned} \frac{da}{dt} &= (i\delta_a - \kappa_a)a - ig_T \Delta T a - ig_E E_{sc} a + \varepsilon_a \\ \frac{d(\Delta T)}{dt} &= -\gamma_{th} \Delta T + K_{th} |a|^2 \\ \frac{dE_{sc}}{dt} &= -\gamma_e E_{sc} + K_e |a|^2, \end{aligned} \quad (4.1)$$

where  $g_E$  and  $g_T$  are respectively the electrooptic and thermooptic coupling rate coefficients.  $E_{sc}$  and  $\Delta T$  denote the space-charge electric field and variation in environment temperature due to the total intracavity photons. The intrinsic generation coefficients of

space-charge field and heat are given by  $K_e$  and  $K_{th}$ , while the decay rates are denoted by  $\gamma_{e,th}$ . This description for a system under low input power is a sufficient first order estimation of the thermal and photorefractive nonlinearities of the system. However, as noted by the work cited above as well as in the previous section, there is a power dependence of the relaxation times not captured by 4.1. A more accurate description of a LN microresonator system operating at higher input powers will require an expression that captures the total number trap states, where the probability of a photon exciting an electron to a trap state diminishes as the number of free traps approaches zero. This more detailed representation of the system is an adaptation of the band transport model<sup>11</sup>, where the probability of trap ionization under illumination based on available carriers is taken into consideration. Consequently, the rate equations of  $E_{sc}$  and  $\Delta T$  can be expressed as

$$\frac{dE_{sc}}{dt} = \begin{cases} -\gamma_e E_{sc} + K_e \left(1 - \frac{N_{tot}}{N_{eff}}\right) N_{tot} & N_{tot} \leq \frac{N_{eff}}{2} \\ -\gamma_e E_{sc} + \frac{K_e N_{eff}}{4} & N_{tot} > \frac{N_{eff}}{2} \end{cases} \quad (4.2a)$$

$$\frac{d(\Delta T)}{dt} = -\gamma_{th} \Delta T + K_{th} N_{tot}. \quad (4.2b)$$

Here,  $N_{tot}$  represents the total intracavity photon number and the expression  $K_e \left(1 - \frac{N_{tot}}{N_{eff}}\right)$  can be thought of as a mapping of photons to space-charge carrier generation rate, which captures the description of the decreasing probability of charge carrier generation with increasing donor ionization at higher input powers.  $N_{eff}$  denotes the total number of trap states available for ionization. As more of the available electrons are excited into trap states, eventually  $\frac{dE_{sc}}{dt}$  reaches zero, when the maximum generation rate of  $\frac{K_e N_{eff}}{4}$  at  $N_{tot} > \frac{N_{eff}}{2}$  is balanced by the term dictating the decay rate of  $-\gamma_e E_{sc}$ . At this point,  $E_{sc}$  is saturated at a maximum value.

### 4.3.2 Modeling of Second Harmonic Generation With an Auxiliary Laser

In this section, the analysis of SHG in the LN microresonator system with the presence of an auxiliary laser is presented. The Hamiltonian of the system is given by

$$\begin{aligned}
 H = & \delta_a a^\dagger a + \delta_b b^\dagger b + \delta_c c^\dagger c + g \left( a^2 b^\dagger + (a^\dagger)^2 b \right) \\
 & + i\varepsilon_a \left( -a + a^\dagger \right) + i\varepsilon_c \left( -c + c^\dagger \right),
 \end{aligned} \tag{4.3}$$

where  $a$ ,  $b$ , and  $c$  represent the pump, SH, and auxiliary modes respectively, these quantities are normalized such that  $|a|^2$ ,  $|b|^2$ , and  $|c|^2$  denote the number of photons in the modes.  $\delta_{a(c)} = \omega_{a(c)} - \omega_{fa(c)}$ ,  $\delta_b = \omega_b - 2\omega_a$  are the pump laser detunings from the pump telecom (auxiliary drive) cavity mode and the SH cavity mode, while  $g$  is the nonlinear coupling rate of the SH process, as derived in previous sections. The pump (auxiliary drive) term is represented by  $\varepsilon_{a(c)} = \sqrt{2\kappa_{a(c),1} \frac{P_{a(c)}}{\hbar\omega_{fa(c)}}$ . In our work, the auxiliary drive mode was selected to be TE in order avoid phase-matching with any  $\chi^{(2)}$  processes that could potentially interfere with SHG. Its primary use is for PR effect saturation.

Under the Heisenberg representation of the modes, the coupled equations of motions are,

$$\begin{aligned}
 \frac{d}{dt}a &= - (i\delta_a + \kappa_a) a - i(g_E E_{sc} + g_T \Delta T) a - i2ga^\dagger b + \varepsilon_a \\
 \frac{d}{dt}b &= - (i\delta_b + \kappa_b) b - i(g_E E_{sc} + g_T \Delta T) b - iga^2 \\
 \frac{d}{dt}c &= - (i\delta_c + \kappa_c) c - i(g_E E_{sc} + g_T \Delta T) c + \varepsilon_c.
 \end{aligned} \tag{4.4}$$

along with 4.2 from the previous subsection. Where we note that  $c$  mode of the auxiliary laser is not coupled with the  $b$  mode and therefore can be separately solved for at every time-step of the numerical modeling. A few additional assumptions were made in order to simplify the analysis and numerical modeling. First, the intrinsic generation rates and response times of heat, charge carriers and intracavity photons were treated as small

compared to the time-scale of the PR effect (i.e.  $\frac{d}{dt}a = \frac{d}{dt}b = \frac{d}{dt}c = \frac{d(\Delta T)}{dt} = 0$ ). Second, when  $N_{tot} > \frac{N_{eff}}{2}$ , the space-charge field generation rate was maximized such that  $K_e \left(1 - \frac{N_{tot}}{N_{eff}}\right) N_{tot} = \frac{K_e N_{eff}}{4}$ . Third, the distribution of probabilities for every photon's generation of a charge carrier is uniform, and therefore has an equal probability in ionizing a trap donor (location can concentration of photons within the microring does not affect generation rate). Fourth, visible SH photons were assigned twice the probability of charge carrier excitation. Lastly, for the sake of simplicity, our model only considered one PR response time most relevant to empirical observations.

Carrying out a similar analysis as 2.2, and taking into account the thermal and PR contributions, we arrive at the following coupled equations

$$\begin{aligned}
\frac{da}{dt} &= 0 = X_a a - K_{T,a} (N_{tot,t-dt}) a - g_{E,a} E_{sc} a - i2ga^*b + \epsilon_a \\
\frac{dc}{dt} &= 0 = X_c c - K_{T,c} (N_{tot,t-dt}) c - g_{E,c} E_{sc} c + \epsilon_c \\
b &= \frac{iga^2}{X_b - K_{T,b} (N_{tot,t-dt}) - g_{E,b} E_{sc}} = \frac{iga^2}{X_{b,t-dt}} \\
\frac{dE_{sc}}{dt} &= \begin{cases} -\gamma_e E_{sc} + K_e \left(1 - \frac{N_{tot,t-dt}}{N_{eff}}\right) N_{tot,t-dt} & N_{tot,t-dt} \leq \frac{N_{eff}}{2} \\ -\gamma_e E_{sc} + \frac{K_e N_{tot,t-dt}}{4} & N_{tot,t-dt} > \frac{N_{eff}}{2}, \end{cases}
\end{aligned} \tag{4.5}$$

noting once again that the response times of photon generation and thermal relaxation is much smaller compared to that of charge carrier generation. Here,  $K_{T,a} = ig_T \frac{K_{th}}{\gamma_{th}}$  is the thermal coefficient at steady state,  $N_{tot,t-dt} = |a|^2 + 2|b|_{t-dt}^2 + |c|^2$  is the total intracavity photon number, where the numerical modeling makes use of the SH  $b$  mode at the previous time-step as an approximation of the number of SH photons in the cavity. The pump and auxiliary modes photon number  $|a|^2$  and  $|c|^2$  can be further expressed as a polynomial.

Here we only present the polynomial for  $|a|^2$ , which is

$$\begin{aligned}
0 = & \left( |a|^2 \right)^3 \left( \frac{4g^4}{|X_{b,t-dt}|^2} + |K_{T,a}|^2 - 4g^2 \operatorname{Re} \left\{ \frac{K_{T,a}^*}{X_{b,t-dt}} \right\} \right) \\
& + \left( |a|^2 \right)^2 \left( -2\operatorname{Re} \{ K_{T,a}^* X_a \} + 2\operatorname{Re} \{ g_{E,a} E_{sp} K_{T,a}^* \} + 4g^2 \operatorname{Re} \left\{ \frac{X_a}{X_{b,t-dt}^*} \right\} - 4g^2 \operatorname{Re} \left\{ \frac{g_{E,a}^* E_{sp}^*}{X_{b,t-dt}} \right\} \right) \\
& + |a|^2 \left( |X_a|^2 - 2\operatorname{Re} \{ g_{E,a} E_{sp} X_a^* \} + |g_{E,a}|^2 |E_{sc}|^2 \right) - |\varepsilon_a|^2
\end{aligned} \tag{4.6}$$

where the solution to this polynomial can be solved for at every time-step in the dynamical variation of space-charge electric field  $E_{sc}$ .

Subsequently we can arrive at the output power of mode  $a$  at the waveguide, as well as the transmission of mode  $a$ ,

$$\begin{aligned}
P_{a,out} &= |a_{out}|^2 \hbar \omega_a \\
a_{out} &= \frac{\varepsilon_a}{\sqrt{2\kappa_{a,1}}} - \sqrt{2\kappa_{a,1}} \frac{-\varepsilon_a}{(X_a - K_{T,a} N_{tot,t-dt} - g_{E,a} E_{sc}) + \frac{2g^2 |a|^2}{X_{b,t-dt}}}
\end{aligned} \tag{4.7}$$

$$T = \left| 1 + \frac{2\kappa_{a,1}}{X_a' + \frac{2g^2 |a|^2}{X_{b,t-dt}}} \right|^2, \tag{4.8}$$

which is frequently the quantity that is observed in experiments. Here we have aggregated the terms related to loss and frequency shift into  $X_a' = X_a - K_{T,a} N_{tot,t-dt} - g_{E,a} E_{sc}$ .

It is clear from the equations above that for the purpose of minimizing the PR induced wavelength shift, at  $\frac{dE_{sc}}{dt} = 0$  and  $N_{tot,t-dt} \geq \frac{N_{eff}}{2}$ , additional input cavity photons will not cause a shift in the wavelength. The system at this state has achieved maximum charge-carrier generation rate and is balanced by the relaxation rate to achieve constant static field. This dependence of  $E_{sc}$  on the available charge carriers also explains the previously observed power dependence of the PR effect<sup>12</sup>. However for practical purposes, it is often hard to fully stabilize the cavity using an auxiliary laser with a frequency close to that of



the fundamental due to additional charge-carriers generated more efficiently by SH mode frequencies. Moreover, many applications often have stringent power requirements, thus it is more important to ask: at what point will additional cavity photons produce a sufficiently small resonance shift for the application? The equation of interest then is

$$g_{E,a}\Delta E_{sc} < \Delta\omega. \quad (4.9)$$

From here, the appropriate input power for the auxiliary laser can be reverse engineered.

## 4.4 Results and Discussion

In this section, results of SHG due to both quasi-phase-matching and modal phase-matching are both presented. The experimental fine control of resonance modes, particularly the SHG peak output wavelength in a PPLN microring using an auxiliary laser is further discussed. The details of fabrication procedure and the design of phase-matching can be found in<sup>2,6</sup>. The specific device under test has a ring radius of  $70\mu\text{m}$  and a ring width of  $1.8\mu\text{m}$ . The thickness of the LN material was  $600\text{nm}$ , and was shallow etched with a step height of  $180\text{nm}$ . A poling period of  $3\mu\text{m}$  was used to realize the phase-matching between the fundamental and SH mode. Finally, we note the type-I phase-matching used for SHG, where the  $d_{33}$  term of the second order nonlinear susceptibility tensor component coupling the TM fundamental mode to the TM SH mode was used.

### 4.4.1 Auxiliary Laser Stabilization of LN Microring Resonant Modes

Figure 4.1(a) displays a schematic of the stabilization of the SHG process. Two lasers corresponding to a low power pump laser for SHG and a high power auxiliary laser for charge-carrier saturation were used. The auxiliary laser was first hand-tuned into the cavity

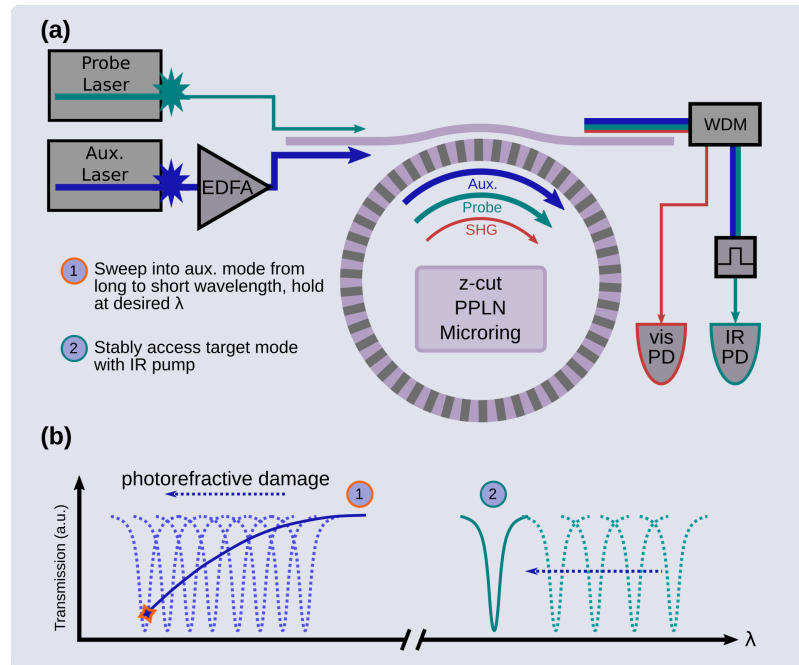


**Figure 4.1:** (a) Schematic of the experimental setup. Two laser inputs, a pump probe and an auxiliary drive were used for interrogating two separate cavity modes (the pump mode  $a$  and auxiliary mode  $c$ ). A higher power for the auxiliary laser input is used. (b) Conceptual diagram of the operation principle. The photorefractive effect causes unstable and difficult resonance locking. The proposed solution first utilizes an auxiliary laser, by slowly tune it into resonance at high power, where stable tuning is possible due to the stable dynamics of thermal expansion and photorefraction. With the auxiliary laser in resonance, the target mode can be stably accessed at low powers.

resonance at an input power of 5.4mW, after which a stable interrogation of the mode with high SHG efficiency was achieved using an input power of 98.6  $\mu$ W. Here, the word stable refers to: (1) the freedom to scan over the SH resonance repeatedly and realize the same output SH power and resonance shape, as well as (2) the ability to hold the probe input laser at the resonance wavelength with little to no fluctuations (limited by the stability of the input laser and environment temperature). Conceptually, as Fig 4.1(a) shows and based on the previous section's explanations, while the auxiliary laser is first used to access stable steady states of the resonant system at higher powers, the target mode instabilities due to competing thermal and photorefractive processes can be circumvented.

The dynamics governing the LN microring system was modeled by solving for the coupled system of equations in 4.5, where a comparison of the empirical and simulation results are depicted in Fig. 4.2. Here the fitted model parameters were  $\gamma_e = 0.25$  Hz,  $K_e = 180$  V/(m  $\cdot$  s),  $g_{E,a(c)} = 2.1 \times 10^4$  m/(V  $\cdot$  s),  $g_{E,b} = 8.5 \times 10^4$  m/(V  $\cdot$  s),  $\gamma_{th} = 230$  kHz,  $K_{th,(a,b,c)} = 0.026$  K/s, and  $g_T = 1.68$  (K  $\cdot$  s) $^{-1}$ . For the effective total trap states approximation, a value of  $N_{\text{eff}} \approx 6 \times 10^8$  provided a good fit to our observations and approximately corresponds to a donor concentration of  $N_d \approx 5 \times 10^{17}$  cm $^{-3}$ .<sup>9</sup> All parameters in the numerical simulations were in good agreement with previous LN microring studies<sup>9,12,13</sup>.

The resonant TM fundamental IR mode had a Q factor measured at  $Q_l = 1.88 \times 10^5$ . The characterization and simulation of Fig. 4.2(a-b) was performed without the presence of an auxiliary laser, where the solid lines (black triangles) represent the experimental observations and the dotted lines (colored circles) are the simulation results. The instability of the SH output and the corresponding fundamental mode was observed through the variation of the SH peaks as well as the closing of the separation of the double peaks in a single scan. The latter was observed due to differing frequency shifts and the small mode mismatch between the telecom and SH modes. Here, the characterization was performed by implementing ten scans at a scan speed of 0.5 nm/sec and at intervals of 10 seconds apart. The shifts in resonance wavelengths were due to increasing  $E_{sc}$  at each subsequent

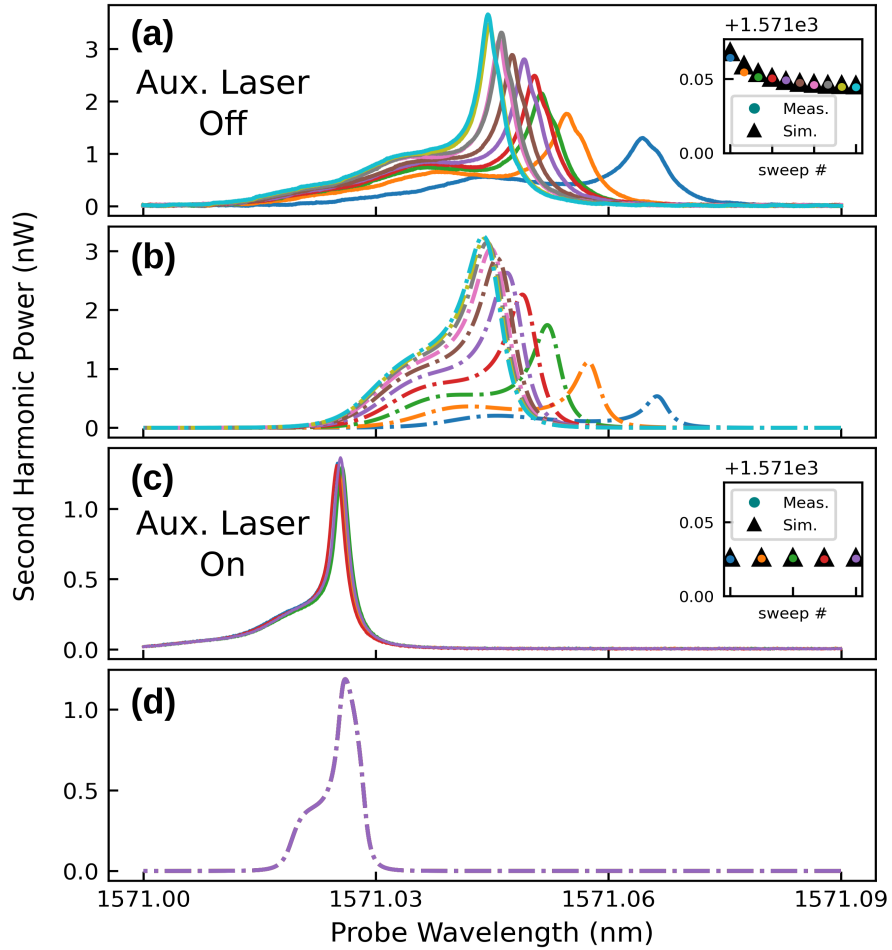


**Figure 4.2:** Experimental and simulated SH output plots with the auxiliary laser off and on resonance. (a) SH output traces measured at intervals of 10 seconds, with the auxiliary laser set to be far-detuned from the resonance. The on-chip auxiliary and probe laser powers were set to 5.4 mW and 98.6  $\mu$ W respectively. The inset depicts the shifting peak of the SHG with number of laser scans, where the measured and simulated data are denoted by circles and triangles. (b) The simulated SH output of the measurement without an auxiliary laser. The cold cavity resonance wavelengths for IR and SH modes are fitted to be approximately 1571.05 nm and 785.535 nm respectively, this slight energy mismatch causes the double peaks observed in the SHG spectrum. (c) SH output traces when the auxiliary laser is locked into one resonance, at intervals of 10 seconds. The auxiliary laser suppresses the PR-induced resonance shifts, allowing stable cavity access. The inset depicts the stabilized peak of the SHG with number of laser scans. (d) Simulated output traces of SHG with the auxiliary laser in resonance.

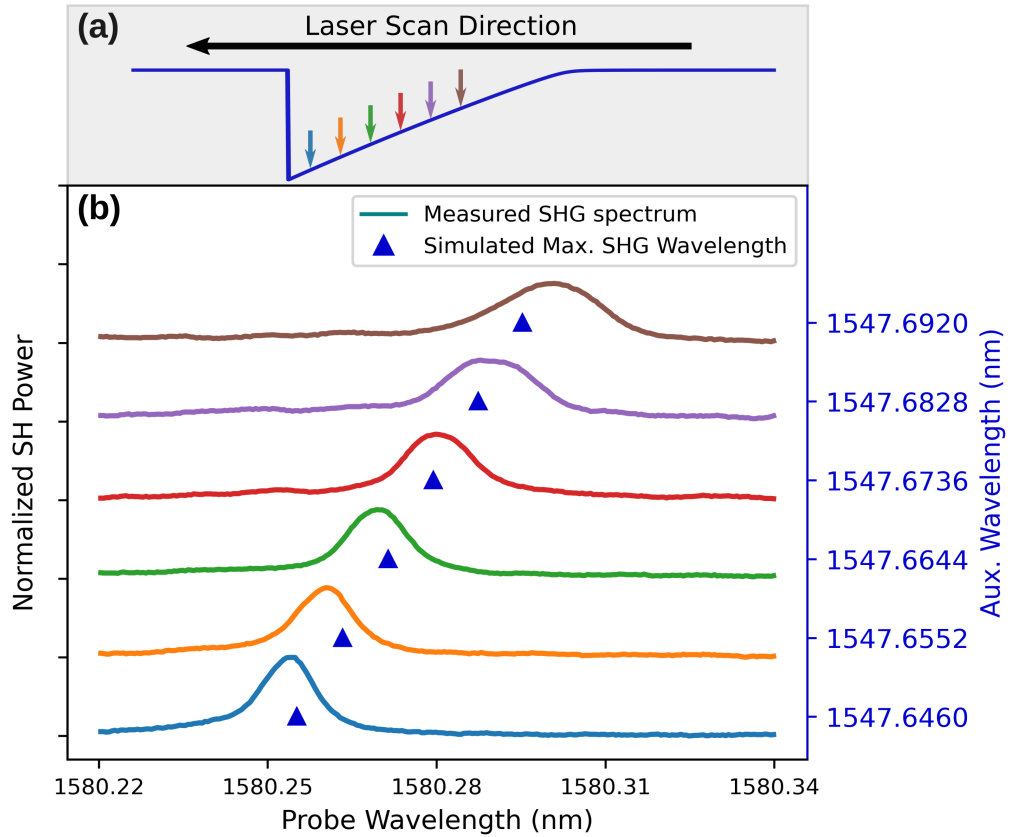


**Figure 4.3:** Tuning of SHG peak wavelength using an auxiliary laser and the photorefractive effect. (a) Illustration of the transmission curve of the auxiliary mode resonance with red-to-blue scan. Each arrow independently signifies a different auxiliary laser wavelength used when measuring the SHG output. The color of the arrow corresponds to the trace in (b). (b) Normalized SHG output at various Auxiliary laser wavelengths (5 mW auxiliary laser power on-chip). The simulated SHG peak wavelength is plotted against the traces (98.6  $\mu$ W on-chip probe power).

scanning of the laser from a build-up of charge-carriers.

In contrast, with the auxiliary laser hand tuned slowly into a TE resonance (avoidance of unintended nonlinear interactions), repeating the experiment of repeated scans over the SH resonance resulted in reproducible SH output spectrums. Furthermore, it was possible to stably hand tune the probe laser into the peak of the SH output, which is otherwise a significant challenge. We note that the condition met here can be expressed as  $|c|^2 \gg |a|^2$ , such that the incremental resonance shift due to the input probe mode  $a$  is small, i.e.  $g_E \Delta E_{sc} \ll \kappa_a$ .

An important utilization of this auxiliary-assisted stabilization technique is for the fine-tuning of any SH resonance wavelength. In Fig. 4.3, experimental results that demonstrate stable tuning using an auxiliary laser is shown. By varying the laser drive wavelength detuning from the auxiliary mode  $c$ , stable tuning of the maximum SHG wavelength was achieved over a 50 pm bandwidth. The drive laser was set at 5mW on-chip power, whereas the probe laser input on-chip power was 98.6 $\mu$ W.

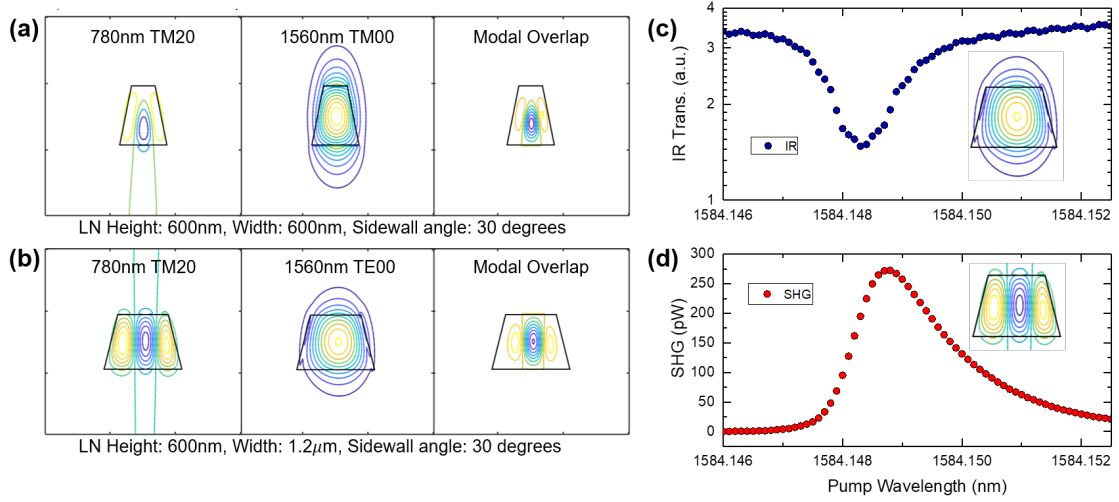


**Figure 4.4:** Simulated mode profiles relevant to phase-matching utilizing the  $d_{33}$  component of the  $\chi^{(2)}$  nonlinear coefficient, along with the mode overlap profile in the cross-section of the LN waveguide. For a film thickness of 600 nm, phase-matching occurs at 600 nm. (b) Mode profiles of the IR and visible mode at a phase-matching width of 1.2  $\mu\text{m}$ , utilizing the  $d_{31}$  coefficient. (c)-(d) Measured transmission and SHG output of a 1.2  $\mu\text{m}$  wide ring with a TE<sub>00</sub> IR input pump. The SHG spectrum corresponds to a 600 %/W efficiency.

#### 4.4.2 Modal Phase-Matched SHG on LN

Prior to the technological advances that led to the realization of high quality factor microresonators on a LN platform, the engineering of modal dispersion had been the go-to method for phase-matching the fundamental and higher order modes in nonlinear frequency conversion. This was due to many of the popular materials being non-ferroelectric, such as AlN. For LN-based microrings, the use of modal phase-matching could circumvent difficult poling processes and produce more robust and repeatable devices.

Fig. 4.4 shows the optimized simulated geometries for both SHG due to the  $d_{33}$  and  $d_{31}$  components of the second order nonlinear susceptibility tensor.

## 4.5 Future Work and Conclusions

In this section, we have presented a technique for circumventing PR related instabilities in microcavity resonance wavelengths with the assistance of an auxiliary laser. The target probe mode can be reliably and easily accessed even by hand-tuning by saturating the space-charge field. We further utilize this method in the stabilization of a SHG peak in a PPLN microring. The versatility of this scheme is further supported by the extensive numerical modeling of the triple-mode interactions in a dual-resonant, nonlinear system. The theoretical analysis takes into consideration the available trap donor states, which describes the power dependence of the space-charge field generation coefficient. Lastly, the tuning capabilities of this scheme was explored by varying auxiliary laser wavelength detunings from cavity resonance, where picometer precision was achieved. The method described in this Letter can be used in a variety of microresonator systems that suffer from PR instabilities.

## References

- [1] J. Lu, A. Al Sayem, Z. Gong, J. B. Surya, C.-L. Zou, and H. X. Tang, “Ultralow-threshold thin-film lithium niobate optical parametric oscillator,” *Optica* **8**, 539 (2021).
- [2] J. Lu, M. Li, C.-L. Zou, A. Al Sayem, and H. X. Tang, “Toward 1% single-photon anharmonicity with periodically poled lithium niobate microring resonators,” *Optica* **7**, 1654 (2020).
- [3] C. Wang, M. Zhang, X. Chen, M. Bertrand, A. Shams-Ansari, S. Chandrasekhar, P. Winzer, and M. Lončar, “Integrated lithium niobate electro-optic modulators operating at CMOS-compatible voltages,” *Nature* **562**, 101 (2018).
- [4] B. Desiatov, A. Shams-Ansari, M. Zhang, C. Wang, and M. Lončar, “Ultra-low-loss integrated visible photonics using thin-film lithium niobate,” *Optica* **6**, 380 (2019).
- [5] M. Zhang, B. Buscaino, C. Wang, A. Shams-Ansari, C. Reimer, R. Zhu, J. M. Kahn, and M. Lončar, “Broadband electro-optic frequency comb generation in a lithium niobate microring resonator,” *Nature* **568**, 373 (2019).



- [6] J. Lu, J. B. Surya, X. Liu, A. W. Bruch, Z. Gong, Y. Xu, and H. X. Tang, "Periodically poled thin-film lithium niobate microring resonators with a second-harmonic generation efficiency of 250,000%/w," *Optica* **6**, 1455 (2019).
- [7] Y. Qi and Y. Li, "Integrated lithium niobate photonics," *Nanophotonics* **9**, 1287 (2020).
- [8] R. Bhatt, I. Bhaumik, S. Ganesamoorthy, R. Bright, M. Soharab, A. Karnal, and P. Gupta, "Control of intrinsic defects in lithium niobate single crystal for optoelectronic applications," *Crystals (Basel)* **7**, 23 (2017).
- [9] A. Yariv, S. S. Orlov, and G. A. Rakuljic, "Holographic storage dynamics in lithium niobate: theory and experiment," *J. Opt. Soc. Am. B* **13**, 2513 (1996).
- [10] Y. Xu, M. Shen, J. Lu, J. B. Surya, A. A. Sayem, and H. X. Tang, "Mitigating photorefractive effect in thin-film lithium niobate microring resonators," *Opt. Express* **29**, 5497 (2021).
- [11] N. V. Kukhtarev, V. B. Markov, S. G. Odulov, M. S. Soskin, and V. L. Vinetskii, "Holographic storage in electrooptic crystals. i. steady state," *Ferroelectrics* **22**, 949 (1978).
- [12] X. Sun, H. Liang, R. Luo, W. C. Jiang, X.-C. Zhang, and Q. Lin, "Nonlinear optical oscillation dynamics in high-q lithium niobate microresonators," *Opt. Express* **25**, 13504 (2017).
- [13] H. Jiang, R. Luo, H. Liang, X. Chen, Y. Chen, and Q. Lin, "Fast response of photorefraction in lithium niobate microresonators," *Opt. Lett.* **42**, 3267 (2017).

# Chapter 5

## Integration of Soliton Microcombs and SHG on Aluminum Nitride Microrings

### 5.1 Motivation

In the past few years, interest in Aluminum Nitride as the go-to platform for frequency comb generation has soared. The advantages of the platform are numerous and have been mentioned in prior chapters. The most recent advance on integrated AlN comb generation is the development of dispersion engineered soliton combs with dual dispersive waves and high repetition rates, as well as the measurement of its carrier envelope offset frequency ( $f_{\text{ceo}}$ )<sup>1</sup>, performed on a separate AlN chip. There have been a number of other works that highlight the advantages of the platform. This includes the compatibility with photolithography<sup>2-5</sup>, allowing high Q microring resonators of up to  $2.1 \times 10^6$  being realized, which is important for scaling of AlN-based microcomb devices. Also worth noting is the observation of near octave spanning soliton crystals on AlN, a further exploration of the physics of AlN microrings<sup>5</sup>.

Another major advantage of using single crystalline AlN is its relatively matured growth technology. In our empirical observations, the parameters including height, SHG

efficiency, output comb power, as well as bulk index of the material across multiple wafers have been highly consistent and repeatable. In contrast, popular materials for soliton comb generation like  $\text{Si}_3\text{N}_4$  require the use of more complex fabrication methods like the Damascene process. This relies on multiple processing steps (including a mechanical planarization) and increases the uncertainty of the material parameters such as absolute thickness. Furthermore, it has been found<sup>6</sup> that the index and dispersion properties of  $\text{Si}_3\text{N}_4$  are highly dependent on the precursor gas ratios which further complicate the robustness of soliton generation on  $\text{Si}_3\text{N}_4$ . On the other hand, this section will dive into the robustness of the AlN platform and its ability to produce very repeatable results, which is highly desirable for the frequency comb community.

The demonstration of a self-referenced soliton comb requires two critical components. The first is the device which supports the generation of an octave spanning soliton comb, and the second is the frequency doubler. In all previous works, these two components have been separated. Typically this meant that in order for self-referencing to occur, the signal to be doubled from the frequency comb device must first be amplified, then coupled into a high-efficiency bulk LN doubler. Other methods using auxiliary lasers have also been studied<sup>1,7</sup>. These setups which include the use of an external doubler are non-trivial (often require many servo loops and the control of many degrees of freedom such as the temperature and external environment of both components) and significantly increases the footprint of the system. Integration of frequency doubling and soliton comb generation would have significant impact on the stability of a self-referenced comb and would be a large step towards full integration.

The work presented in this section represents a major step towards integrating the two components. First, we show precise control over the parameters of the AlN devices, where repeatability of these parameters can be achieved on-demand. We then show systematic device optimization for the generation of broadband soliton microcombs as well as highly efficient SHG at the wavelength region of interest, utilizing the methods of designing the

doubly resonant and phase-matching target wavelengths in chapter 2. Finally we show integrated devices with the simultaneous existence of both broadband soliton combs and efficient SHG at the target wavelengths using two different approaches. The first method uses a serial connection of the soliton microring and the doubler microring along a shared bus waveguide. The second method directly couples the soliton microring with the  $\chi^{(2)}$  microring.

## 5.2 Soliton Generation on Aluminum Nitride Microrings

The generation of soliton microcombs occurs spontaneously when there is a stable balance between the Kerr nonlinearity and the dispersive properties of the microresonator in the red-detuned wavelength region of the resonator mode. Typically, due to the small magnitude of Kerr nonlinearity in AlN, this is only achieved with high input powers. Due to the thermal bistability caused by self-phase and cross-phase modulation, as well as the high finesse of microring cavities, the observance of soliton steps at high input powers is a significant challenge. Specifically, due to the much weaker total comb power of a soliton than that of a noisy modulation-instability (MI) comb, the intracavity power drops substantially and suddenly when entering the soliton state. This causes a drastic drop in temperature and results in a significant shift of the resonance, thus disrupting the soliton state. Therefore, the realization of soliton microcombs rely on methods such as power kicking, auxiliary laser, photorefractive effect, temperature tuning and fast sweeping<sup>8</sup>. Due to the soaring interesting of broadband comb generation in AlN microrings, there has been a rapid development of soliton comb generation on the platform. To date, while octave spanning single- and multi-solitons with engineered dispersive waves an octave apart have been realized, further improvements in robustness, repeatability of dispersive wave spectral locations, as well as stability remain highly sought after.

### 5.3 Theoretical Description of Soliton Generation

Generally, two equivalent theoretical descriptions of the soliton generation process is used for its study. The first is in lens of studying the coupling between every individual mode due to Kerr induced four-wave-mixing (FWM). This is the modal expansion approach which has the simplified form

$$\frac{\partial A_\mu}{\partial \tau} = -\frac{\kappa_\mu}{2} A_\mu + \delta_\mu F + ig_{(3)} \sum_{j,k,l} A_j A_k^* A_l e^{i(\omega_j - \omega_k + \omega_l - \omega_\mu)\tau}. \quad (5.1)$$

Where  $A$  is the power amplitude,  $\kappa_\mu$  is the sum of all losses at mode  $\mu$ ,  $\delta_\mu$  denotes the delta function such that the pump term  $F$  affects only the pump mode ( $\mu = 0$ ).  $g_{(3)}$  is the nonlinear coupling rate for the FWM process. This work will not look at the soliton generation process through the lens of modal expansion.

The other approach is to use the Lugiato-Lefever equation (LLE), which is a damped, detuned, and driven nonlinear Schrodinger equation with a periodic boundary condition, written as (normalized by the Kerr nonlinear coupling rate)

$$\frac{d\psi}{d\tau} = -\left(\frac{(\kappa_{ext}(\omega) + \kappa_i)}{\kappa_{tot}} + i\alpha\right) \psi + i|\psi|^2 \psi - i\mathcal{F}^{-1} \{D_{int}(\omega) \odot \mathcal{F}\{\psi\}\} + F. \quad (5.2)$$

Here,  $\psi$  is the normalized amplitude in the ring,  $\frac{(\kappa_{ext}(\omega) + \kappa_i)}{\kappa_{tot}} = 1$  is the normalized total coupling rate including the external  $\kappa_{ext}$  and internal  $\kappa_i$  contributions.  $\alpha$  denotes the detuning of the pump frequency from the mode frequency normalized by the total coupling rate of the microring.  $F$  corresponds to the driving term and the cubic nonlinear term  $i|\psi|^2 \psi$  is the normalized Kerr self-phase modulation. Finally, the expression for  $D_{int}(\omega)$  comes from the Taylor expansion of the mode resonance frequency around the pump mode

$p$  such that

$$\omega_m = \omega_p + \frac{d\omega_p}{dm}m + \frac{1}{2!} \frac{d^2\omega_p}{dm^2}m^2 + \frac{1}{3!} \frac{d^3\omega_p}{dm^3}m^3 + \dots \quad (5.3)$$

$$D_{int}(\omega_m) = \omega_m - \left( \omega_p + \frac{d\omega_p}{dm}m \right). \quad (5.4)$$

These above two formulations of equations 5.1 and 5.2 are identical and can both be solved efficiently using the Fast Fourier Transform (FFT).

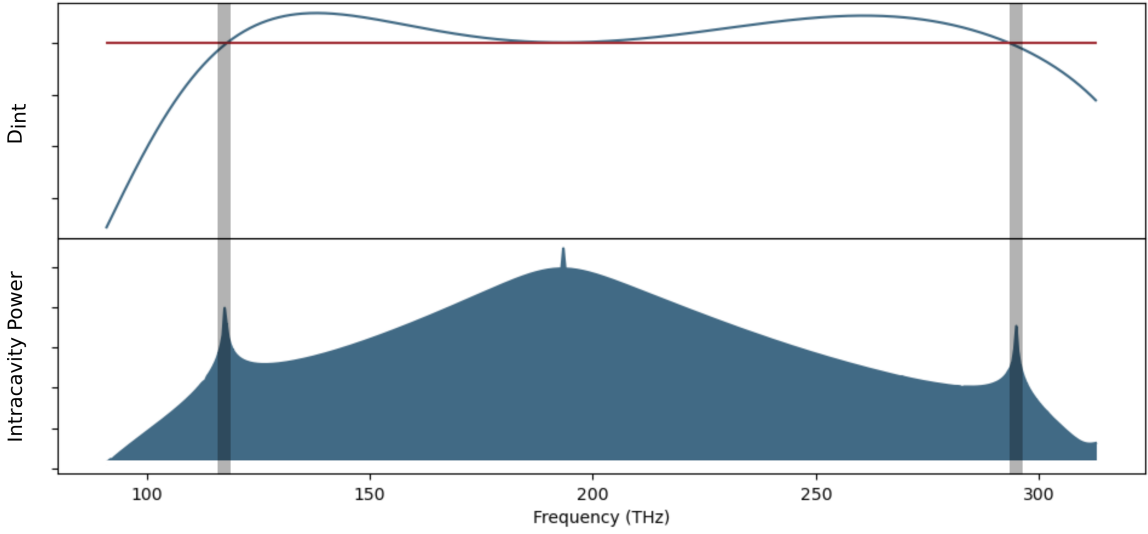


**Figure 5.1:** The top plot displays the integrated dispersion ( $D_{int}$ ) profile of the corresponding intracavity comb power (log-scale) profile of the simulated single soliton comb profile on the bottom. The red line indicates zero  $D_{int}$ . Peaks in the comb power can be associated with zero crossings in  $D_{int}$  as indicated by the shaded regions.

Although this work here heavily involves the simulation of the LLE, detailed derivations of coupled-mode theory and LLE formulation of soliton combs is outside the scope of this thesis and has also been covered in great detail elsewhere<sup>8–11</sup>. However, some details will be needed for the two most important parameters for consideration during the simulation of the LLE. The first is integrated dispersion, which is defined as the detuning between the real resonant frequency (combined with all effects of dispersion) of a mode  $N$  modes away from the pump (where  $N$  is an integer) and the frequency which is  $N$  times

the local FSR away from the pump frequency. This is critical to the design of dispersive waves because a soliton consists of equidistant comb lines that are separated by the FSR at the pump frequency. Therefore, a zero integrated dispersion would correspond to the coincidence of the real frequency of the resonant mode and the frequency which is an  $N \times \text{FSR}$  from the pump frequency, leading to an amplified comb line at that point (also sometimes referred to as the Cherenkov radiation), as shown in Fig. 5.1.

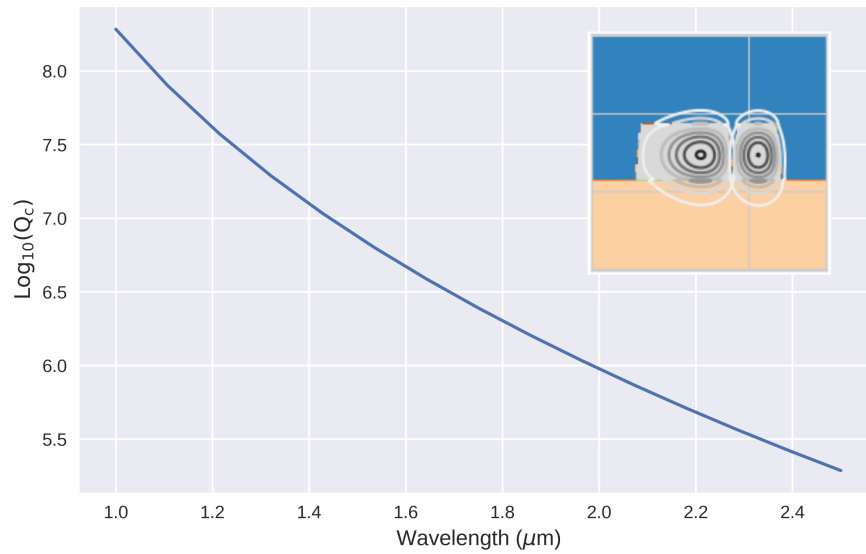


**Figure 5.2:** Wavelength dependence of the coupling  $Q$  ( $Q_c$ ), plotted on logarithm scale. The inset shows the cross sectional simulation of the ring (left) and the bus waveguide (right) mode in commercial software FIMMWAVE, which is then used to calculate the evanescent field overlap.

The second important parameter of consideration is the coupling rate at different frequencies. The bus waveguide of the microring resonator is designed to achieve broadband coupling, however, the coupling rate nonetheless will depend on a multitude of factors. These factors include the width, wrap-around length, as well as proximity from the ring. Ultimately, the coupling with respect to frequency can be calculated by solving for the ring and waveguide modes and extracting the field overlap as well as the phase-matching between the two modes, as depicted in Fig. 5.2, which expresses the coupling rate in terms

of the coupling  $Q$  ( $Q_c$ ). We note that the  $Q_c$  profile in general follows a Sinc function curve with respect to frequency, with a periodicity that can be engineered by the length of the wrap-around. Therefore with careful design, it is possible to have either stronger or weaker coupling at certain wavelengths of interest.

With the simulated integrated dispersion and  $Q_c$  of the microring at all frequencies of interest, Eq. 5.2 can be numerically solved to observe the dynamics of the soliton formation.

## 5.4 Device Modeling

The numerical modeling of the soliton microcomb on AlN can be done by evolving Eq. 5.2 through time. Here the simulation software was optimized to be user-friendly as well as computationally efficient. The programming language of choice is a python front-end using the FFTW package for efficient FFT calculations with a compiled Cython back-end for parallel vector calculations. The simulated spectra agrees well with experimental results as well as a widely available and free software package PyLLE<sup>12</sup>. The comb simulation software is also well integrated with the dispersion and coupling  $Q$  simulation softwares developed for the plotting of Fig. 5.1 and Fig. 5.2. One can simply run the desired calculation for the integrated dispersion and  $Q_c$  profile for a device configuration and use them as an input to the comb simulation software. Fig. 5.3(a) displays the integrated dispersion profile, (b) is the simulated total comb power as the pump frequency is swept from start to finish, (c) depicts the intracavity and in-waveguide comb spectrum in the frequency domain at the red starred snapshot of (b), and (d) is the corresponding temporal profile of (c).

For the numerical simulation, the split-step method was used for the calculation of the comb dynamics, where the nonlinear effects were calculated in the time domain and the dispersion and losses were solved for in the frequency domain. In order to increase



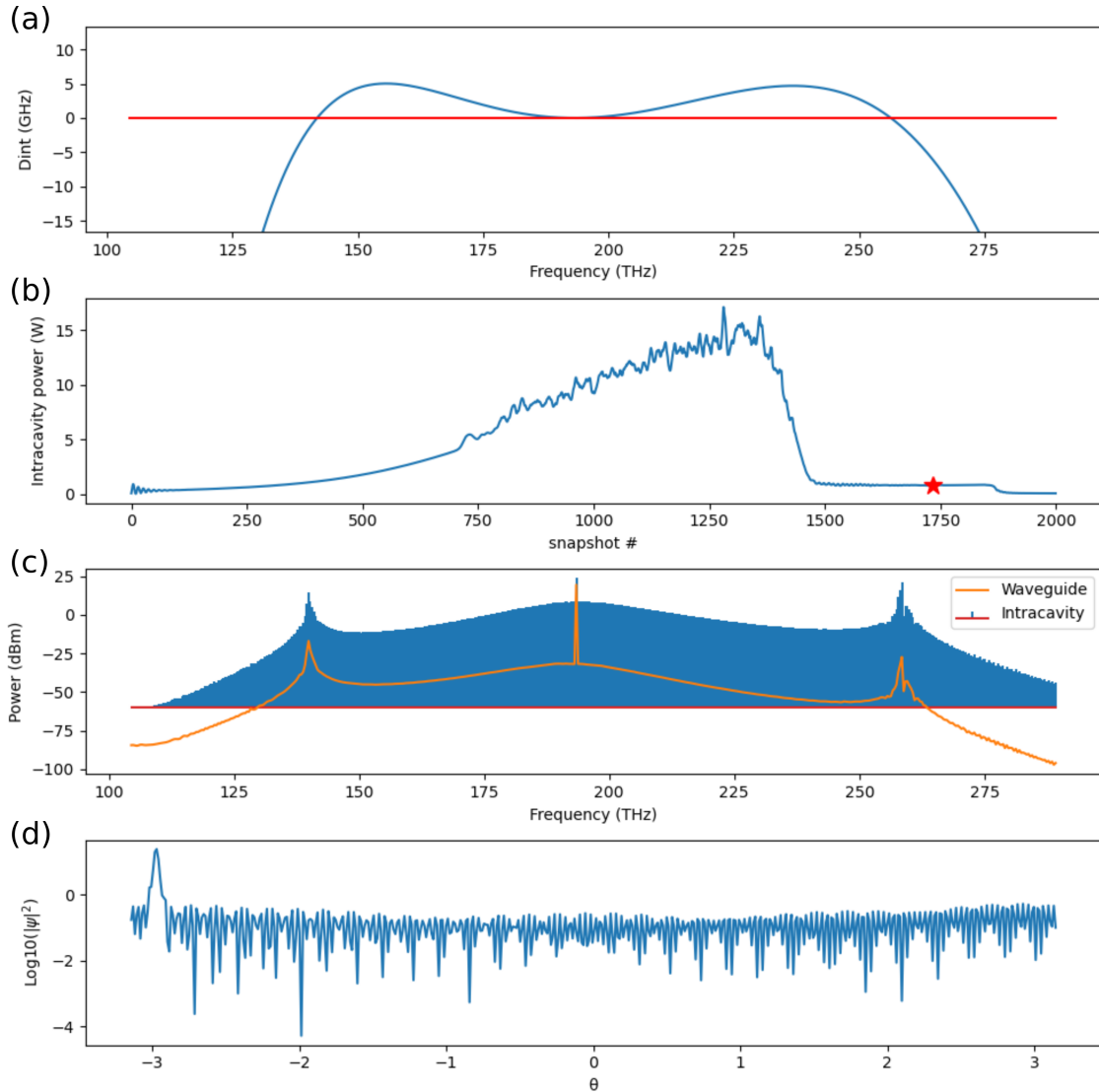


**Figure 5.3:** Simulated comb dynamics. (a) A plot of the integrated dispersion profile used in the simulation. (b) Comb power throughout the simulation at each snapshot as the pump frequency started from the blue-detuned region to the red-detuned region. Total simulated time was  $1 \mu\text{s}$ , and was divided into 2000 equally spaced in time "snapshots" and plotted. Pump frequency in simulation was tuned from 193.4156 THz to 193.4124 THz. (c) Plotted comb power for each simulated mode frequency at the starred snapshot of (b), where the blue stem-plot is the intracavity power and the orange curve is the waveguide power. (d) The temporal profile of (c), where  $\theta$  represents the radial location within the microring.

accuracy of the solution as well as to preserve time symmetry (such that moving forward and then backward in a single time-step will not produce a different solution), a half step was implemented in frequency domain before and after a full step in the time domain.

Finally, it is common to require comb simulations of rings with large radii and high power especially in systems where the Kerr nonlinearity may not be significant. Simulations of modes in excess of 1000 and watts of input power will require proportionally small time-steps for an accurate simulation of the comb spectrum. In these cases, it may take up to hours of simulation time which may not be ideal for testing purposes. Therefore it is important to utilize an optimized software. Although a free software package PyLLE is widely available, which utilizes a python front end and a Julia language back-end for efficient linear algebra calculations, for a simulation of 500 mW, 100  $\mu\text{m}$  radius, 1024 modes, and a total simulated time of 1  $\mu\text{s}$ , PyLLE still requires 51 minutes of run-time on an AMD Ryzen 5 3600 processor with 6 cores and 12 threads.

Here, the simulations were optimized by (1) using the Fastest Fourier Transform in the West (PyFFTW) package which is an optimized library for discrete Fourier transforms, (2) integration of Cython to precompile the most computationally expensive parts of the split-step algorithm and (3) utilizing parallel computing (multiple threads) by unrolling certain element-wise vector operations such as the calculation of the dispersion component in the frequency domain of the split-step algorithm.

The resulting time it takes for the same calculation as above (500 mW, 100  $\mu\text{m}$  radius, 1024 modes, and a total simulated time of 1  $\mu\text{s}$ ) using the processor noted (AMD Ryzen 5 3600), using 8 threads, is reduced to 16 minutes. Achieving further significant speedups may require more parts of the code being precompiled, or by utilizing a different algorithm. In terms of speed, the current bottleneck when solving for many modes is in the exponential, additive, and multiplicative operations and not necessarily the FFT operations.

## 5.5 Device Design

As noted previously, for applications in self-referenced, stable soliton combs, one of the most important properties of the comb is that it must be broadband (octave spanning). In order to achieve this, it is imperative to engineer the integrated dispersion profile to possess two zero crossing points (excluding at the pump frequency) an octave apart, which will provide an amplified signal at the corresponding frequencies. This will allow the comb lines at those frequencies to be more easily detected and thus useful for implementing f-2f self-referencing. Furthermore, consistently achieving a soliton comb on every device is not an easy task due to competing processes that may be more stable than the soliton state. One major competing process is Raman lasing, which one must take steps to avoid in order to generate a soliton comb on AlN microrings. To do so requires the fine adjustments of the microring parameters to avoid parametric amplification near the Raman gain bandwidth.

### 5.5.1 Octave Spanning Soliton Combs

#### Dispersion engineering

Arguably the most important parameter to optimize for when trying to achieve broadband combs is the dispersion, in comparison to Q factor enhancement or decreasing mode volume. The three degrees of freedom of interest here are the ring width, height and radius.

In choosing the ring radius, several trade-offs are considered. A small ring radius will offer larger FSR, and therefore subsequently the comb generation will be more power-efficient, since less comb lines are needed for an octave spanning comb. However, this will increase the scattering (bending) losses due to more interaction with the side-wall roughness and thus lowering the intrinsic Q factor of the microring device. However, too large of a radius will increase the power requirement and the probability of overlap between the Raman gain bandwidth and a resonant mode. Although a large radius will decrease bend-

ing losses, it will also require a bus waveguide that is closer in proximity (smaller coupling gap) to the ring, and thus introduce more scattering losses in the external coupling region of the microring. Our experiments have found that a  $60\ \mu\text{m}$  radius generally works well for broadband soliton generation, although further fine-tuning is needed to avoid stimulated Raman scattering.

For the design of ring width, the spectral location of the soliton comb dispersive waves is of consideration since dispersive waves are important for achieving broadband combs. The relationship between dispersive waves and ring width on AlN microrings is well documented. As the ring width increases, there is a tendency for the dispersive waves to deviate away from the pump frequency. In our experiments, octave spanning soliton combs have been achieved in the range of ring widths from  $2.3$  to  $2.5\ \mu\text{m}$ .

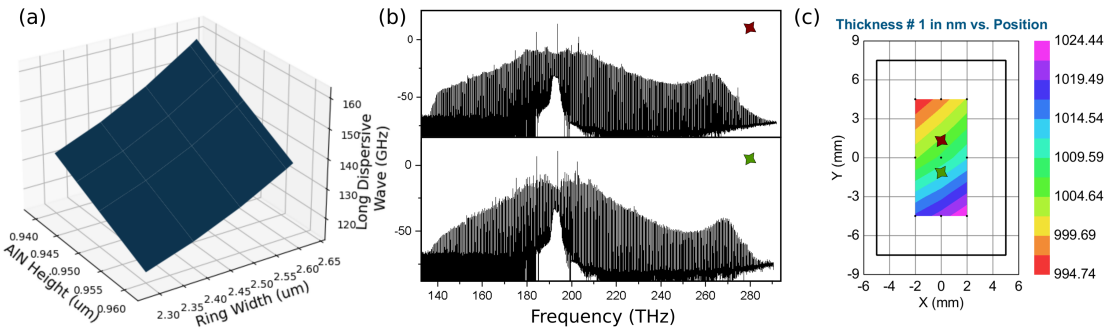


**Figure 5.4:** (a) Dependence of the long wavelength dispersive wave (LWDW) frequency on both AlN height and the ring width, note that the same change in height produces a much larger difference in the frequency of the LWDW compared to the same change in ring width. (b) Experimental observation of the change in LWDW frequency and the overall comb spectrum due to a  $\approx 10$  nm difference in height indicated by the red and green starred location of the devices on the chip in (c) which is a map of the height variation within the measured chip.

Perhaps an often overlooked but extremely important parameter is the height of the nonlinear material (AlN). Since the fundamental TM mode is used for soliton comb generation, its field profile is often more prominent in the vertical ( $z$ ) direction, thus its group velocity index is highly sensitive to the height compared to the fundamental TE mode. Small changes on the order of nanometers in height would lead to drastic differences in

the spectral locations of the dispersive waves. This dependence is shown in Fig. 5.4(a-c). Additionally, comb spectrums of two devices with the same parameters (including normalized transmission at telecom wavelengths and input power) except height is depicted, which shows not only a shift in the dispersive waves, but also a general difference in the comb line output power. This can be explained by the fact that increasing the height not only leads to dispersive waves deviating from the pump frequency, but also the higher peak of the integrated dispersion curve. In our experiments, we have chosen a range of heights between 990 nm and 1010 nm which empirically allows us to generate octave-spanning soliton comb spectrums.

### **Thermal nonlinearity**

Overcoming the thermal nonlinear shifts is a major challenge which has sparked many research efforts. Thermal nonlinear shift on single crystal AlN (c-AlN) is generally much less pronounced than that of poly-crystalline AlN. However, due to the thermal-optic coefficient of c-AlN, a typical thermal triangle of  $\approx 0.1$  nm at waveguide input powers of 400 mW will still occur at scanning speeds of 10 nm/s, blinding any observance of soliton steps. To overcome this, the laser sweeping is first operated manually to the red-detuned region of the resonant mode. The pump laser is then passed through a single-side-band modulator which receives an input periodic signal from an arbitrary function generator (AFG) in order to achieve a fast sweeping over the resonance and prevent the build-up of temperature. A scanning speed of 3000 pm/ $\mu$ s was used for the generation of soliton combs. As the AFG generates a periodic signal which scans over the resonance, a photodetector is used to measure the comb power simultaneously and is used as a trigger to stop the AFG signal output and to initiate a servo locking on the soliton step. A more detailed description of the scheme can be found elsewhere<sup>2</sup>.

## Avoidance of Raman processes

The Raman effect is the inelastic (outgoing photons have a different frequency than input photons) scattering of photons by lattice phonon modes. In a microring, this effect can be enhanced by the cavity such that stimulated Raman scattering occurs. Under ideal conditions, the threshold for stimulated Raman scattering can be low enough such that it becomes favorable over the generation of a soliton comb. This occurs when two conditions are met: (1) there is a large overlap of the Raman gain bandwidth peak and a fundamental TM resonance mode. For c-AlN, the bandwidth occurs near 1700-1740 nm. To avoid this, careful design of the microring parameters can allow the microring modes to avoid the peak of the bandwidth, and thereby increasing the threshold of stimulated Raman scattering. (2) The losses at the Raman gain bandwidth is low. Thus, it is possible to engineer external losses to occur more prominently at the 1700-1740 nm using clever bus waveguide designs through precisely controlled wrap-around lengths and other external coupling techniques<sup>13</sup>.

When the above ideal conditions for stimulated Raman scattering are met, there is fierce competition between the Raman processes and the Kerr FWM processes. This can be observed in a comparison of output comb power spectrums of a microring with optimized Raman scattering and a microring without (Fig. 5.5(b-c)).

In this work, we first systematically finely vary the parameters (<50 nm step-sizes) (ring width, height, bus waveguide width, bus waveguide wrap-around length, radius) of the microring, guided by the analysis of chapter 2. This allowed the microring modes to avoid the peak of the Raman gain bandwidth and finally the absence of low-threshold stimulated Raman scattering was repeatable across multiple chip fabrications.

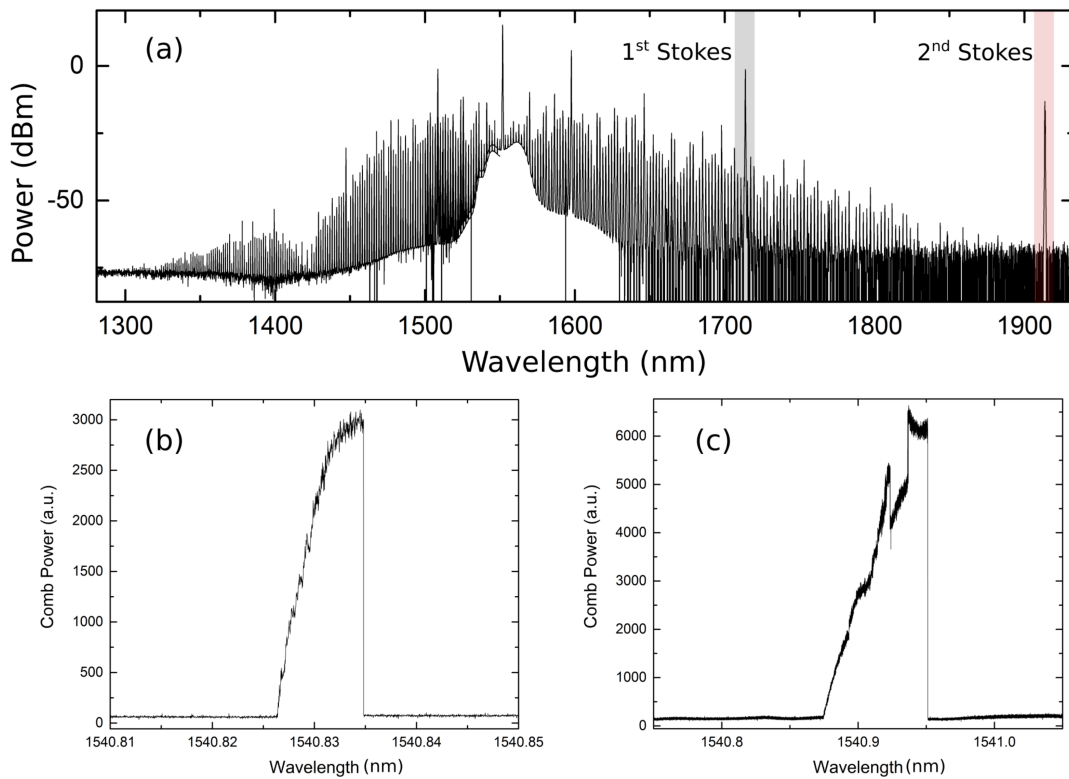


**Figure 5.5:** (a) A comb spectrum showing the presence of both the stimulated Raman scattering process and Ker four-wave-mixing, the first stokes line is at 1706 nm and the second stokes line is located at 1905 nm. (b) A plot of total comb power with respect to pump wavelength, scanned across the resonance at a speed of 10 nm/s, this plot shows no presence of stimulated Raman scattering. (c) A plot of total comb power which shows Raman interactions. In general the observance of stimulated Raman scattering is correlated with the observance of a larger thermal triangle.

## 5.5.2 Device Fabrication

In order to achieve the previously mentioned fine-tuning of the height, one must have nanometer-level control of the height while preserving the quality of the material (i.e. surface roughness). Conventionally, the dry-etching of AlN requires a chemical reaction component based on a  $\text{BCl}_3/\text{Cl}_2$  gas. However, in order to achieve a smoother surface and finer control of the height, an ion-milling recipe using an Ar plasma with an RF power of 150 W was developed instead to achieve the task. Fig. 5.6(a-b) displays the before and after etching results, which shows an even etching over the chip surface, as the variation of the height remains approximately the same. The final microring device fabricated as a result of this etching recipe showed no degradation in experimental Q factor.

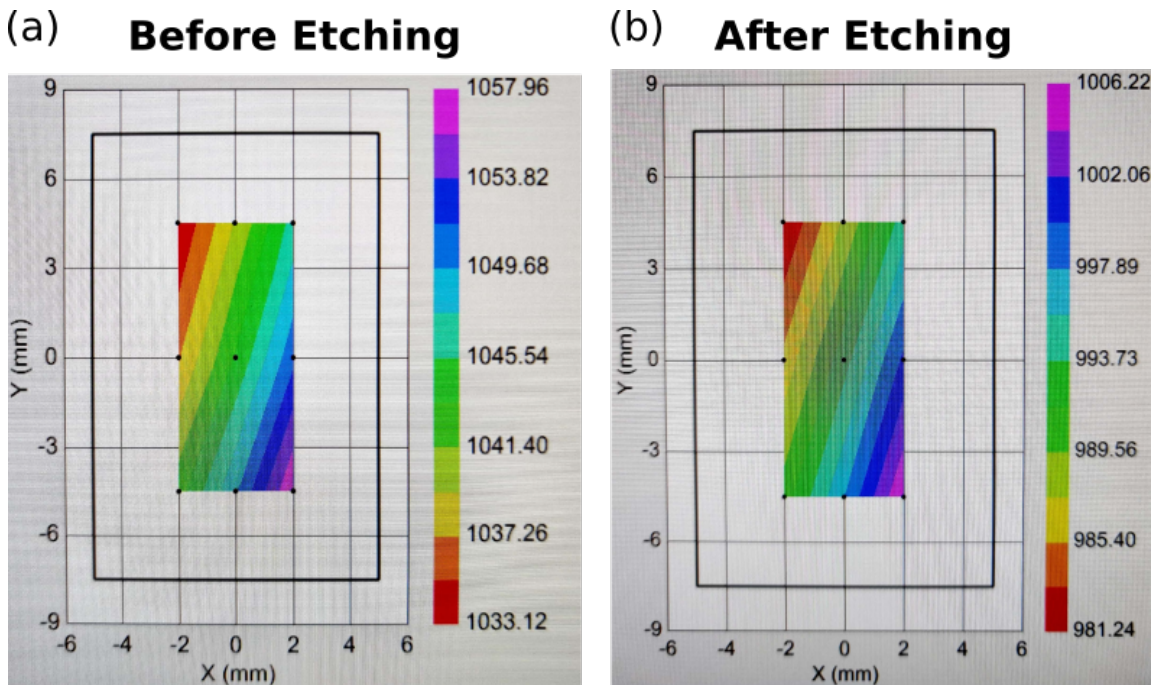


**Figure 5.6:** Before and after ion milling. (a) The variation of height in nanometers over a photonic chip before processing. (b) Variation of height in nanometers over the same photonic chip after ion-milling and before patterning and fabrication of the microring devices.



## 5.6 Coupled Rings for the Integration of Frequency Doubling and Comb Generation

Efforts to integrate frequency doubling and soliton comb generation onto a single chip have been on-going. For the  $\text{Si}_3\text{N}_4$  platform which is arguably the most popular platform for soliton comb generation, due to the centro-symmetric nature of the material, second order nonlinear interactions such as SHG is not typically possible. This can be overcome by using photo- or electric-field induced SHG<sup>14,15</sup>, as well as engineering non-symmetries in the material by introducing stress on the  $\text{Si}_3\text{N}_4$  film. The research efforts in  $\chi^{(2)}$  technologies on  $\text{Si}_3\text{N}_4$  remains nascent.

The proof of concept demonstration of  $f_{ceo}$  detection on the AlN platform has recently been achieved by our group and has perhaps one of the greatest potential of all existing platforms for full integration. However, it remains difficult to achieve for multiple reasons outlined below.

There are two main approaches for SHG on AlN, each with its own set of challenges. The most straight-forward way which requires no resonance alignment is through the use of a straight waveguide, as demonstrated in a previous work<sup>16</sup>. However, due to its low efficiency, high power auxiliary lasers are needed for the detection and stabilization of the  $f_{ceo}$ . Furthermore, the increased length of the bus-waveguide also results in a decrease of comb power extraction efficiency. The other method which has been studied in detail through the work of this thesis is the use of dually resonant microrings. Using resonant structures will significantly decrease the power requirements of the system and also may allow us to eventually avoid the use of an auxiliary laser for  $f_{ceo}$  detection. The challenge of this approach is primarily in the alignment of the double resonances, which we have addressed previously by the systematic fine-tuning of microring parameters as well as the optimization of highly reproducible fabrication techniques.

In this work, a device design which couples a high efficiency SHG microring (doubler) with a soliton microring was chosen over a design which connects a doubler in series along the same bus waveguide. This was done in order to increase control over the coupling between the mode of the soliton and the mode of the doubler.

### 5.6.1 Theoretical Description

In order to determine whether the soliton comb generation process will be affected significantly by the microring doubler, it is critical to understand the soliton generation and SHG process of a coupled resonator system from a numerical standpoint.

#### Soliton generation

In the coupled ring resonator system, a few simplifying assumptions were made for the analysis. First, due to the low powers coupled from the soliton ring (denoted as ring A) into the doubler (denoted as ring B), the SH interactions are in the non-depletion regime. Therefore when studying the comb generation dynamics, the effects of coupling into the SH modes can be ignored. Second, every mode of ring A (or B) is only coupled to at most one mode of ring B (or A), furthermore, only coupling between modes within 5 line-widths away (i.e.  $10\kappa_{tot}$ ) are considered.

Ignoring the SHG contributions, we can then analyze the system in the rotation frame of

$$\sum_{j=1}^M (\omega_{f,j}) a_j^\dagger a_j + \sum_{k=1}^N (\omega_{f,j'}) b_k^\dagger b_k, \quad (5.5)$$

where  $M$  and  $N$  are the total number of modes in consideration for the numerical analyses of ring A and B respectively.  $a_j$  is the  $j^{\text{th}}$  mode of ring A and  $b_k$  is the  $k^{\text{th}}$  mode of ring B.  $\omega_{f,j}$  is the mode  $j$  frequency due to the FWM process of soliton comb generation, this is different from the real mode frequency which includes the contributions of integrated dispersion.  $\omega_{f,j'}$  is the  $\omega_{f,j}$  which is spectrally closest to the real frequency of mode  $b_k$ . In

this rotation frame, we can ignore all of the phase contribution terms of the coupled modes and focus on the relevant physical dynamics.

We further express the normalized (such that frequency shifts are in terms of number of linewidths and the Kerr nonlinear coupling rate is 1, details of the normalization can be found in the source code appendix B) coupled LLEs that include the interaction terms of resonators A and B as

$$\begin{aligned} \frac{d\psi_A}{d\tau} = & i|\psi_A|^2 \psi_A - \mathcal{F}^{-1} \{ (i\Phi_A + \xi_A(\omega)) \odot \mathcal{F} \{ \psi_A \} \} \\ & - \mathcal{F}^{-1} \{ i\kappa_{BA}(\omega) \odot \mathbf{T}_{BA} \mathcal{F} \{ \psi_B \} \} + \frac{F}{\psi_A} \psi_A \end{aligned} \quad (5.6)$$

$$\begin{aligned} \frac{d\psi_B}{d\tau} = & i|\psi_B|^2 \psi_B - \mathcal{F}^{-1} \{ (i\Phi_B + \xi_B(\omega)) \odot \mathcal{F} \{ \psi_B \} \} \\ & - \mathcal{F}^{-1} \{ i\kappa_{AB}(\omega) \odot \mathbf{T}_{AB} \mathcal{F} \{ \psi_A \} \}. \end{aligned} \quad (5.7)$$

Where  $\psi_{A(B)}$  denotes the normalized intracavity amplitude,  $\mathcal{F}$  is the discrete Fourier transform,  $\odot$  corresponds to the element-wise multiplication operator, and  $\xi(\omega) = \frac{(\kappa_{ext}(\omega) + \kappa_i)}{\kappa_{tot}}$  is the normalized coupling rate. We have the expression for  $\vec{\Phi}_{A(B)}$

$$\begin{aligned} \vec{\Phi}_A = & \vec{D}_{int}^A(\omega) + \vec{\Delta}_A \\ = & \begin{bmatrix} D_{int}^A(\omega_0) \\ D_{int}^A(\omega_1) \\ \vdots \\ D_{int}^A(\omega_M) \end{bmatrix} + \begin{bmatrix} \omega_0 - (\Delta\omega_{FSR}^A(j-p) + \omega_f) \\ \vdots \\ \omega_{j=p} - \omega_f \\ \vdots \\ \omega_{j=M} - (\Delta\omega_{FSR}^A(M-p) + \omega_f) \end{bmatrix} \end{aligned} \quad (5.8)$$

$$\begin{aligned}
\vec{\Phi}_B &= \vec{D}_{\text{int}}^B(\omega) + \vec{\Delta}_B \\
&= \begin{bmatrix} D_{\text{int}}^B(\omega_0) \\ D_{\text{int}}^B(\omega_1) \\ \vdots \\ D_{\text{int}}^B(\omega_N) \end{bmatrix} + \begin{bmatrix} \omega_0 - (\Delta\omega_{\text{FSR}}^A(j' - p) + \omega_f) \\ \vdots \\ \omega_k - (\Delta\omega_{\text{FSR}}^A(j' - p) + \omega_f) \\ \vdots \\ \omega_{k=N} - (\Delta\omega_{\text{FSR}}^A(N - p) + \omega_f) \end{bmatrix}, \tag{5.9}
\end{aligned}$$

which is the total contributions of frequency detuning (from the zero dispersion case) including integrated dispersion  $\vec{D}_{\text{int}}(\omega)$  and the detuning of the real mode frequencies from the soliton FWM terms  $\vec{\Delta}$ . Here,  $j'$  denotes the ring A mode which is closest in absolute frequency to the  $k^{\text{th}}$  mode of ring B and  $\omega_{\text{FSR}}^A$  is the FSR of ring A at the pump frequency  $\omega_f$ .  $\vec{D}_{\text{int}}(\omega)$  is precomputed from either FIMMWAVE or COMSOL and is static throughout the numerical simulation. In order to determine  $j'$ , the real mode frequencies are determined for ring A and ring B, and subsequently only the modes between A and B within 5 linewidths apart are taken into consideration by implementing the transfer matrix  $\mathbf{T}_{AB(BA)}$ . Finally,  $\kappa_{AB(BA)}(\omega)$  represents the frequency dependent coupling rate between the two microrings.

For the numerical simulation of the coupled rings system, we can vectorize the nonlinear differential equations as

$$\vec{\psi}'(t) = \mathbf{A}\vec{\psi}(t),$$

which in general has a solution of the form

$$\vec{\psi}(t) = e^{\mathbf{A}t}\vec{\psi}_0.$$

Such that if we advance a single time-step of  $dt$ , we arrive at

$$\begin{aligned}
\vec{\psi}(t+dt) &= e^{\mathbf{A}(t+dt)} \vec{\psi}_0 \\
&= e^{\mathbf{A}dt} \vec{\psi}(t) \\
&= e^{(\mathbf{N}+\mathbf{D})dt} \vec{\psi}(t),
\end{aligned} \tag{5.10}$$

where

$$\mathbf{N} = \begin{bmatrix} i|\psi_A|^2 + \frac{F}{\psi_A} & 0 \\ 0 & i|\psi_B|^2 \end{bmatrix} \tag{5.11}$$

$$\mathbf{D} = \begin{bmatrix} -\mathcal{F}^{-1} \left( i\vec{\Phi}_A + \vec{\xi}_A(\omega) \right) \odot \mathcal{F} & -\mathcal{F}^{-1} \left( i\kappa_{BA}(\omega) \odot \mathbf{T}_{BA} \right) \mathcal{F} \\ -\mathcal{F}^{-1} i\kappa_{AB}(\omega) \odot \mathbf{T}_{AB} \mathcal{F} & -\mathcal{F}^{-1} \left( i\vec{\Phi}_B + \vec{\xi}_B(\omega) \right) \odot \mathcal{F} \end{bmatrix}. \tag{5.12}$$

Eq. 5.10 can be approximated by the symmetric split-step method with an error that scales at  $O(dt^2)$ ,

$$\vec{\psi}(t+dt) = e^{\mathbf{D}\frac{dt}{2}} e^{\mathbf{N}dt} e^{\mathbf{D}\frac{dt}{2}} \vec{\psi}(t) \tag{5.13}$$

### SHG analysis

In this subsection, we investigate the coupling of an A mode ( $a$ ) with a B ( $b$ ) mode and its effect on the SH process (mode  $c$ ). The purpose is to identify the best coupling regime between the two microrings for our purposes of soliton generation and efficient SHG.

The total transformed Hamiltonian is

$$\begin{aligned}
\check{H} &= \delta_a a^\dagger a + \delta_b b^\dagger b + \delta_c c^\dagger c + \kappa_{AB} \left( a^\dagger b + b^\dagger a \right) \\
&+ g \left( b^2 c^\dagger + \left( b^\dagger \right)^2 c \right) + i \sqrt{2\kappa_{a,1} \frac{P_f}{\hbar\omega_f}} \left( -a e^{i\omega_f t} + a^\dagger e^{-i\omega_f t} \right),
\end{aligned} \tag{5.14}$$

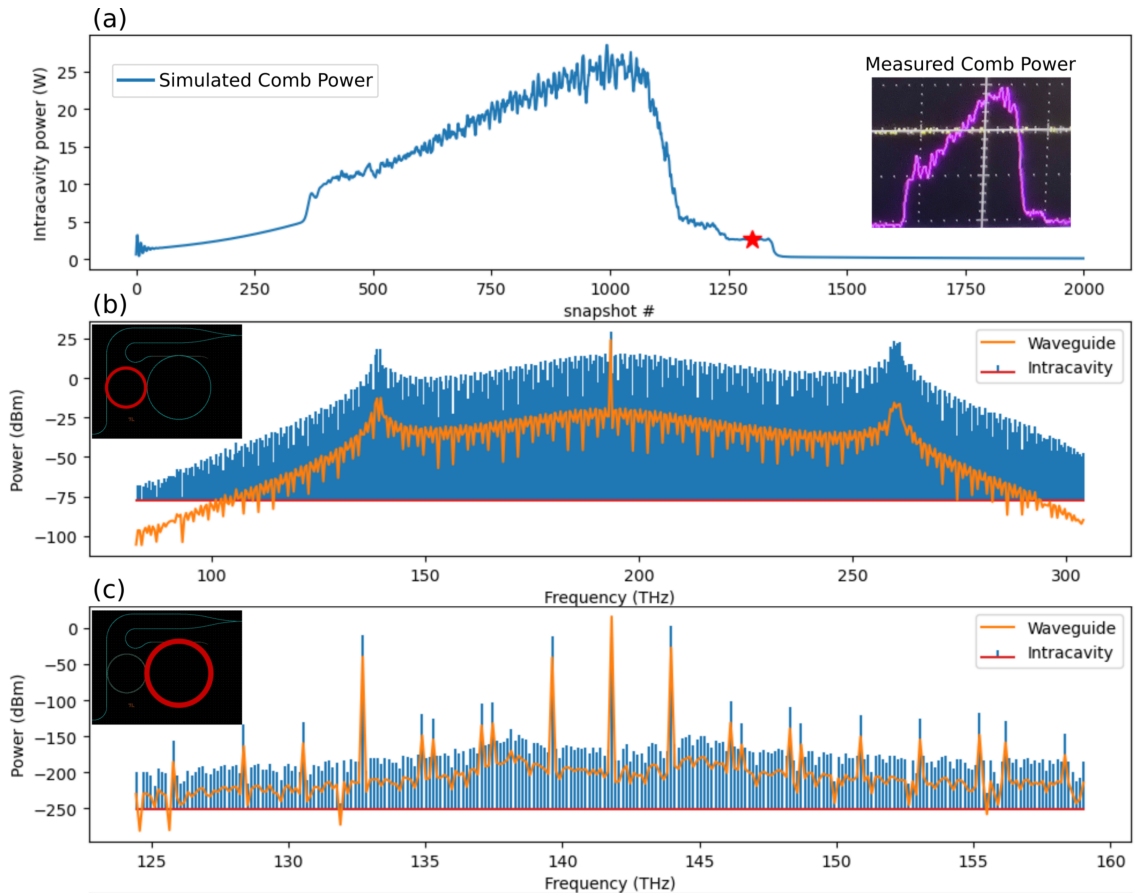


**Figure 5.7:** Numerical modeling of the coupled rings. (a) The simulated total comb power as the pump laser is swept over the resonance. In the inset is a measured comb power spectrum from a coupled microrings device. (b) Simulated intracavity and waveguide soliton comb spectrum corresponding to the detuning of the red star in (a). This corresponds to the intracavity power in the soliton ring highlighted in red. (c) Simulated coupled intracavity and waveguide power spectrum in the doubler ring. A corresponding theoretically achievable SHG efficiency of  $50,000\%/W$  would produce an in-waveguide SH power of  $-63$  dBm at 288 THz.

such that the Heisenberg equations of motion can be written as

$$\begin{aligned}
\dot{a} &= -X_a a - i\kappa_{AB} b + \varepsilon_a \\
\dot{b} &= -X_b b - igb^* c - i\kappa_{AB} a \\
\dot{c} &= -X_c c - igb^2.
\end{aligned} \tag{5.15}$$

Here  $X_l = i\delta_l + \kappa_l$ ,  $l \in \{a, b, c\}$  and  $\varepsilon_a = \sqrt{2\kappa_{a,1} \frac{P_f}{\hbar\omega_f}}$ .  $\kappa_{AB}$  denotes the coupling rate between the two microrings and  $g$  is the second order nonlinear coupling rate. At steady state, and rearranging to solve for mode amplitudes, we arrive at the following expressions for the various modes

$$\begin{aligned}
a &= \frac{-i\kappa_{AB} b + \varepsilon_a}{X_a} \\
b &= \frac{-i\kappa_{AB} \varepsilon_a}{X_b X_a + \kappa_{AB} + \frac{g^2 |b|^2}{\frac{X_c}{X_a}}} \\
c &= \frac{-igb^2}{X_c}.
\end{aligned} \tag{5.16}$$

The above equations can be used to solve for the steady state of the mode photon numbers  $|a|^2$ ,  $|b|^2$ , and  $|c|^2$ . Finally we can solve for the transmitted telecom power as well as the output SH power in the waveguide.

$$P_{trans} = P_f \left| 1 - \frac{-2\kappa_{a,1} \kappa_{AB}^2}{X_b X_a^2 + \kappa_{AB}^2 X_a + \frac{g^2 X_a |b|^2}{X_c}} - \frac{2\kappa_{a,1}}{X_a} \right|^2 \tag{5.17}$$

$$P_{SH} = \hbar\omega_c \left| \frac{i\sqrt{2\kappa_{a,1}} g b^2}{X_c} \right|^2. \tag{5.18}$$

## 5.7 Results and Discussion

First, we demonstrate control over the dispersive waves' spectral location as shown in Fig. 5.8, where the broadening of the soliton comb can be seen as the ring width narrows.

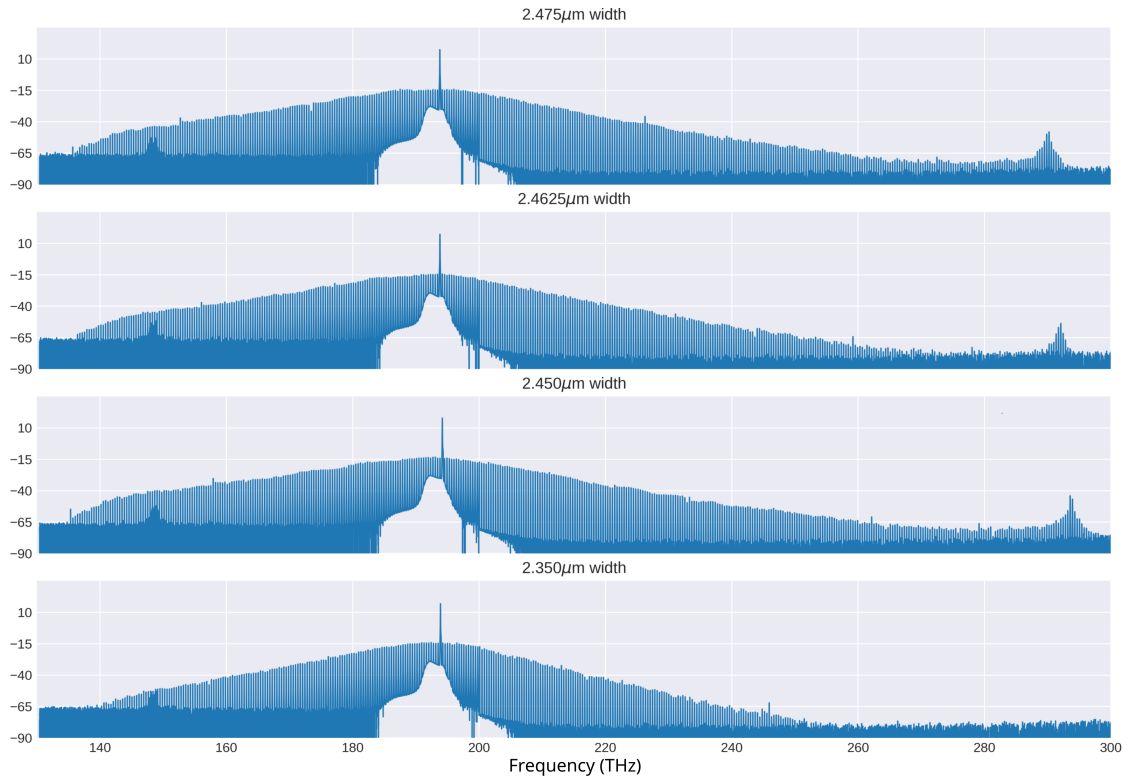


**Figure 5.8:** Measurement of soliton comb microring devices with varying widths. The dispersive waves tend to deviate away from the pump line as the ring width decreases, indicating a broadening of the corresponding integrated dispersion profile.



The devices measured had a fixed ring radius of  $60\ \mu\text{m}$  and a bus waveguide width of  $1.15\ \mu\text{m}$  with a wrap-around angle of 5 degrees. In Fig. 5.9 we also demonstrate the ability to simultaneously achieve a soliton comb and SHG along the same bus-waveguide by coupling a cascade of microring doublers in serial with the soliton microring.

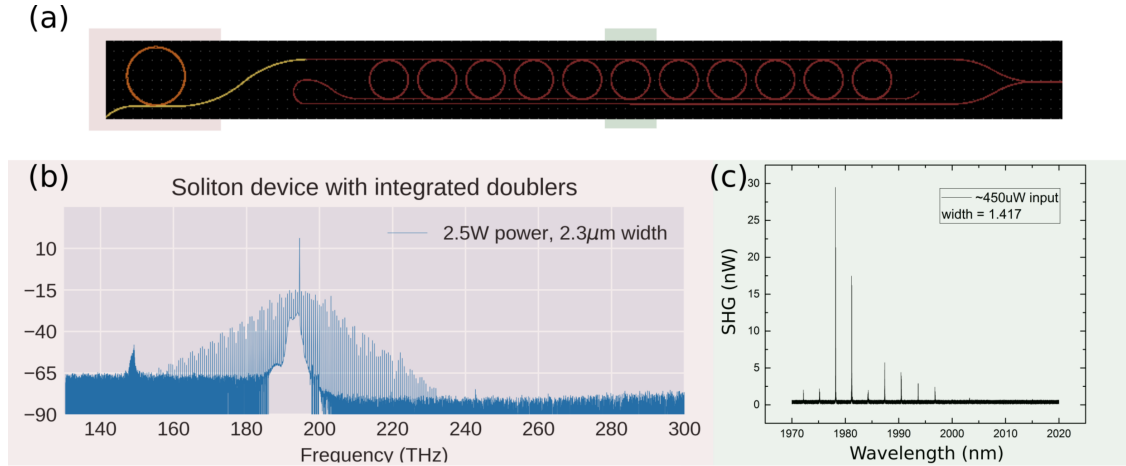


**Figure 5.9:** Simultaneous observance of SHG and soliton microcomb. (a) Generated to-scale image of the device measured, where the red shaded device is the soliton microring and the green shaded device is the microring doubler. (b) Multi-soliton spectrum generated by the microring with an input power of 2.5 W. (c) Measurement of SHG at  $450\ \mu\text{W}$  of input power.

There are, however, significant challenges with using a serial connection of the soliton microring and the doublers. Mainly, in order for a specific comb line to be doubled, the wavelength of the particular mode must be within a linewidth of the doubler microring mode, which can be non-trivial to realize. Furthermore, the coupling between the two rings is not as easily engineered since there are two coupling regions that light must pass through from the soliton ring to the doubler ring. In contrast, mode hybridization occurs when the two rings are directly coupled, where it is easier to engineer a high coupling rate that can produce a much broader range of frequencies in which the comb mode and the SH mode may interact. This is illustrated more clearly in Fig. 5.10, where a ring-to-ring coupling rate of  $\kappa_{AB} = 10 \times \kappa_{a,1}$  is used. The figure shows that reasonably efficient SHG can be realized at a mode-mismatch bandwidth of a significant portion of the FSR,

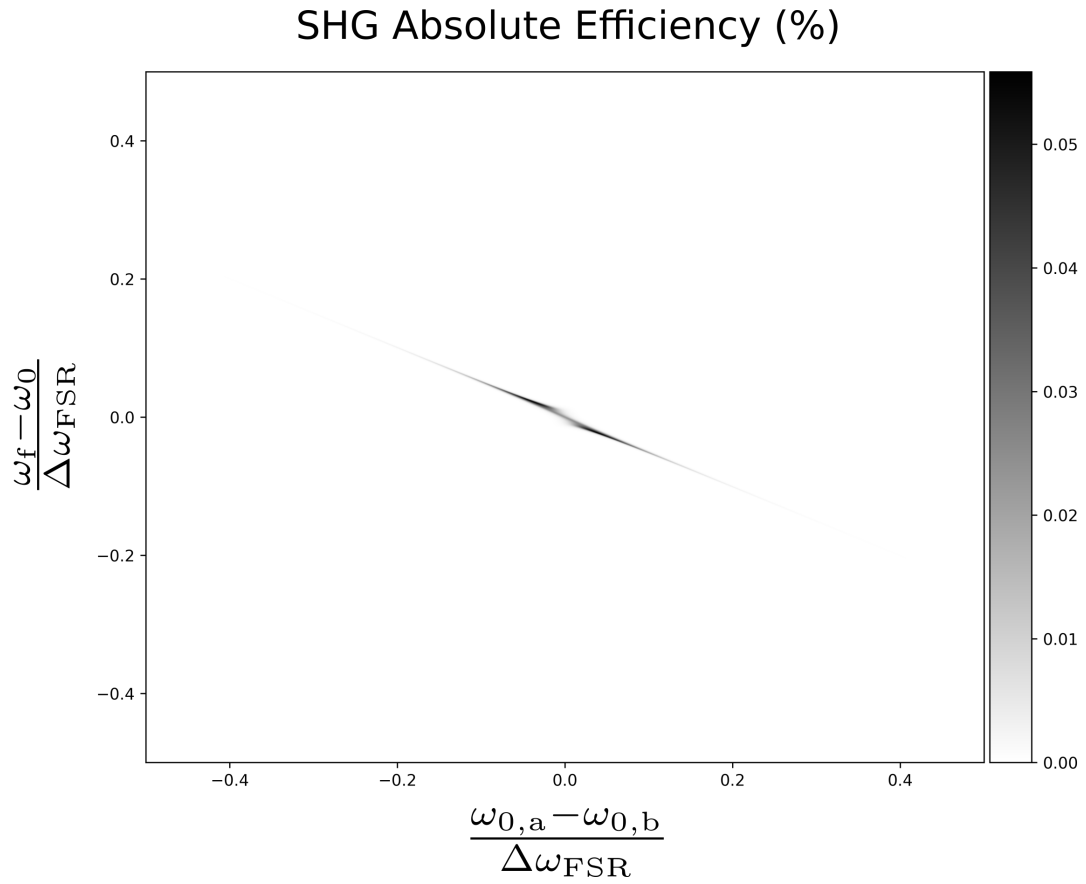


**Figure 5.10:** Simulation of SHG from the auxiliary doubler microring. The x-axis is the detuning of the two coupled modes while the y-axis is the pump detuning. Both axes are normalized by the FSR. A coupling rate of 1.5 GHz was used.

which means one can worry much less about the very specific frequency matching of the microring modes. Note that the coupling rate  $\kappa_{AB} = 10 \times \kappa_{a,1}$  can be realized relatively easily at  $2 \mu\text{m}$  as shown in Fig. 5.2.

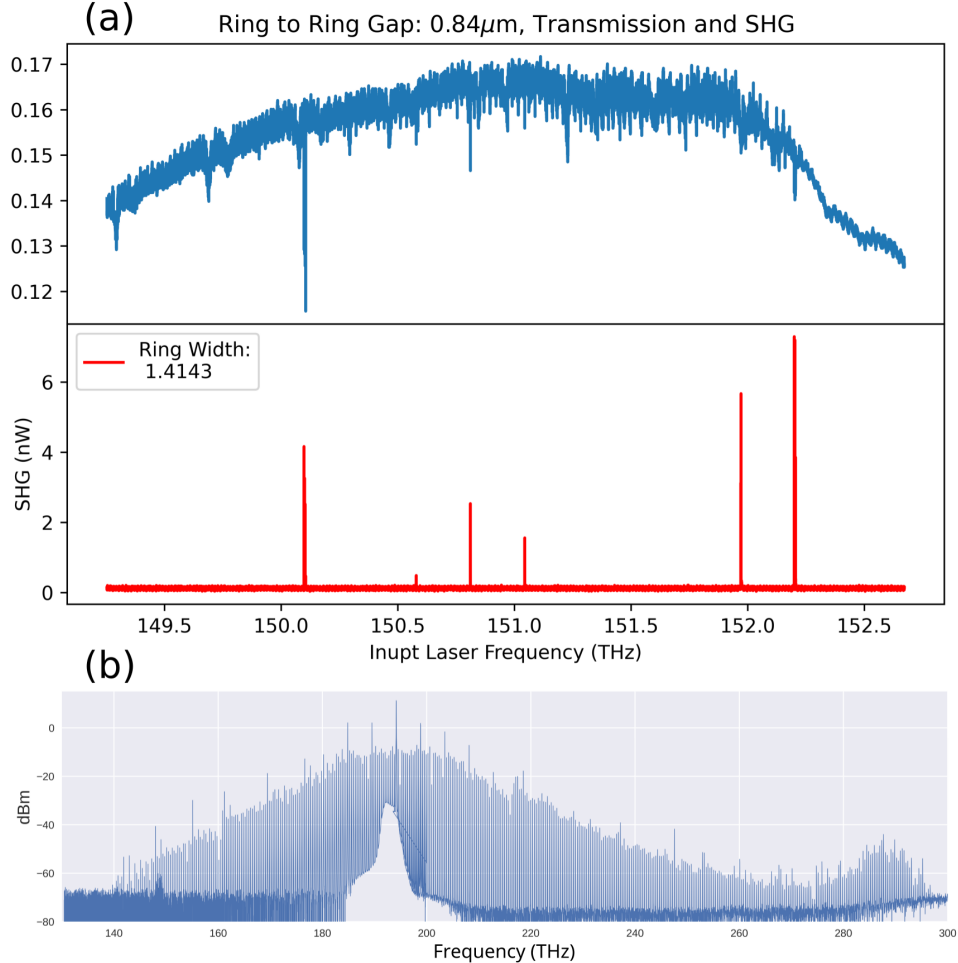


**Figure 5.11:** Simultaneous observance of broadband comb and high efficiency SHG. (a) Display of the transmission and corresponding SHG spectrum of the doubler (auxiliary) ring coupled to the primary ring. The measurement was performed using a  $2 \mu\text{m}$  tunable laser set at  $800 \mu\text{W}$  corresponding to waveguide power of  $300 \mu\text{W}$ . (b) MI comb from the primary ring, spanning greater than one octave.

Finally, by optimizing all parameters of both rings, we were able to: (1) Avoid low-threshold stimulated Raman scattering, (2) achieve Soliton microcomb, and (3) realize high efficiency SHG at the targeted wavelength. In the chip under test, all parameters (soliton ring width:  $2.48 \mu\text{m}$ , soliton ring radius:  $60.7 \mu\text{m}$ , height variation:  $990\text{-}1005 \text{ nm}$ )

except the coupling gap between the two rings and the doubler microring width were fixed. The results are shown in Fig. 5.11 where SHG and broadband octave spanning comb can be observed simultaneously, furthermore, competing Raman processes were not seen in the comb power of the devices during fast wavelength scans. Currently, although soliton steps can be observed from the fast scans, it remains challenging to lock onto a one, thus only a preliminary result in Fig. 5.12 is shown where the data is taken from a soliton microring coupled to a doubler ring.

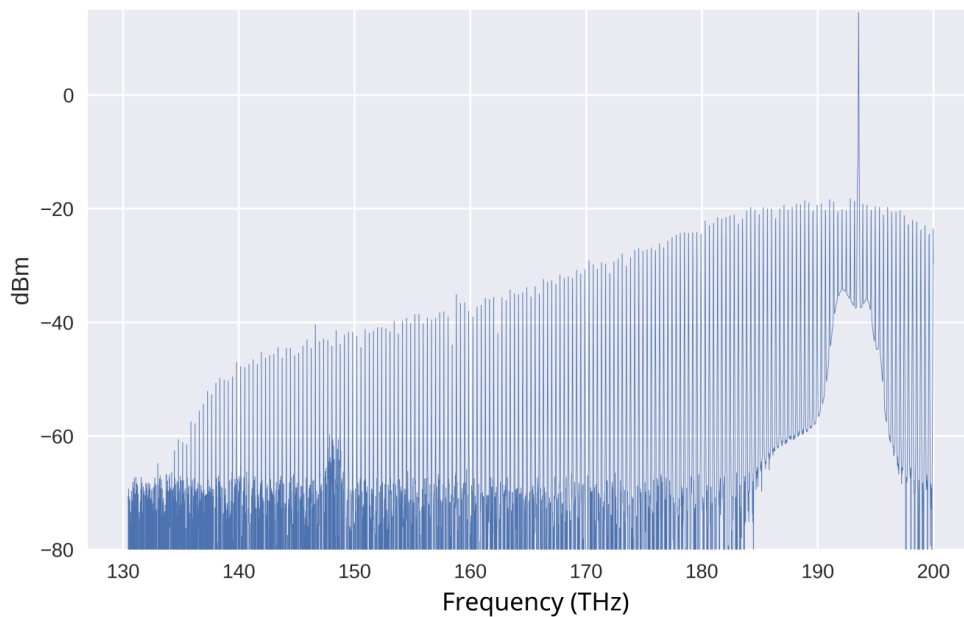


**Figure 5.12:** Observed soliton spectrum from a primary ring.

## References

- [1] X. Liu, Z. Gong, A. W. Bruch, J. B. Surya, J. Lu, and H. X. Tang, “Aluminum nitride nanophotonics for beyond-octave soliton microcomb generation and self-referencing,” *Nat. Commun.* **12**, 5428 (2021).
- [2] Z. Gong, A. Bruch, M. Shen, X. Guo, H. Jung, L. Fan, X. Liu, L. Zhang, J. Wang, J. Li, J. Yan, and H. X. Tang, “High-fidelity cavity soliton generation in crystalline AlN micro-ring resonators,” *Opt. Lett.* **43**, 4366 (2018).

- [3] Y. Sun, W. Shin, D. A. Laleyan, P. Wang, A. Pandey, X. Liu, Y. Wu, M. Soltani, and Z. Mi, “Ultra-high Q microring resonators using a single-crystal aluminum-nitride-on-sapphire platform,” *Opt. Lett.* **44**, 5679 (2019).
- [4] H. Weng, J. Liu, A. A. Afridi, J. Li, J. Dai, X. Ma, Y. Zhang, Q. Lu, J. F. Donegan, and W. Guo, “Directly accessing octave-spanning dissipative kerr soliton frequency combs in an AlN microresonator,” *Photonics Res.* **9**, 1351 (2021).
- [5] H. Weng, J. Liu, A. A. Afridi, J. Li, J. Dai, Y. Zhang, Q. Lu, J. F. Donegan, and W. Guo, “Perfect soliton crystal in an AlN microresonator,” in *Conference on Lasers and Electro-Optics* (OSA, Washington, D.C., 2021).
- [6] G. Moille, D. Westly, G. Simelgor, and K. Srinivasan, “Impact of the precursor gas ratio on dispersion engineering of broadband silicon nitride microresonator frequency combs,” *Opt. Lett.* **46**, 5970 (2021).
- [7] H. Zhou, Y. Geng, W. Cui, S.-W. Huang, Q. Zhou, K. Qiu, and C. Wei Wong, “Soliton bursts and deterministic dissipative kerr soliton generation in auxiliary-assisted microcavities,” *Light Sci. Appl.* **8**, 50 (2019).
- [8] W. Wang, L. Wang, and W. Zhang, “Advances in soliton microcomb generation,” *Adv. Photon.* **2**, 1 (2020).
- [9] D. C. Cole, A. Gatti, S. B. Papp, F. Prati, and L. Lugiato, “Theory of kerr frequency combs in fabry-perot resonators,” *Phys. Rev. A* **98**, 013831 (2018).
- [10] Y. K. Chembo and C. R. Menyuk, “Spatiotemporal lugiato-lefever formalism for kerr-comb generation in whispering-gallery-mode resonators,” *Phys. Rev. A* **87**, 053852 (2013).
- [11] T. Hansson and S. Wabnitz, “Dynamics of microresonator frequency comb generation: models and stability,” *Nanophotonics* **5**, 231 (2016).
- [12] G. Moille, Q. Li, X. Lu, and K. Srinivasan, “PyLLE: A fast and user friendly lugiato-lefever equation solver,” *J. Res. Natl. Inst. Stand. Technol.* **124**, 1 (2019).
- [13] Z. Gong, M. Li, X. Liu, Y. Xu, J. Lu, A. Bruch, J. B. Surya, C. Zou, and H. X. Tang, “Photonic dissipation control for kerr soliton generation in strongly raman-active media,” *Phys. Rev. Lett.* **125**, 183901 (2020).
- [14] X. Lu, G. Moille, A. Rao, D. A. Westly, and K. Srinivasan, “Efficient photoinduced second-harmonic generation in silicon nitride photonics,” *Nat. Photonics* **15**, 131 (2021).
- [15] E. Timurdogan, C. V. Poulton, M. J. Byrd, and M. R. Watts, “Electric field-induced second-order nonlinear optical effects in silicon waveguides,” *Nat. Photonics* **11**, 200 (2017).

- [16] W. H. P. Pernice, C. Xiong, C. Schuck, and H. X. Tang, “Second harmonic generation in phase matched aluminum nitride waveguides and micro-ring resonators,” *Appl. Phys. Lett.* **100**, 223501 (2012).

# Chapter 6

## Summary and outlook

As a summary of the work presented throughout this thesis, we have shown our attempts to systematically develop a fully integrated on-chip system for the generation of a compact and stable soliton microcomb. The main challenges of such a task are: (1) integrated and optimal SHG at a specific wavelength, (2) simultaneous efficient comb generation and SHG, (3) mitigation or stabilization of processes that disrupt or interfere with the soliton microcomb processes and cause instability, and finally (4) the integration of all components related to soliton microcomb generation and carrier envelope offset frequency detection as well as stabilization. The first challenge was addressed by chapter 2, where we presented a systematic procedure for optimizing SHG at any specific wavelength<sup>1</sup>. The second challenge was addressed by exploring a hybrid silicon nitride on aluminum nitride platform<sup>2</sup>. This platform takes advantage of the mature comb technologies in silicon nitride as well as the efficient second harmonic generation processes that have been developed for aluminum nitride. We presented a solution to the third challenge in chapter 4, where a method of stabilizing a photorefractive and thermal refractive system using an auxiliary laser was presented<sup>3</sup>. The versatility of this solution was also demonstrated by finely tuning a second harmonic generation peak across a range of wavelengths

with picometer-level precision. The fourth challenge of integration was addressed by using a novel coupled resonator system where one ring is designated for soliton microcomb generation and the other for efficient second harmonic generation. It was shown that this scheme is much more tolerant of frequency mismatches between the fundamental and SH modes which should be highly appreciated by applications of targeted SHG and of  $f_{ceo}$  detection. Finally, preliminary results showing soliton microcomb spectrum output from such a coupled ring resonator device was presented.

The outlook of this work is promising. Since it has already been shown by this work that soliton microcomb generation using a coupled ring resonator system on AlN is possible, the remaining task is to optimize a device for an octave spanning soliton microcomb. Along with an efficient doubler, such a device can be used to achieve the original goal of this thesis, which is to develop the first integrated, on-chip, compact and stable soliton microcomb.

## References

- [1] J. B. Surya, X. Guo, C.-L. Zou, and H. X. Tang, “Control of second-harmonic generation in doubly resonant aluminum nitride microrings to address a rubidium two-photon clock transition,” *Opt. Lett.* **43**, 2696 (2018).
- [2] J. B. Surya, X. Guo, C.-L. Zou, and H. X. Tang, “Efficient third-harmonic generation in composite aluminum nitride/silicon nitride microrings,” *Optica* **5**, 103 (2018).
- [3] J. B. Surya, J. Lu, Y. Xu, and H. X. Tang, “Stable tuning of photorefractive microcavities using an auxiliary laser,” *Opt. Lett.* **46**, 328 (2021).



# Appendix A

## Microring Resonator Design and Fabrication

### A.1 Microring Resonators

A particularly important component of a nonlinear integrated photonic circuit is the microring resonator. Its primary benefit is the ease of fabrication compared to other types of microresonators. Its properties such as dispersion, free spectral range and coupling can also be customized for the specific application as we shall see. In this chapter, a description and derivation of the important properties that guide the behavior of light inside a microring resonator is presented. The topics described here are not exhaustive and are chosen based on what will become useful for quantitative and qualitative analyses in chapters 3-7. For more detailed explanations, there are a number of other useful resources<sup>1-4</sup>.

#### A.1.1 Waveguide Coupling

The analysis of a microring resonator typically starts with the description of the coupling conditions into and out of the resonator. The input-output relations of electric field passing through the coupling region of a ring resonator with a single bus waveguide

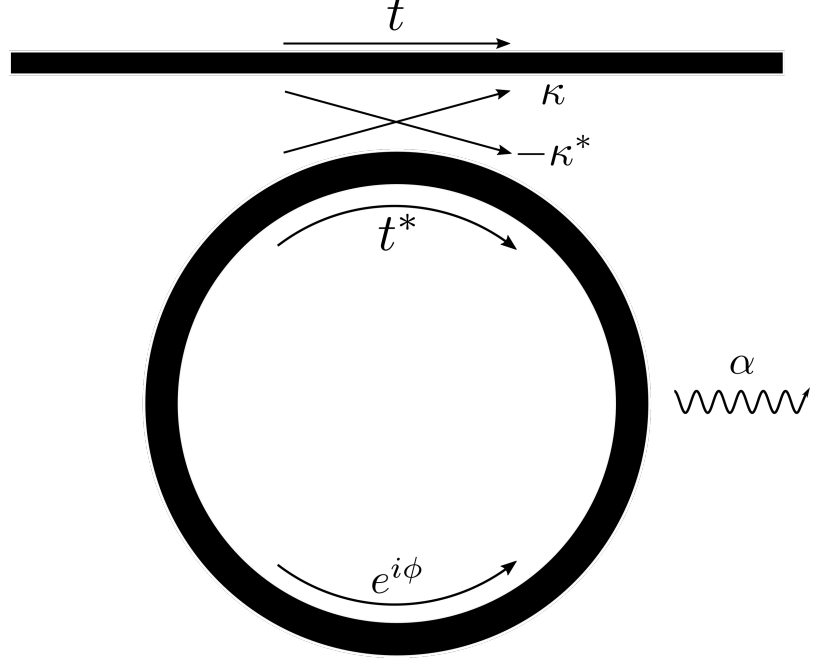


**Figure A.1: Conceptual illustration of a microring resonator.** Coupling terms ( $t, \kappa$ ), loss ( $\alpha$ ) and phase accumulation ( $e^{i\phi}$ ) experienced by the input field in a single round-trip are depicted.

(Fig. A.1) can be described by the following equation,

$$\begin{pmatrix} E_{t1} \\ E_{t2} \end{pmatrix} = \begin{pmatrix} t & \kappa \\ -\kappa^* & t \end{pmatrix} \begin{pmatrix} E_{i1} \\ E_{i2} \end{pmatrix} \quad (\text{A.1})$$

where the transfer matrix corresponding to the coupling region between the bus-waveguide and the microring obeys reciprocity and time reversal symmetry. Here,  $E_{i(t)1}$  represents the incoming (outgoing) electric field in the bus-waveguide at the coupling region, and  $E_{i(t)2}$  denotes the incoming (outgoing) electric field in the ring. In this simplified model, we assume no loss from the coupling, and that energy conservation requires the transfer matrix to be a unitary operation on the input field. Furthermore, by solving for  $E_{t1}$  and  $E_{t2}$  in terms of  $E_{i1}$ , we can obtain useful information on the effect of a microring resonator on

incoming light, as described here

$$\begin{aligned}
E_{t1} &= tE_{i1} - \kappa^* \kappa \alpha e^{i\phi} E_{i1} - \kappa^* \kappa \alpha e^{i\phi} \alpha t^* e^{i\phi} E_{i1} - \kappa^* \kappa \alpha e^{i\phi} (\alpha t^* e^{i\phi})^2 E_{i1} \dots \\
&= tE_{i1} - \kappa^* \kappa \alpha e^{i\phi} \left( 1 + \alpha t^* e^{i\phi} + (\alpha t^* e^{i\phi})^2 + (\alpha t^* e^{i\phi})^3 + \dots \right) E_{i1} \quad (\text{A.2}) \\
&= \left( t + \frac{-\kappa^* \kappa \alpha e^{i\phi}}{1 - \alpha t^* e^{i\phi}} \right) E_{i1} = \frac{t - \alpha e^{i\phi}}{1 - t^* \alpha e^{i\phi}} E_{i1}
\end{aligned}$$

$$\begin{aligned}
E_{t2} &= -\kappa^* E_{i1} - \kappa^* t^* \alpha e^{i\phi} E_{i1} - \kappa^* (t^* \alpha e^{i\phi})^2 E_{i1} - \kappa^* (t^* \alpha e^{i\phi})^3 E_{i1} \dots \\
&= -\kappa^* \left( 1 + t^* \alpha e^{i\phi} + (t^* \alpha e^{i\phi})^2 + (t^* \alpha e^{i\phi})^3 + \dots \right) E_{i1} \quad (\text{A.3}) \\
&= \frac{-\kappa^*}{1 - t^* \alpha e^{i\phi}} E_{i1}
\end{aligned}$$

Calculating for the normalized power within the resonator and at the output end of the bus-waveguide, we reach the following equations,

$$\left| \frac{E_{t1}}{E_{i1}} \right|^2 = \frac{|t|^2 + \alpha^2 - 2\alpha t \cos(\phi)}{1 + \alpha^2 |t|^2 - 2\alpha t \cos(\phi)} \quad (\text{A.4})$$

$$\left| \frac{E_{t2}}{E_{i1}} \right|^2 = \frac{|\kappa|^2}{1 + \alpha^2 |t|^2 - 2\alpha t \cos(\phi)} \quad (\text{A.5})$$

where we see that when  $\phi$  is equal to an integer multiple of  $2\pi$ , the power circulating the resonator is at a maximum, and conversely the power transmitted at the bus-waveguide is minimized. At resonance, the accumulated phase in a single round trip corresponds to,

$$\phi = 2\pi m = 2\pi \frac{L}{\lambda} \quad (\text{A.6})$$

where  $L = 2\pi R$ , and  $m$  denotes all integers greater than 0. In later sections it will be shown that the above equations are useful for intuitive understanding of how microring cavities amplify input power.

## A.1.2 Dispersion and the Free Spectral Range

Dispersion is the phenomenon where different wavelengths or frequencies of light will travel at different velocities through a medium. The bulk index of refraction of a material varies with the wavelength of light, where typically the index of a material is modeled by the Sellmeier equation. In a microring resonator, dispersion is usually described by the effective index and this comes in three different varieties. The first is geometric dispersion, where by changing the cross-sectional geometry or radius of curvature of the ring will subsequently alter the effective index. The second is material dispersion, where different materials follow different effective index curves. Finally there is modal dispersion, where eigenmodes of the ring will experience distinctive effective indices.

A particularly important feature of the microring resonator is the free spectral range (FSR), which is the frequency or wavelength spacing between resonances. Using the resonance condition described by Eq. A.6, we can derive the FSR of a microring resonator. In the simplest approximation, where we assume that the effective index  $n_{\text{eff}}$  is constant in the vicinity of  $\lambda$ , the resonance condition reads,

$$m = \frac{2\pi n_{\text{eff}} R}{\lambda} \quad (\text{A.7})$$

where the FSR is simply,

$$\left| \frac{\partial m}{\partial \lambda} \right|^{-1} = \frac{\lambda^2}{2\pi n_{\text{eff}} R} \quad (\text{A.8})$$

Often due to the geometry of the microring which causes large dispersion, the approximation that  $n_{\text{eff}}$  is constant in the vicinity of  $\lambda$  does not hold. Thus the equation of FSR becomes,

$$\left| \frac{\partial m}{\partial \lambda} \right|^{-1} = \left( 2\pi R \left| \frac{\partial (n_{\text{eff}}(\lambda) \lambda^{-1})}{\partial \lambda} \right| \right)^{-1} = \frac{\lambda^2}{2\pi R \left| \lambda \frac{\partial n_{\text{eff}}}{\partial \lambda} - n_{\text{eff}} \right|} = \frac{\lambda^2}{L n_g} \quad (\text{A.9})$$

where  $n_g = n_{eff} - \lambda \frac{\partial n_{eff}}{\partial \lambda}$  is known as the group index, and  $L$  is the round-trip length of the cavity.

In frequency ( $f$ ) domain the corresponding FSR becomes,

$$\left| \frac{\partial m}{\partial f} \right|^{-1} = \left( \frac{L}{c} \left( n(f) + f \frac{\partial n(f)}{\partial f} \right) \right)^{-1} = \frac{c}{Ln_g} \quad (\text{A.10})$$

here  $c$  denotes the speed of light in vacuum.

Part of the appeal of using microring resonators is the relative ease of the customization of the dispersion and subsequently the FSR. This is largely due to the fact that the dispersion is highly sensitive to the geometry. Particularly in the field of comb generation, the degrees of freedom allowed in the geometrical design of the microring is highly desirable for designing resonators that produce broadband combs.

### A.1.3 Quality Factor and Finesse

In this subsection, we shall dive into properties of the microring resonator that are frequently used to gauge its "quality". Generally speaking, we wish to create a resonator that can amplify input light to as high power as possible. This then requires the loss  $\alpha$  of the resonator to be as low as possible. The specific quantities we use to measure this are the quality factor, and the finesse of the resonator.

There are two main definitions of the quality (Q) factor. The first, which is the one used in this thesis, is the bandwidth definition which is the ratio of the frequency (wavelength) to the frequency (wavelength) full width at half maximum (FWHM) of the resonance. The second definition is the ratio of the energy stored in the resonator to the energy dissipated per cycle. These two definitions are approximately equal when the Q factor is large and it

can be written as,

$$Q \equiv \frac{\omega}{\text{FWHM}} = \frac{\omega}{2\Delta\omega} \quad (\text{A.11})$$

We further define the loaded-Q factor ( $Q_l$ ) as the Q factor that takes into account all loss mechanisms of the resonator. Generally there are two types of loss mechanisms. The first is loss due to coupling, such as to the bus-waveguide (corresponding to  $Q_c$ ). The second is intrinsic loss, like scattering and material absorption (corresponding to  $Q_i$ ). We further note that a system like the one in Fig. A.1 can operate under three different coupling regimes: (1) The resonator is said to be critically coupled ( $Q_c = Q_i$ ), when the intrinsic loss rate and the coupling rate are equal. In this regime, the intracavity power is at a maximum and the transmitted power is minimized, theoretically to zero. (2) In the over-coupled regime ( $Q_c < Q_i$ ), coupling into the resonator is greater than the intrinsic loss rate. In this regime, the linewidth of the resonance is broadened and the extinction ratio (defined as the peak of the resonance divided by the base) is lowered. (3) In the under-coupled regime ( $Q_c > Q_i$ ), the bandwidth of the resonance becomes narrower and closer in value to the intrinsic linewidth (due to intrinsic losses of the resonator). Its extinction ratio is lowered compared to when the resonator is critically coupled.

Another important quantity is the finesse ( $F$ ) of the cavity, which is defined as,

$$F \equiv \frac{\text{FSR}}{\text{FWHM}} = \frac{c}{2n_g L \Delta f} \quad (\text{A.12})$$

For the system described by Fig. A.1, it is helpful to derive the FWHM in order to gain an intuitive understanding of the finesse at critical coupling. Beginning with the expression for  $E_{t2}$  in Eq. A.5, we wish to find the value of  $\phi$  which would correspond to half the power at resonance. Furthermore, the assumption that the coupling does not induce any loss means that the coupling coefficients are real values. The equation we wish

to solve is then,

$$\frac{1}{2} \left| \frac{E_{t2}}{E_{i1}} \right|_{\max}^2 = \frac{1}{2} \left( \frac{\kappa^2}{1 + t^2 \alpha^2 - 2t\alpha} \right) = \frac{1}{2} \left( \frac{\kappa^2}{(1 - t\alpha)^2} \right) = \frac{\kappa^2}{1 + t^2 \alpha^2 - 2t\alpha \cos(\phi)} \quad (\text{A.13})$$

where if we isolate  $\cos(\phi)$ , we arrive at,

$$\cos(\phi) = \frac{-1 - t^2 \alpha^2 + 4t\alpha}{2t\alpha} \quad (\text{A.14})$$

If we assume a high quality factor, we can Taylor expand  $\cos(\phi)$  around 0. Taking the first non-vanishing term and evaluating at critical coupling ( $t = \alpha$ ), we can simplify the equation to,

$$\phi \approx \frac{1 - t^2}{t} \quad (\text{A.15})$$

and finally, we arrive at the equation for the FWHM,

$$\text{FWHM} = 2\Delta f = \frac{c(1 - t^2)}{\pi n_{eff} R t} \quad (\text{A.16})$$

Since the finesse is simply the ratio of the FSR to the FWHM, we can express the finesse at critical coupling for the single resonator and bus-waveguide system as,

$$F \approx \frac{\pi}{1 - t^2} = \frac{\pi}{\kappa^2} \quad (\text{A.17})$$

If we relate this quantity to the maximum intracavity power ratio in Eq. A.5 at critical coupling, we find that

$$\left| \frac{E_{t2}}{E_{i1}} \right|_{\max}^2 \approx \frac{\kappa^2}{(1 - t^2)^2} = \frac{F}{\pi} \quad (\text{A.18})$$

which states that the ratio of finesse to  $\pi$  is a good estimator of the intracavity power enhancement at critical coupling and high Q.

## References

- [1] W. Bogaerts, P. De Heyn, T. Van Vaerenbergh, K. De Vos, S. Kumar Selvaraja, T. Claes, P. Dumon, P. Bienstman, D. Van Thourhout, and R. Baets, “Silicon microring resonators,” *Laser Photon. Rev.* **6**, 47 (2012).
- [2] C. Manolatou, M. J. Khan, S. Fan, P. R. Villeneuve, H. A. Haus, and J. D. Joannopoulos, “Coupling of modes analysis of resonant channel add-drop filters,” *IEEE J. Quantum Electron.* **35**, 1322 (1999).
- [3] in *Integrated Ring Resonators* (Springer Berlin Heidelberg, Berlin, Heidelberg, 2007) pp. 3–40.
- [4] A. Yariv and P. Yeh, in *Photonics*, 6th ed., The Oxford Series in Electrical and Computer Engineering (Oxford University Press, New York, NY, 2006).



# Appendix B

## Frequency Comb Simulation Source Code

### B.1 Main Code

```
1 from comb_utils_cy_pyfile import *
2 import argparse
3
4 if __name__ == '__main__':
5     parser = argparse.ArgumentParser()
6     # simulation parameters
7     parser.add_argument('-Nmodes', type=int, default=2**9,
8                         help='number of modes, use a power of 2 for faster simulation')
9     parser.add_argument('-total_time', type=float, default=1e-6,
10                        help='total time for simulation in seconds, default 1e-6')
11    parser.add_argument('-dt', type=float, default=1e-3/4,
12                       help='normalized time step (normalized to total loss rate), \
13                           default 1e-3/2')
14    parser.add_argument('-snapshots', type=int, default=2000,
15                       help='number of snapshots of the comb solution, default 2000')
16    parser.add_argument('-mode_offset', type=int, default=0,
17                       help='offset of modes in relation to central pump frequency, \
18                           this is used for flexibility when Dint curve does not \
19                           fully fit in range of modes')
20    parser.add_argument('-filename', type=str, default='combsol',
21                       help="file name for comb solution, default is 'combsol', \
22                           do not include any suffix (e.g., .csv)")
23    parser.add_argument('-save', type=int, default=1,
24                       help='indicate if you want to save the comb solution (1 or 0), \
25                           default is 1 (yes)')
```

```

26 parser.add_argument('-threads',type=int,default=1,
27     help='indicate the number of threads you want to \
28     utilize for FFTs, default is 1')
29 parser.add_argument('-plan_fft',type=int,default=1,
30     help='indicate whether you want to use pyfftw, \
31     this should be 1 for faster simulation')
32 parser.add_argument('-fastmath',type=bool,default=False,
33     help='indicate whether you want to use fastmath in numba, \
34     this sacrifices a bit in accuracy for speed')
35
36 # ring parameters
37 parser.add_argument('-radius',type=float,default=60e-6,
38     help='radius in meters')
39 parser.add_argument('-height',type=float,default=1e-6,
40     help='height of cross section in meters')
41 parser.add_argument('-width',type=float,default=2.5e-6,
42     help='width of cross section in meters')
43 parser.add_argument('-ng',type=float,default=2.2,
44     help='group velocity index, default 2.2')
45 parser.add_argument('-Qc',type=float,default=1.5e6,
46     help='coupling Q, default 1e6')
47 parser.add_argument('-Qi',type=float,default=1.5e6,
48     help='intrinsic Q, default 1e6')
49 parser.add_argument('-n2',type=float,default=2.4e-19,
50     help='kerr nonlinear index, default 2.4e-19')
51 parser.add_argument('-Dint_file',type=str,default='2.500w_58.5r_0.945h.csv',
52     help='Dint file, needs to have specific format')
53 parser.add_argument('-Dint_degrees',type=int,default=9,
54     help='Degrees to fit the Dint polynomial, default 9')
55
56 # pump laser parameters
57 parser.add_argument('-detuning_range', nargs=2, type=int, default=[-8,15],
58     help='detuning range, default [-8,20]')
59 parser.add_argument('-frequency_range', nargs=2, type=int, default=[],
60     help='frequency range, default [], use this to replace detuning range')
61 parser.add_argument('-wavelength_range', nargs=2, type=int, default=[],
62     help='wavelength range, default [], use this to replace detuning range,\
63     prioritizes wavelength -> frequency -> detuning range')
64 parser.add_argument('-pump_frequency',type=float,default=299792458/1.550e-6,
65     help='frequency in Hz, default to 1550nm in frequency')
66 parser.add_argument('-pump_wavelength',type=float,default=None,
67     help='pump wavelength in meters, default is None, \
68     set this to replace pump frequency')
69 parser.add_argument('-frequency_sweep_speed',type=float,default=None,
70     help='set laser sweep speed in Hz/sec, default None')
71 parser.add_argument('-wavelength_sweep_speed',type=float,default=None,
72     help='set laser sweep speed in nm/sec, default None')
73 parser.add_argument('-pump_power',type=float,default=250e-3,
74     help='set laser pump power in watts, default 200e-3')
75
76 args = parser.parse_args()
77
78 aln_ring = microring(R=args.radius,height=args.height,width=args.width,
79     ng=args.ng,Qc=args.Qc,Qi=args.Qi,n2=args.n2,
80     _dnorm_range=args.detuning_range,_w_range=args.frequency_range,

```

```

81     _l_range=args.wavelength_range,_w0=args.pump_frequency,
82     _l0=args.pump_wavelength,total_time=args.total_time,
83     _w_sweep_speed=args.frequency_sweep_speed,
84     _l_sweep_speed=args.wavelength_sweep_speed,
85     Qc_import=10*np.linspace(5.1,7.1,args.Nmodes),
86     Qc_file='coupling_q_1.csv',Dint_file=args.Dint_file,dt=args.dt,
87     Nmodes=args.Nmodes,pump=args.pump_power,
88     snapshots=args.snapshots,mode_offset=args.mode_offset,
89     Dint_degrees=args.Dint_degrees,save=args.save,filename=args.filename)
90
91     value = input("start simulation? y or n:\n")
92     value2 = 'continue'
93     idx = None
94
95     if (value == 'y') or (value == 'yes'):
96         aln_ring.split_step(plan_fft=args.plan_fft,
97                             threads=args.threads,fastmath=args.fastmath)
98
99         while not (value2 == 'y' or value2 == 'yes'):
100             if idx:
101                 aln_ring.plot_all(int(idx))
102             else:
103                 aln_ring.plot_all()
104             value2 = input("quit simulation? y or n:\n")
105             if (value2 == 'y' or value2 == 'yes'):
106                 break
107             idx = input('new index for plotting:\n')
108
109     else:
110         print('\nsimulation stopped')

```

## B.2 Comb Solver

```

1  import pandas as pd
2  import glob
3  import os
4  from matplotlib import pyplot as plt
5  import pandas as pd
6  import numpy as np
7  from scipy import signal
8  import pdb
9  import time
10 import calendar
11 import pyfftw
12 import pickle
13 from tqdm import tqdm
14 from numba import jit
15 from comb_utils_cython import *

```

```

16
17 # utility functions
18
19 def save_obj(obj,name):
20     with open(os.getcwd() + '/' + name + '.pkl', 'wb') as f:
21         pickle.dump(obj, f, pickle.HIGHEST_PROTOCOL)
22
23 def load_obj(name):
24     with open(os.getcwd() + '/' + name + '.pkl', 'rb') as f:
25         return pickle.load(f)
26
27 def save_params(obj,name):
28     idx = 1
29     file_list = [os.path.basename(x) for x in glob.glob(os.getcwd()+'/.*')]
30     new_filename = name
31     while new_filename+'.csv' in file_list:
32         new_filename = name + '_' + f'{idx:03}'
33         idx += 1
34     save_obj(obj,new_filename)
35
36
37 # note that _w is in units of Hz, not radians/sec
38
39 class microring:
40
41     def __init__(self,R=60e-6,height=1e-6,width=2.3e-6,ng=2.2,
42                 Qc=1e6,Qi=1e6,n2=2.4e-19,_dnorm_range=[-8,12],_w_range=[],_l_range=[],
43                 _w0=299792458/1.550e-6,_l0=None,total_time=10e-6,_w_sweep_speed=None,
44                 _l_sweep_speed=None,Qc_import=None,Qc_file=None,Dint_file=None,dt=1e-3/2,
45                 Nmodes=2**8,pump=200e-3,snapshots=2000,mode_offset=0,Dint_degrees=9,
46                 save=True,filename='combsol',set_Dint=None,seed=None,aux=None):
47         # set constants
48         self.constants()
49
50         # set ring parameters
51         self.ring_parameters(R,height,width,ng,Nmodes,Qi,mode_offset,aux)
52
53         if Qc_import is not None:
54             self.Qc = Qc_import
55             self.Ql = (1/self.Qc[len(Qc_import)//2]+1/Qi)**-1
56         else:
57             self.Qc = Qc
58             self.Ql = (1/Qc+1/Qi)**-1
59             self._d_wext = _w0/self.Qc # 25e6 # single value
60
61         # laser parameters (_w is in Hz units)
62         if _l0:
63             self._l0 = _l0
64             self._w0 = self.c/_l0
65         else:
66             self._w0 = _w0
67             self._l0 = self.c/self._w0
68
69         # linewidth of resonance useful for normalization
70         self._d_wtot = self._w0/self.Ql # total coupling rate at pump frequency

```

```

71     self._d_wi = self._w0/self.Qi
72
73     if _w_range or _l_range:
74         try:
75             self._l_start = _l_range[0]
76             self._l_end = _l_range[1]
77             self._w_start = self.c/_l_start
78             self._w_end = self.c/_l_end
79         except:
80             self._w_start = _w_range[0]
81             self._w_end = _w_range[1]
82             self._l_start = self.c/self._w_start
83             self._l_end = self.c/self._w_end
84             self._dnorm_range = [(self._w0-self._w_start)/(self._d_wtot/2),
85                                 (self._w0-self._w_end)/(self._d_wtot/2)]
86         else:
87             self._dnorm_range = _dnorm_range # normalized detuning array
88             # (normalized in terms of half linewidths)
89             self._w_start = self._w0 - self._dnorm_range[0]*(self._d_wtot/2)
90             self._w_end = self._w0 - self._dnorm_range[1]*(self._d_wtot/2)
91             self._l_start = self.c/self._w_start
92             self._l_end = self.c/self._w_end
93
94     print(f'_w_start = {self._w_start/1e12} THz, _w_end = {self._w_end/1e12}\
95           THz')
96     print(f'_l_start = {self._l_start*1e9} nm, _l_end = {self._l_end*1e9} nm')
97     print(f'normalized detunings = [ {self._dnorm_range[0]} , \
98           {self._dnorm_range[1]} ] (relevant parameters: _dnorm_range)')
99
100    if total_time and (_w_sweep_speed is None) and (_l_sweep_speed is None):
101        self.total_time = total_time
102        self._w_sweep_speed = np.abs(self._w_end-self._w_start)/total_time
103        self._l_sweep_speed = np.abs(self._l_end-self._l_start)/total_time
104        print(f'sweep speed (_w space) = {self._w_sweep_speed/1e9} GHz/s\
105              \nsweep speed (_l space) = {self._l_sweep_speed*1e9} nm/s')
106    elif _w_sweep_speed:
107        self._w_sweep_speed = _w_sweep_speed
108        self.total_time = np.abs(self._w_end-self._w_start)\
109              /self._w_sweep_speed
110        print(f'total time = {self.total_time}')
111    elif _l_sweep_speed:
112        self._l_sweep_speed = _l_sweep_speed
113        self.total_time = np.abs(self._l_end-self._l_start)\
114              /self._l_sweep_speed
115        print(f'total time = {self.total_time}')
116    else:
117        print('no sweep speed or total time given (relevant \
118              parameters: _l_sweep_speed, _w_sweep_speed, total_time)')
119
120    self.Tnorm = self.total_time*self._d_wtot/2
121    self.dt=dt/(pump/0.003) # normalized dt, dt is not in units of seconds
122    print(f"real time = {self.total_time}, normalized time = \
123          {self.Tnorm} (relevant parameters: total_time), dt = {dt}")
124    self.Nsim = self.Tnorm//self.dt
125

```

```

126 print(f'Simulation points = {self.Nsim} (relevant parameters: dt)')
127
128 self._darr = np.linspace(self._w0-self._w_start,self._w0\
129 -self._w_end,int(self.Nsim)) # replaced last term with int(self.Nsim)
130 print(f'detuning at start = {self._darr[0]/1e9} GHz, \
131       detuning at end = {self._darr[-1]/1e9} GHz (relevant parameters: \
132       _w_range, _l_range)')
133
134 self.idx = Nmodes//2-mode_offset
135 self.mode_arr = np.arange(-Nmodes/2+mode_offset,Nmodes/2+mode_offset)
136 self._mu_ = self.fftshift(self.mode_arr,self.idx)
137 self._warr = self.mode_arr*self.FSR+self._w0
138
139 if Qc_import is not None:
140     self._d_wext = self._warr/self.Qc
141     self._d_wext_arr = self._d_wext
142
143 # find coefficients for Dint if a file is given, if not, use the default.
144 # The file has to have two columns with name 'lambda' and 'Dint'
145 if Qc_file:
146     df_Qc = pd.read_csv(Qc_file)
147     self.Qc_co coeffs = np.polyfit(3e2/df_Qc['lambda'],df_Qc['Qc'],deg=9)
148     self.Qc = self.PolyCoefficients(self._warr/1e12,self.Qc_co coeffs)
149     print(Qc/1e6)
150     self._d_wext = self._warr/self.Qc
151     self._d_wext_arr = self._d_wext
152
153 if Dint_file:
154     df = pd.read_csv(Dint_file)
155     df['lambda']=3e2/df['lambda']
156     self.Dint_co coeffs = np.polyfit(df['lambda'],df['Dint'],deg=Dint_degrees)
157 else:
158     self.Dint_co coeffs = np.array([ 7.38392840e-07, -1.08366836e-03,
159     6.20323154e-01, -1.52824970e+02, 2.00631574e+01,
160     9.25526200e+06, -2.25798494e+09, 2.33413386e+11, -9.25346061e+12])
161 if set_Dint is not None:
162     self.Dint_arr = set_Dint
163     self._warr_adjusted = self._warr+self.Dint_arr
164     self.Dint_arr = self.fftshift(self.Dint_arr,self.idx)
165 else:
166     self.Dint_arr = self.PolyCoefficients(self._warr/1e12,self.Dint_co coeffs)
167     self.Dint_arr = self.fftshift(self.Dint_arr,self.idx)
168     self.Dint_arr -= self.Dint_arr[0]
169     self._warr_adjusted = self._warr+self.ifftshift(self.Dint_arr,self.idx)
170 self.n2 = n2 # m^2 / W
171 self.Veff = self.A*self.L
172 self.g0 = self.h*self._w0**2*self.c*self.n2/self.ng**2/self.Veff
173 # nonlinear gain (approximation since _w0 should represent laser wavelength)
174 # note that g0 has units of Hz.
175 self._gamma_ = self.n2*self._w0/self.c/self.A
176
177 # set vacuum noise fluctuations that will initiate the comb
178 self.normalization = np.sqrt(self.g0*2/self._d_wtot)
179 self.noise_norm = self.set_noise(seed=seed)
180 self.pump = pump

```

```

181 self.Nsnapshots = snapshots
182 self._d_snapshots = np.linspace(self._dnorm_range[0],
183     self._dnorm_range[1], self.Nsnapshots)
184 self.sol = np.ndarray(shape=(self.Nsnapshots, self.Nmodes), dtype='complex')
185 self.F_arr = np.zeros(self.Nmodes, dtype='complex')
186
187 try: # temporary solution for coupling Q array
188     self.F_arr[0] = np.sqrt(8*self.g0*self.fftshift(
189         self._d_wext_arr, self.idx)[0]*self.pump/(self.h*self._w0)\
190         /self._d_wtot**3) # normalized power coupled into waveguide
191     self._d_wext = self.fftshift(self._d_wext_arr, self.idx)
192     print(f"normalized external coupling rate at pump = \
193         {self.fftshift(self._d_wext_arr/(self._w0/1e6), self.idx)[0]}")
194 except Exception as e: # temporary solution for coupling Q single value
195     self.F_arr[0] = np.sqrt(8*self.g0*self._d_wext*self.pump\
196         /(self.h*self._w0)/self._d_wtot**3)
197
198 print(f'g0 = {self.g0}, Veff = {self.Veff}, \
199     F^2 = {np.abs(self.F_arr[0])**2}')
200 self.norm_factor = np.sqrt(2*self.g0/self._d_wtot)
201 self.sol[0, :]=self.noise_norm
202
203 if Qc_file is None and Qc_import is None:
204     self.plot_Dint()
205 else:
206     self.plot_Dint_Qc()
207
208
209 self.save = save
210 self.filename = filename
211 if '.csv' in self.filename:
212     raise Exception("do not include '.csv' or suffix in filename")
213
214 def PolyCoefficients(self, x, coeffs):
215     """ Returns a polynomial for ``x`` values for the ``coeffs`` provided.
216
217     The coefficients must be in ascending order (``x**0`` to ``x**o``).
218     """
219     o = len(coeffs)
220     print(f'polynomial of order {o-1}.')
221     y = 0
222     coeffs = coeffs[::-1]
223     for i in range(o):
224         y += coeffs[i]*x**i
225     return y
226
227 def set_noise(self, seed):
228     if seed:
229         np.random.seed(seed=seed)
230     energy = self.h*(self.fftshift(self._warr_adjusted, self.idx))
231     phase_noise = 2*np.pi*np.random.rand(self.Nmodes)
232     arr = np.random.rand(self.Nmodes)
233     normalized_noise = self.normalization*arr*np.sqrt(energy/2)\
234         *np.exp(1j*phase_noise)*self.Nmodes
235     return normalized_noise

```

```

236
237
238 def split_step(self, plan_fft=False, threads=1, wisdom=None, fastmath=False):
239     """split step method, initial seed starts off in the frequency domain,
240     note that due to the randomness of the seed noise, the solutions
241     may not be the same even when run multiple times with the
242     same parameters"""
243     with tqdm(total=self.Nsnapshots) as pbar:
244         divbysnapshot = self.Nsim//self.Nsnapshots
245         sol_track = 0
246         _psi_f = self.sol[0,:]
247         F_arr = np.fft.ifft(self.F_arr)*(self.Nmodes)
248         _psi_f += self.F_arr*self.Nmodes*self.dt
249
250         #####
251         # convert to local variables
252         dt = np.complex128(self.dt)
253         Dint_arr = np.complex128(self.Dint_arr)
254         noise_norm = self.noise_norm
255         _d_wext = np.complex128(self._d_wext)
256         _d_wi = np.complex128(self._d_wi)
257         _d_wtot = np.complex128(self._d_wtot)
258         _darr = np.complex128(self._darr)
259         Nsim = self.Nsim
260         #####
261
262         '''Plan ifft/fft, pre-allocate resources, this will speed up
263     the FFT quite a bit compared to regular np.fft
264     note that the bottleneck is usually the array assignments and
265     dispersion calculations within the loop, not the fft'''
266         # frequency domain
267         ifft_arr = pyfftw.empty_aligned(self.Nmodes, dtype='complex128', n=16)
268         # time domain
269         fft_arr = pyfftw.empty_aligned(self.Nmodes, dtype='complex128', n=16)
270         fft_object = pyfftw.FFTW(fft_arr, ifft_arr, threads=threads,
271             flags=('FFTW_MEASURE',))
272         ifft_object = pyfftw.FFTW(ifft_arr, fft_arr, direction='FFTW_BACKWARD',
273             threads=threads, flags=('FFTW_MEASURE',))
274         ifft_arr[:] = _psi_f
275         # some additional ways of using pyfftw builders to initialize
276         # fft arrays in memory
277         # sometimes overhead of setting up additional threads is not worth it
278         # ifft_object = pyfftw.builders.ifft(ifft_arr, threads=1)
279         # Plan fft
280         # fft_object = pyfftw.builders.fft(fft_arr, threads=1)
281
282         if wisdom:
283             pyfftw.import_wisdom(wisdom)
284
285         if plan_fft:
286             dwext = _d_wext
287             dwi = _d_wi
288             dwtot = _d_wtot
289             Dint_arr = Dint_arr
290             detuning = _darr

```



```

291     F_arr = np.complex128(F_arr)
292     self.sol = split_step_cython(Nsim,dt,dwext,dwi,dwtot,Dint_arr,
293     detuning,F_arr,self.Nmodes,noise_norm,divbysnapshot,
294     self.Nsnapshots,pbar,ifft_object,fft_object,ifft_arr,fft_arr)
295
296     else: # this is without optimization to compare, using the optimized
297     # version usually gives a >30% speedup
298
299     for i in range(int(Nsim)):
300         _psi_f = np.exp(-(dt/2) * ((_d_wext+_d_wi)/_d_wtot+1j)\
301         * (Dint_arr + _darr[i])*2/_d_wtot )) * _psi_f
302         _psi_t = np.fft.ifft(_psi_f) # convert to time domain
303         _psi_f = np.fft.fft(np.exp(dt * (1j * np.abs(_psi_t) ** 2 \
304         + F_arr/_psi_t )) * _psi_t)
305         _psi_f = np.exp(-(dt/2) * ((_d_wext+_d_wi)/_d_wtot+1j)\
306         * (Dint_arr + _darr[i])*2/_d_wtot )) * _psi_f
307         _psi_f += noise_norm
308         if (not ((i+1)%divbysnapshot)) and sol_track<self.Nsnapshots:
309             self.sol[sol_track,:] = _psi_f
310             sol_track += 1
311             pbar.update(1)
312
313     if plan_fft:
314         """import wisdom from previous simulations to save time on
315         FFT planning, this doesn't improve performance much
316         unless you do a lot of FFT planning and your FFT
317         array sizes are very large."""
318         self.wisdom = pyfftw.export_wisdom()
319
320     if self.save:
321         self.save_sol()
322     pass
323
324     def plot_intracavity_power(self):
325         plt.plot(self._d_snapshots,np.mean(np.abs(self.sol)**2\
326         *self.normalization**2,axis=1))
327         plt.show()
328
329     def plot_all(self,idx=None):
330         norm_factor = 1/(4*self.g0/(self._d_wtot**2*self.h*self._warr))/self.Nmodes
331         self.norm_factor = norm_factor
332         if not self.aux:
333             pump_arr = np.linspace(0,0,self.Nmodes,datatype='complex')
334             pump_arr[0] = self.pump
335             self.wg_sol = pump_arr - self.sol*np.sqrt(self.fftshift(norm_factor,
336             self.idx))*np.sqrt(self.t_roundtrip*self._d_wext)
337
338         if idx is None:
339             differences = (np.diff(np.sum(np.abs(self.sol[:])**2,axis=1)))
340             idx = np.where(differences>0)[0][np.argmin(
341             differences[np.where(differences>0)])]-100
342         fig, axs = plt.subplots(4,1,figsize=(10,13))
343         zeros_arr = np.linspace(0,0,self.Nmodes)
344         axs[0].plot(self._warr/1e12,self.ifftshift(self.Dint_arr,self.idx)/1e9)
345         axs[0].plot(self._warr/1e12,zeros_arr,'r-')

```

```

346     axs[0].set_xlabel('Frequency (THz)')
347     axs[0].set_ylabel('Dint (GHz)')
348
349     axs[1].plot(np.sum(np.abs(self.sol[:]*np.sqrt(norm_factor))**2,axis=1))
350     axs[1].plot(idx,np.sum(np.abs(self.sol[idx]*np.sqrt(norm_factor))**2),
351                 'r*',markersize=12)
352     axs[1].set_xlabel('snapshot #')
353     axs[1].set_ylabel('Intracavity power (W)')
354     axs[2].stem(self._warr/1e12,10*np.log10(np.abs(
355         self.ifftshift(self.sol[idx],self.idx)*np.sqrt(norm_factor))**2*1e3),
356              bottom=np.min(10*np.log10(np.abs(self.ifftshift(self.sol[idx],
357         self.idx)*np.sqrt(norm_factor))**2*1e3)),
358              markerfmt=' ',label='Intracavity')
359     if not self.aux:
360         axs[2].plot(self._warr/1e12,10*np.log10(np.abs(
361             self.ifftshift(self.wg_sol[idx],self.idx))**2*1e3),
362                 label='Waveguide')
363     axs[2].legend(loc='upper right')
364     axs[2].set_xlabel('Frequency (THz)')
365     axs[2].set_ylabel('Power (dBm)')
366     axs[3].plot(np.linspace(-np.pi,np.pi,self.Nmodes),
367              np.log10(np.abs(np.fft.ifft(self.sol[idx]))**2))
368     axs[3].set_xlabel('')
369     axs[3].set_ylabel('Log10($|\psi|^2$)')
370     fig.tight_layout()
371     plt.show()
372     return fig
373
374     def plot_Dint(self):
375         zeros_arr = np.linspace(0,0,self.Nmodes)
376         fig, ax = plt.subplots(1,1,figsize=(4,2))
377         ax.plot(self._warr/1e12,self.ifftshift(self.Dint_arr,self.idx)/1e9)
378         ax.plot(self._warr/1e12,zeros_arr,'r-')
379         ax.set_xlabel('Frequency (THz)')
380         ax.set_ylabel('Dint (GHz)')
381         fig.tight_layout()
382         plt.show()
383
384     def plot_Dint_Qc(self):
385         zeros_arr = np.linspace(0,0,self.Nmodes)
386         fig, ax = plt.subplots(1,2,figsize=(9,2))
387         ax[0].plot(self._warr/1e12,self.ifftshift(self.Dint_arr,self.idx)/1e9)
388         ax[0].plot(self._warr/1e12,zeros_arr,'r-')
389         ax[0].set_xlabel('Frequency (THz)')
390         ax[0].set_ylabel('Dint (GHz)')
391         ax[1].plot(self._warr/1e12,np.log10(self.Qc))
392         ax[1].set_xlabel('Frequency (THz)')
393         ax[1].set_ylabel('Qc (Log10)')
394         fig.tight_layout()
395         plt.show()
396
397     def fftshift(self,lst,idx):
398         # shifts the first 0 to idx terms all to the right side of
399         # the rest of the array
400         return np.concatenate((lst[idx:],lst[0:idx]))

```

```

401
402 def ifftshift(self, lst, idx):
403     # inverse of self.fftshift
404     return np.concatenate((lst[-idx:], lst[0:-idx]))
405
406 def save_sol(self, filename=None):
407     if filename is None:
408         idx = 1
409         file_list = [os.path.basename(x) for x in glob.glob(os.getcwd()+ '/*')]
410         new_filename = self.filename
411         while new_filename+'.csv' in file_list:
412             new_filename = self.filename + '_' + f'{idx:03}'
413             idx += 1
414         pd.DataFrame(self.sol.T).to_csv(new_filename + '.csv')
415     else:
416         idx = 1
417         file_list = [os.path.basename(x) for x in glob.glob(os.getcwd()+ '/*')]
418         new_filename = filename
419         while new_filename+'.csv' in file_list:
420             new_filename = filename + '_' + f'{idx:03}'
421             idx += 1
422         pd.DataFrame(self.sol.T).to_csv(new_filename + '.csv')
423
424 def constants(self):
425     # constants
426     self.c = 299792458
427     self._hbar_ = 1.0545718e-34
428     self.h = 6.62607015e-34
429
430 def ring_parameters(self, R, height, width, ng, Nmodes, Qi, mode_offset, aux):
431     # ring parameters
432     self.R = R
433     self.height = height
434     self.width = width
435     self.ng = ng
436     self.Nmodes = Nmodes
437
438     self.Qi = Qi
439     self.L = 2*np.pi*R
440     self.A = width*height
441     self.FSR = self.c/(ng*self.L)
442     self.t_roundtrip = 1/self.FSR
443     self.mode_offset = mode_offset
444     self.aux = aux

```

## B.3 Cython

```
1 # cython: language_level=3
2 import numpy as np
3 cimport cython
4 from cython.parallel import prange
5 import pyfftw
6 # from libc.complex cimport exp as cexp
7 # from libc.complex cimport abs as cabs
8
9 cdef extern from "complex.h":
10     double complex cexp(double complex z) nogil
11     # double complex abs(double complex y) #nogil
12
13 @cython.cdivision(True)
14 @cython.boundscheck(False)
15 @cython.wraparound(False)
16 @cython.nonecheck(False)
17 cpdef double complex[:,::1] split_step_cython(unsigned int Nsim, double complex dt,
18     double complex[:,::1] dwext, double complex dwi, double complex dwtot,
19     double complex[:,::1] Dint_arr, double complex[:,::1] detuning,
20     double complex[:,::1] F_arr, unsigned int Nmodes,
21     double complex[:,::1] noise_norm, unsigned int divbysnapshot,
22     unsigned int Nsnapshots, pbar, ifft_object, fft_object,
23     double complex[:,::1] ifft_arr, double complex[:,::1] fft_arr):
24
25     cdef unsigned int Dlen = dwext.shape[0]
26     cdef double complex[:,::1] Dispersion = np.zeros((Dlen), np.complex128)
27     cdef unsigned int i
28     cdef unsigned int j
29     cdef unsigned int sol_track = 0
30     sol = np.zeros((Nsnapshots, Dlen), np.complex128)
31
32     for i in range(Nsim):
33         for j in prange(Dlen, nogil=True, num_threads=8):
34             Dispersion[j] = cexp(-(dt/2)*((dwext[j]+dwi)/dwtot+1j*(Dint_arr[j] \
35                 + detuning[i])*2/dwtot))
36             ifft_arr[j] *= Dispersion[j]
37             ifft_object()
38             for j in prange(Dlen, nogil=True, num_threads=8):
39                 fft_arr[j] = cexp(dt*(1j*abs(fft_arr[j])**2 \
40                     + (F_arr[j]/fft_arr[j]))) * fft_arr[j]
41             fft_object()
42             for j in prange(Dlen, nogil=True, num_threads=8):
43                 ifft_arr[j] *= Dispersion[j]
44                 ifft_arr[j] += noise_norm[j]
45             if (not((i+1)%divbysnapshot)) and sol_track < Nsnapshots:
46                 sol[sol_track, :] = ifft_arr
47                 sol_track += 1
48                 pbar.update(1)
49     return sol
```